LBL--33040

DE93 004700

# Structural Studies of Molecular and Metallic Overlayers Using Angle-Resolved Photoemission Extended Fine Structure

Zhengqing Huang
Ph.D. Thesis

Department of Chemistry
University of California

and

Chemical Sciences Division
Lawrence Berkeley Laboratory
University of California
Berkeley, California 94720

October 1992

This work was supported by the Director, Office of Energy Research, Office of Basic Energy Sciences, Chemical Sciences Division of the U.S. Department of Energy under Contract No. DE-AC03-76SF00098.

Structural Studies of Molecular and Metallic Overlayers Using
Angle-Resolved Photoemission Extended Fine Structure

by

Zhengqing Huang

Abstract

This dissertation reports the extension of angle-resolved photoemission extended fine structure (ARPEFS) to the structural studies of molecular and metallic overlayers on metal surfaces through the analysis of the p2mg(2×1)CO/Ni(110) and the p(2×2)K/Ni(111) adsorption systems.

For the dense p2mg(2×1)CO/Ni(110) surface layer, photoemission intensities from the carbon 1s core level were measured in three directions as a function of photoelectron kinetic energy in the range 60-400 eV. Using multiple-scattering spherical-wave (MSSW) modeling, it was found that the CO molecules are adsorbed on the short-bridge sites, with adjacent CO molecules along the $[1\bar{1}0]$ direction displaced alternatively in opposite directions towards the [001] and the $[00\bar{1}]$ azimuths to form a zigzag chain geometry. The tilt angle is 16±2° from the surface normal for the direction linking the carbon atom and the center of the nickel bridge. The carbon-nickel interatomic distance was determined to be 1.94±0.02Å. The first- to second-layer spacing of nickel is 1.27±0.04Å, up from 1.10Å for the clean Ni(110) surface, but close to the 1.25Å Ni interlayer spacing in the bulk. Using the findings of earlier studies of this system, the C-O bond length

and tilt angle were varied within small ranges (1.10-1.20Å and 15-23°, respectively) in our MSSW simulations. At 1.16Å and 19° the best agreement between the experimental data and the theoretical simulations was achieved. The above results yields an O-O distance of 2.95Å for the two nearest CO molecules, close to twice the van der Waals' radius (~1.5Å) for oxygen. Two different sets of partial-wave phase-shift were used in the MSSW calculations, and the structural results from both are in very good agreement.

For the p(2×2)K/Ni(111) overlayer, ARPEFS $\chi(k)$ curves from the potassium 1s core level measured along [111] and [771] at 130K showed that the potassium atoms are preferentially adsorbed on the atop sites, in agreement with a previous low energy electron diffraction (LEED) study of the same system. The K-Ni bond length is 3.02±0.01Å, yielding an effective hard-sphere radius of 1.77Å for potassium. The first- to second-layer spacing of nickel is 1.90±0.04Å, a 6.5% contraction from the bulk spacing of 2.03Å. Furthermore, the first nickel layer shows neither lateral reconstruction (0.00±0.09Å) nor vertical corrugation (0.00±0.03Å). A comparison of the structural parameters with those determined from the LEED study is presented. The limitations of Fourier analysis for site determination and the importance of comparing ARPEFS experimental data with theoretical simulations in both k-space and R-space are also discussed.

# Contents

List of figures ..... v

List of tables ..... vii

Acknowledgments ..... viii

**Chapter 1 Introduction ..... 1**

References ..... 7

Figure caption ..... 9

Figure ..... 10

**Chapter 2 Structural Determination of p2mg(2×1)CO/Ni(110) Using ARPEFS ..... 11**

Abstract ..... 11

2.1 Introduction ..... 13

2.2 Experiment ..... 17

2.3 Data reduction ..... 20

2.4 Structural determination ..... 25

2.4.1 Fourier analysis ..... 25

2.4.2 MSSW analysis ..... 27

2.5 Error analysis ..... 32

2.6 Discussion and conclusions ..... 37

References ..... 41

Tables ..... 44

Figure captions ..... 47

Figures ..... 50

**Chapter 3 ARPEFS Study of the Structure of p(2×2)K/Ni(111) ..... 71**

Abstract ..... 71

3.1 Introduction ..... 72

3.2 Experiment ..... 75

3.3 Data reduction ..... 79

3.4 Results and analysis ..... 81

3.4.1 The [111] data ..... 81

3.4.1.1 Fourier analysis ..... 83

3.4.1.2 MSSW analysis ..... 85

3.4.2 The [771] data ..... 89

3.4.3 Structural refinement and error analysis ..... 91

3.5 Discussion and conclusions ..... 93

References ..... 96

Tables ..... 99

Figure captions ..... 102

Figures ..... 104

# List of Figures

1.1 Schematic of photoelectron diffraction....10

2.1 Model of p2mg(2×1)CO/Ni(110) and experimental geometry....50

2.2 p2mg(2×1)CO/Ni(110) experimental data....51

2.3 Fourier transform of p2mg(2×1)CO/Ni(110) $\chi$(k) curves....52

2.4 Adsorption sites considered for p2mg(2×1)CO/Ni(110)....53

2.5 Reduced structural models for p2mg(2×1)CO/Ni(110)....54

2.6 Reduction of theoretical $\chi$(k) curves....55

2.7(a) MSSW best fit, bridge-I site....56

2.7(b) MSSW best fit, hollow site....57

2.7(c) MSSW best fit, bridge-II site....58

2.7(d) MSSW best fit, top-I site....59

2.7(e) MSSW best fit, top-II site....60

2.7(f) MSSW best fit, bridge-I site (Rehr's PWPS)....61

2.8(a) FT of MSSW best fit, bridge-I site....62

2.8(b) FT of MSSW best fit, hollow site....63

2.8(c) FT of MSSW best fit, bridge-II site....64

2.8(d) FT of MSSW best fit, top-I site....65

2.8(e) FT of MSSW best fit, top-II site....66

2.8(f) FT of MSSW best fit, bridge-I site (Rehr's PWPS).....67

2.9 R-factor vs. structural parameters.....68

2.10 Best-fit structure of p2mg(2×1)CO/Ni(110).....69

2.11 Comparison between ARPEFS and LEED results.....70

3.1 Model of p(2×2)K/Ni(111) and experimental geometry.....104

3.2 p(2×2)K/Ni(111) experimental data.....105

3.3 Fourier transform of [111] $\chi$(k) curve.....106

3.4 [111] MSSW best-fit for various sites.....107

3.5 FT of MSSW best-fit [111] $\chi$(k) curves.....108

3.6 Comparison of [771] $\chi$(k) curves.....109

3.7 Surface reconstruction in p(2×2)K/Ni(111).....110

3.8 R-factor vs. structural parameters.....111

# List of Tables

2.1 Best-fit results for different structural models of p2mg(2×1)CO/Ni(110) ..... 44

2.2 Structural parameters of p2mg(2×1)CO/Ni(110) (Pendry's PWPS) ..... 45

2.3 Structural parameters of p2mg(2×1)CO/Ni(110) (Rehr's PWPS) ..... 46

3.1 Estimated scattering angles ..... 99

3.2 Best-fit results for various proposed adsorption sites of p(2×2)CO/Ni(111) ..... 100

3.3 Comparison between ARPEFS and LEED results ..... 101

# Acknowledgments

I would like to thank my thesis advisor Dave Shirley for his interest in this work and for his support and guidance over the years. I had the privilege of working with Tong Leung and Xunsheng Zhang when I began learning surface science. Lou Terminello introduced me to ARPEFS through many days and nights of work at SSRL and LBL. Thanks also go to all my other collaborators, especially Zahid Hussain, Liqiong Wang, and Alexis Schach von Wittenau, and to the many others who have helped me in one way or another.

I am honored to have met many interesting people and made many friends over the years. Phil Heimann, Hong Lin, Jane Medhurst, Baohua Niu, Tobias Reich, Lou Terminello, Liqiong and Laisheng Wang, Peng Wang, Linfeng Xie, and Jingsong Zhang have been constant sources of information; I enjoyed the many conversations and discussions with them. Special thanks go to Roger van Zee for the many shared meals. The entire Shirley group has been most friendly: I thank you all.

Most importantly, I thank my family for their love and support through all these years.

This work was supported by the Director, Office of Energy Research, Office of Basic Energy Sciences, Chemical Sciences Division of the U.S. Department of Energy under Contract No. DE-AC03-76SF00098.

# Chapter 1

# Introduction

Determining the bonding geometry of the interface between a solid surface and a vacuum constitutes an important area of surface-science research. Not only is a quantitative knowledge of the atomic arrangements on surfaces important from a structural point of view, it also provides the basis for an understanding of other surface phenomena, such as surface electronic structures, the nature of surface chemical bonding, and surface chemical reactions.

Amongst the many methods employed in the structural studies of clean and adsorbed single-crystal surfaces, the electron-diffraction based techniques of low energy electron diffraction (LEED),[1] surface extended x-ray absorption fine structure (SEXAFS),[2] and angle-resolved photoemission extended fine structure (ARPEFS)[3-6] are perhaps the most extensively used and also the most quantitative. The ARPEFS technique in particular has been shown to be capable of determining the bonding geometry of atoms (mainly sulfur and chlorine) adsorbed on metal and semiconductor surfaces with a precision of 0.01Å in the most favorable cases.[4,5] This dissertation describes, through the analysis of the p2mg(2×1)CO/Ni(110) and the p(2×2)K/Ni(111) adsorption systems, the application of ARPEFS to the structural determinations of two new types of surface layers, *i.e.*, molecular and metallic overlayers on metal surfaces. Necessary refinements of the ARPEFS method that will facilitate the studies of these systems

will be discussed. The structural analysis of these two surfaces, especially of p2mg(2×1)CO/Ni(110), will demonstrate the capability of ARPEFS to determine the structure of complicated systems.

Angle-resolved photoemission extended fine structure is the modulation of the photoemission partial cross-section of a core level of the adsorbed (or substrate) atoms as a function of the energy with which the core-level electrons are emitted. It is a special form of photoelectron diffraction, first predicted by Liebsch[7,8] and later confirmed experimentally by several groups.[9-11] Figure 1.1 illustrates the basic principle of photoelectron diffraction. A core-level electron is ejected from an adsorbed atom by a monochromatic beam of photons of energy $h\upsilon$. The kinetic energy, E, of the photoelectron equals the photon energy less the core-level binding energy. The photoelectron wavevector k inside the solid can be calculated using the de Broglie relation:

$$k(\text{Å}^{-1}) = 0.5123[E + V_0(eV)]^{1/2}, \qquad (1)$$

where $V_0$ is the inner potential of the solid. The photoelectron wave travels in all directions, part of it going directly towards the electron detector and part of it being scattered by nearby atoms before reaching the detector. The phase difference, $kr_j(1-\cos\theta_j)$, between the direct and the scattered wave cause these two waves to interfere. An interference pattern of peaks and valleys can be observed by either varying the direction in which electrons are detected while fixing the electron wavevector k (and hence the electron kinetic energy E and the photon energy $h\upsilon$), or varying the electron kinetic energy (by varying the photon energy) while keeping the angle of electron detection fixed. These

diffraction patterns reflect the local environment of the photoemitting atom and can be analyzed to yield structural information.

Variants of the angle-varying method include azimuthal photoelectron diffraction (APD),[12] polar photoelectron diffraction (PPD),[13,14] and more recently, photoelectron holography[15,16] in which a two-dimensional photoelectron interference pattern is recorded and in turn Fourier-transformed to obtain a real-space picture of the geometric environment of the photoemitting atom. This new technique is still in its early stage of development and shows promises as a tool for surface structural studies. Both the APD and the PPD techniques are often referred to as the X-ray photoelectron diffraction (XPD). They are dominated by strong peaks under the forward-scattering condition $\theta_j = 0$. For atomic-adsorption systems there are no forward-scattering atoms for the photoemitting adsorbate atom for most detection angles, thus XPD are not very well suited to the study of these systems. However, in cases such as molecular adsorption and multilayer growth, XPD is a very sensitive method for determining if there is an atom situated between the photoemitting atom and the detector at the particular detection direction. For example, the XPD of carbon 1s core level from the p2mg(2×1)CO/Ni(110) overlayer system,[13,14] whose structure will be the focus of Chapter 2, shows a strong peak when the detector is positioned at an angle of 21° from the surface normal, indicating that the CO molecule is adsorbed on the surface through the carbon end, and the C-O bond axis is 21° from the surface normal. The C-O bond length, however, cannot be obtained from XPD because the path-length difference $r_j(1-\cos\theta_j)$ is zero for forward-scattering regardless of the bond length $r_j$. The position of the carbon atoms (the adsorption sites) relative to the substrate nickel atoms are also not accessible from XPD.

Early studies of energy-dependent photoelectron diffraction[11] focused on detecting electrons in the kinetic energy range 50-200eV along the direction normal to the surface — hence the term "normal photoelectron diffraction (NPD)". Extracting structural information from NPD required implicit and complicated LEED-like "quasi-kinematic" calculations.[17] The basic physics of ARPEFS are similar to that of NPD, but ARPEFS represents significant developments over NPD in many aspects. First of all, ARPEFS uses a EXAFS-like cluster approach in which electrons are treated as scattering from individual atoms, while in NPD electrons are considered to be scattering off planes of atoms. The advantage of the cluster approach is that it is concerned with the relative positions of the photoemitting atom and its surrounding atoms, thus enabling explicit inclusion of adsorption sites and lateral displacements in structural analysis. This feature, coupled with another two improvements of ARPEFS over NPD [the detection of electrons in a wider energy window (~50-500eV) and the resulting higher resolution of Fourier transform], makes it possible to derive the adsorption sites and approximate interatomic distances from the data for many simple systems without the necessity of performing theoretical calculations. A further improvement of ARPEFS is that the experimental diffraction data are measured in more than one emission directions. Since different scattering atoms are emphasized in different directions due to the strong variation of scattering amplitude with scattering angle,[3-5] multiple ARPEFS-data sets facilitates the precise determination of more structural parameters than a single data set would allow for many systems. For some structures[6,18] it is useful, or even necessary, to have more than one data set to distinguish among various possible structures. A final improvement of ARPEFS is using the Taylor-series magnetic-quantum-

number expansion approximation to describe the scattering of spherical waves by a central potential.[19] This development permits more economical multiple-scattering spherical-wave (MSSW)[20] simulations to be used in the precise determination of surface structures from ARPEFS data, though a complicated structure such as p2mg(2×1)CO/Ni(110) still requires a large amount of computing.

We now briefly describe the procedure of structural analysis using ARPEFS data. In the single-scattering model of ARPEFS, the relative variation of photoelectron intensity $\chi(k)$ with photoelectron wavenumber k can be expressed as (see Figure 1.1)

$$\chi(k) \propto \sum_j A_j(k)\cos[kr_j(1-\cos\theta_j)+\phi_j], \qquad (2)$$

where $A_j(k)$ is a combination of various nonstructural factors and $\phi_j$ is the scattering phase shift. A structural analysis using ARPEFS data usually involves two steps. The first step is to Fourier transform the experimental $\chi(k)$. The amplitudes and path-length differences $r_j(1-\cos\theta_j)$ of the Fourier peaks are compared to those estimated for various adsorption sites using a physically reasonable range of interatomic distances. Usually only one proposed site compares favorably to the experimental Fourier transform. The second step in the analysis is using the more detailed MSSW analysis for a precise determination of bond-angles, bond lengths, interlayer spacings, and surface reconstruction for this favored site. This analysis involves varying both the structural and nonstructural parameters and calculates theoretical $\chi(k)$'s until the best agreement between theory and experiment is achieved. In cases where a Fourier transform favors no

particular sites because of the complexity of the structure or unresolved path-length differences, MSSW simulations for all possible sites are necessary in order to distinguish among these possibilities. Both of the p2mg(2×1)CO/Ni(110) and the p(2×2)K/Ni(111) adsorption systems studied in this thesis required complete MSSW analysis.

The remainder of this dissertation is organized as follows: Chapter 2 describes the ARPEFS study of the unusual p2mg(2×1)CO/Ni(110) overlayer in which there are two inequivalent tilted CO molecules in a unit cell. It also discusses how multiple $\chi(k)$ curves are used for unambiguous assignment of the absorption geometry. Two different sets of partial-wave phase-shift (PWPS) for MSSW calculations are used to assess the errors associated with these PWPS's. Chapter 3 presents the structural analysis of p(2×2)K/Ni(111) and discusses the importance of comparing experimental and theoretical data in both the k space and the R space. Experimental details and conclusions from each study are discussed separately in the respective chapters.

# REFERENCES


1. J.B. Pendry, *Low Energy Electron Diffraction* (Academic, London, 1974).
2. J. Stöhr, D. Denley, and P. Perfetti, Phys. Rev. B **18**, 4132 (1978).
3. J.J. Barton, C.C. Bahr, Z. Hussain, S.W. Robey, J.G. Tobin, L.E. Klebanoff, and D.A. Shirley, Phys. Rev. Lett. **51**, 272 (1983).
4. L.J. Terminello, X.S. Zhang, Z.Q. Huang, S.Kim, A.E. Schach von Wittenau, K.T. Leung, and D.A. Shirley, Phys. Rev. B **38**, 3879 (1988).
5. L.Q. Wang, Z. Hussain, Z.Q. Huang, A.E. Schach von Wittenau, D.W. Lindle, and D.A. Shirley, Phys. Rev. B **44**, 13711 (1991).
6. Z.Q. Huang, Z. Hussain, W.T. Huff, E.J. Moler, and D.A. Shirley, Phys. Rev. B, submitted.
7. A. Liebsch, Phys. Rev. Lett. **32**, 1203 (1974).
8. A. Liebsch, Phys. Rev. B **13**, 544 (1976).
9. S. Kono, C.S. Fadley, N.F.T. Hall, and Z. Hussain, Phys. Rev. Lett. **41**, 117 (1978).
10. D.P. Woodruff, D. Norman, B.W. Holland, N.V. Smith, H.H. Farrell, and M.M. Traum, Phys. Rev. Lett. **41**, 1130 (1978).
11. S.D. Kevan, D.H. Rosenblatt, D. Denley, B. -C. Lu, and D.A. Shirley, Phys. Rev. Lett **41**, 1505 (1978).
12. P.J. Orders, R.E. Connelly, N.F.T. Hall, and C.S. Fadley, Phys. Rev. B **24**, 6163 (1981).
13. D.A. Wesner, F.P. Coenen, and H.P. Bonzel, Phys. Rev. Lett. **60**, 1045 (1988).
14. D.A. Wesner, F.P. Coenen, and H.P. Bonzel, Phys. Rev. B **39**, 10770 (1989).
15. J.J. Barton, Phys. Rev. Lett. **61**, 1356 (1988).

16. B.P. Tonner, Ultramicroscopy, **36**, 130 (1991).

17. C.H. Li and S.Y. Tong, Phys. Rev. Lett. **42**, 901 (1979); C. H. Li, A. R. Lubinsky, and S.Y. Tong, Phys. Rev. B **17**, 3128 (1978).

18. Z.Q. Huang, L.Q. Wang, A.E. Schach von Wittenau, Z. Hussain, and D.A. Shirley (unpublished).

19. J.J. Barton and D.A. Shirley, Phys. Rev. B **32**, 1906 (1985).

20. J.J. Barton, S.W. Robey, and D.A. Shirley, Phys. Rev. B **34**, 778 (1986).

# FIGURE CAPTION

Figure 1.1 Schematic showing the interference effect in photoelectron diffraction. A photoelectron is emitted from the core-level of an adsorbate (shaded) atom. The direct wave and the scattered wave have a path-length difference of $r_j(1-\cos\theta_j)$ (dark arrows) at the angle-resolved electron detector. In ARPEFS the electron intensity is recorded as a function of the energy at each selected angle.

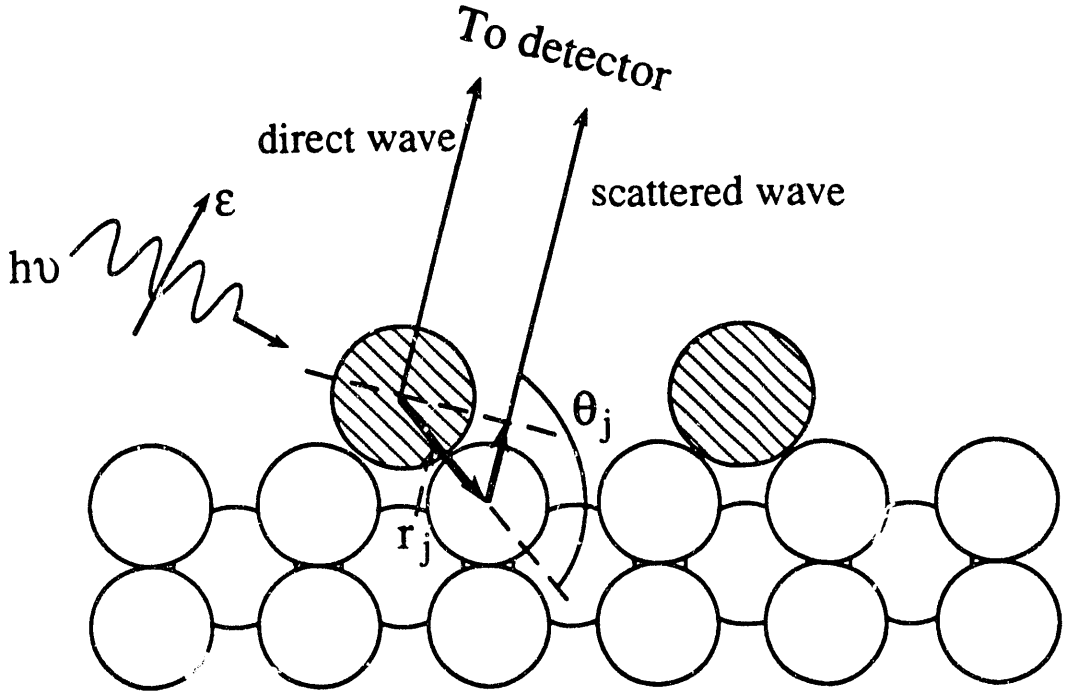


Figure 1.1

# Chapter 2

# Structural Determination of p2mg(2×1)CO/Ni(110) Using ARPEFS

## Abstract

The technique of angle-resolved photoemission extended fine structure (ARPEFS) has been used to study the chemisorption geometry of the dense p2mg(2×1)CO/Ni(110) overlayer at low temperatures. Photoemission intensities from the carbon 1s core level were measured in three directions as a function of photoelectron kinetic energy in the range 60-400 eV. Using multiple-scattering spherical-wave (MSSW) modeling, it was found that the CO molecules are adsorbed on the short-bridge sites, with adjacent CO molecules along the [1$\bar{1}$0] direction displaced alternatively in opposite directions towards the [001] and the [00$\bar{1}$] azimuths to form a zigzag chain geometry. The tilt angle is 16±2° from the surface normal for the direction linking the carbon atom and the center of the nickel bridge. The carbon-nickel interatomic distance was determined to be 1.94±0.02Å. The first- to second-layer spacing of nickel is 1.27±0.04Å, up from 1.10Å for the clean Ni(110) surface, but close to the 1.25Å Ni interlayer spacing in the bulk. Using the findings of earlier studies of this system, the C-O bond length and tilt angle were varied within small ranges (1.10-1.20Å and 15-23°, respectively) in our MSSW simulations. At 1.16Å and 19° the best agreement between the experimental data and the theoretical simulations was achieved. The

above results yields an O-O distance of 2.95Å for the two nearest CO molecules, close to twice the van der Waals' radius (~1.5Å) for oxygen.

## 2.1 INTRODUCTION

Dense atomic and molecular overlayers on metal surfaces are of great interest because these systems often exhibit unusual atomic arrangement and surface symmetry.[1-3] While at low adsorption coverages the structures and properties of surface overlayers are generally more influenced by the interaction between the adsorbed molecules and the metal substrate, the adsorbate-adsorbate interaction becomes more important as the coverage increases. The close packing of these adsorbed species at high coverages can alter the adsorption site, orientation, long range order, and other structural and electronic properties of the surface and near-surface regions.

Perhaps the most studied of these dense molecular overlayers is the saturation monolayer of carbon monoxide adsorbed on the Ni(110) surface at temperatures below 200K. The structure of CO/Ni($\bar{1}$10) at various coverages has been investigated by low-energy electron diffraction (LEED),[4-7] high resolution electron energy loss spectroscopy (HREELS),[8,9] electron stimulated desorption ion angular distribution (ESDIAD),[3,10] angle-resolved photoelectron spectroscopy (ARPES),[11,12] polar X-ray photoelectron diffraction (XPD),[13,14] inverse photoemission,[15,16] and other techniques. It was observed that the CO molecules adsorb perpendicularly to the surface on a mix of top and short-bridge sites through the carbon atoms at low coverages. At coverages of 0.4 to 0.75 monolayers some of the CO molecules begin to tilt from the perpendicular orientation. As the coverage increases to near one monolayer (one CO molecule per surface Ni atom), all the CO molecules are tilted away from the surface normal, half of them towards [001] and the other half towards [00$\bar{1}$]. It was also found

that the tilt angle is the same for both directions, its magnitude varying from 17° as determined by ARPES[11] and ESDIAD[3] measurements to 21° determined with XPD. The observation of a single C-O stretch frequency also suggested that all the CO molecules occupy the same type of adsorption site.

Lambert[5] had earlier proposed a model for this structure based on its unique p(2×1)-like LEED pattern, in which the fractional order beams (±(2n+1)/2, 0) in the [1$\bar{1}$0] azimuth are absent at all energies. In this model the CO molecules are adsorbed in zigzag chains along the [1$\bar{1}$0] rows of Ni atoms, with adjacent molecules displaced alternately along the [001] and [00$\bar{1}$] directions and away from the high-symmetry sites. He also assigned the surface symmetry group as belonging to p1g1. Nishijima *et al.*[8] later suggested that this structure may be best interpreted as having p2mg symmetry because of the existence of a mirror plane along [001], which was further confirmed by experimental work using ARPES, ESDIAD, XPD and inverse photoemission.

A model of this saturation overlayer is illustrated in Figures 2.1(a) and 2.1(b), where we have tentatively assigned the adsorption site to be displaced short-bridge site. If the CO molecules were to occupy high symmetry positions, such as undisplaced top or bridge sites, in a perpendicular fashion, the distance between these molecules would be 3.52Å in the [001] direction, but would only be 2.49Å in the [1$\bar{1}$0] direction — much smaller than the minimum intermolecular distance of 3.0-3.05Å observed for CO molecules.[1,2,17] As a result, the adjacent molecules along [1$\bar{1}$0] are tilted in opposite directions towards the [001] azimuth to avoid the strong intermolecular repulsion. Even if the CO molecules are tilted and displaced in a way such that the larger oxygen ends of the molecules are equally spaced, the O-O distances would still be only 3.05Å. This structure is in

fact the most dense CO overlayer observed so far. The large dispersions of its vibrational modes[9] and electronic energy levels[11,12] are clearly results of this densely-packed and strongly-interacting structure.

Although many experiments have been done and much has been learned about the structure and the properties of this surface layer, and the above model has been widely accepted, there are still many unknowns and much controversy concerning how the CO layer is situated above the nickel surface. Do the CO molecular zigzag chains lie along the ridges, or in the troughs of the (110) surface? If they are along the ridges, do the molecules sit on the atop sites or the short bridge sites? Would it be long bridge site or hollow site in the case where the zigzag chains lie in the troughs? How much do the CO molecules need to be displaced from these high-symmetry sites in order to minimize intermolecular repulsion? While most of the previous work on this surface did not, and was not able to, address the question of the CO adsorption site, the few studies that did differed on their conclusions about the structure. An earlier EELS study[8] favored displaced long-bridge site while a later EELS work[9] argued for a top-site adsorption by means of the more detailed symmetry analysis of the vibrational modes. A LEED I-V study,[7] on the other hand, preferred the short-bridge site adsorption and determined the carbon-metal tilt angle to be 27±5°. While the EELS method is less direct, it was pointed out that the LEED work might have ruled out the top site at too early a stage based on I-V curves for a non-tilt geometry and might have missed a possible good fit at some tilt angle. It is obvious that a more detailed investigation of this structure, possibly by another technique, was called for in order to help resolve this controversy. Another point of interest that had not been adequately addressed is how the adsorption of

carbon monoxide modifies the structure of the underlying Ni substrate, particularly how it affects the Ni first- to second-layer spacing, which on a clean Ni (110) surface was found[18] to be 1.10Å, a 10% contraction compared to 1.245Å for the bulk. The adsorption site, the carbon-nickel tilt angle and interatomic distance, and the adsorption-induced surface relaxation will be the main subjects of this chapter based on our investigation using angle-resolved photoemission extended fine structure (ARPEFS)[19].

There are several reasons why we used ARPEFS to study the structure of CO/Ni(110). First of all, ARPEFS is a local structural probe. It has been shown to be capable of determining surface and near-surface structures of atomic overlayers accurately, sometimes to four or five atomic layers beneath the surface.[20] Its sensitivity to both the perpendicular and the horizontal displacements of the surface layer[21,22] could be very useful for this work since the determination of the C-Ni tilt is equivalent to the determination of the lateral and perpendicular displacements of the carbon atom from a high-symmetry site on the Ni surface. Furthermore, although the predecessor of ARPEFS, the normal photoelectron diffraction (NPD) technique, has been used to study the adsorption of CO molecules on Ni(001) and Ni (111) surfaces,[23] the structural information that could be obtained from NPD data was limited because only electrons emitted in one direction (the direction normal to the surface) in a small kinetic-energy range (~ 50-200eV) were detected in a typical NPD measurement. NPD is most sensitive to the adsorbate-substrate interlayer spacing and less sensitive to the adsorption site.[25] It also required a somewhat implicit and complicated LEED-like theoretical analysis. ARPEFS represents a significant improvement over NPD, both in the use of wider energy windows and multiple emission directions in the

experimental measurements of diffraction data, and in the more direct and simpler theoretical description of the electron scattering process and the interpretation of the experimental data. These developments greatly increase the sensitivity of ARPEFS to other structural parameters, thus allowing adsorption site(s) to be determined unambiguously and the structure to be revealed in greater details (such as corrugation, reconstruction). ARPEFS has been very successful in determining the geometries of atomic adsorbates (mainly P, S, and Cl) on metal and semiconductor surfaces, but has not been previously applied to the structural studies of molecular overlayers on surfaces. This work would therefore be an important test of the feasibility of applying ARPEFS and its theoretical treatments to the study of molecular adsorption systems.

## 2.2 EXPERIMENT

The Ni(110) crystal (7×7×1mm) used in this work was cut from a high-purity single crystal rod, then mechanically polished and chemically etched. Its orientation was determined to be within ±1° of the (110) plane using Laue backscattering. The crystal was then spotwelded between two tungsten wires onto a high precision manipulator equipped with liquid nitrogen cooling and inserted into an ultrahigh-vacuum chamber. The manipulator allowed linear motions along three perpendicular axes as well as rotations about the crystal surface normal and the vertical axis. Prior to the carbon 1s ARPEFS measurement the Ni surface was cleaned by repeated cycles of $Ar^+$ sputtering at energies of 500 to 1000eV, followed by annealing at 700 to 900°C with electron-beam heating. The crystal's cleanliness and surface order were monitored by Auger

electron spectroscopy (AES) and LEED. After most of the bulk impurities had been segregated to the surface and removed, only one or two additional cycles of sputtering and annealing at lower temperatures (550-650°C) were needed for subsequent cleaning of the surface.

The CO overlayer was prepared by first cooling the cleaned crystal to around 120K and then backfilling the sample chamber with $1\times10^{-7}$ Torr of CO through a variable leak valve filled with high purity (99.995%) CO. The storage area of the leak valve was repeatedly flushed before CO was allowed into the chamber. It was consistently observed that a p2mg(2×1) LEED pattern started to develop after an exposure of 8-10 Langmuir (L). At around 12L the pattern was very sharp, with little background. Further exposure (up to 100L) did not change either the LEED pattern or the C(273eV)/Ni(848eV) Auger peak ratio. Therefore, it was assumed that after 12L the surface reaches its saturation coverage and no further adsorption of CO occurs.

An ARPEFS experiment involves detecting the angle-resolved photoelectron intensity of a certain atomic core level as a function of electron kinetic energy in one or more directions. Therefore it requires the use of variable-energy vacuum ultra-violet or X-ray sources. For this work the experiment was performed at the National Synchrotron Light Source on beamline U3C using a 5m extended-grasshopper-type grating monochromator. Three different experimental geometries were chosen for the ARPEFS measurements. For all the three geometries the electron emission and photon polarization directions were oriented along the [001] azimuth. In the case of simple atomic adsorption system it has been shown[24] that by aligning the electron emission direction along the bond axis linking the emitter and a backscatterer (provided a good guess can be

made of the structure to be determined), the ARPEFS curves would exhibit enhanced sensitivity to these specific backscattering substrate atoms. Because the CO molecules are tilted towards the [001] azimuth, our choice of this azimuth for the photon polarization and the detection of photoelectrons was aimed to allow the structure to be determined more precisely. On the other hand, even though the two CO molecules that are tilted away in two opposite directions are chemically and structurally the same, they are not equivalent in a typical ARPEFS experiment. The measured ARPEFS spectrum is the sum of the contributions from both carbon atoms, each with its own high-sensitivity direction. Adding the two contributions effectively lowers the angular sensitivity. This complexity, in addition to the fact that neither the adsorption site for the CO molecules nor the carbon-to-nickel tilt angle can be easily guessed, left no clear choices of specific directions to make the best use of the angular sensitivity. Nevertheless, it is still very important to take ARPEFS curves at different directions to ensure that consistent structural parameters can be determined from independent measurements and to allow more meaningful estimates of errors.

The three experimental geometries, illustrated in Figure 2.1(c), are as follows: (a) emission at 7° off-normal towards [00$\bar{1}$] with the photon polarization vector oriented 35° from surface normal towards [001]; (b) emission and polarization both set at 27° off-normal towards [001]; and (c) emission and polarization both at 40° from surface normal towards [001]. We will denote these three arrangements as near-normal, off-normal-1, and off-normal-2, respectively. The emission direction of geometry (a) can also be described as -7° from surface normal towards the [001] azimuth. This distinction is only important for inputs into theoretical modeling. Unless specifically pointed out, from here on we will

simply use [001] to denote both the [00$\bar{1}$] and the [001] azimuths, without explicit reference to the direction of the vector.

For each of the three geometries described above the carbon 1s photoemission spectra were measured in increments of 0.08 $Å^{-1}$ (corresponding to 3-6eV depending on the kinetic energy) over the kinetic energy range of 60-400eV (photon energy in the range of 350-690eV). Each photoemission spectrum had an energy window of 20-25eV, with the photopeak appearing approximately at the center. Data were collected using an angle-resolved and rotatable electrostatic hemispherical analyzer[25] operating at 160 eV pass energy. The angular resolution of the input lens is 3°. The combined resolution of the photon source and the electron energy analyzer increases from 1.0 to 2.5eV with increasing energy. Photoemission spectra were taken right after the cleaned and cooled Ni sample was exposed to 20L of CO gas. To avoid desorption or dissociation of the CO molecules by electron bombardment, neither LEED nor Auger observations were made until after each ARPEFS curve was completed, which typically entailed 6-8 hours of measurement. A new CO overlayer was prepared for the measurement of each ARPEFS curve. Throughout the experiment the base pressure of the chamber was between $8\times10^{-11}$ and $2\times10^{-10}$ Torr. LEED pattern after each run showed the p2mg(2×1) symmetry with sharp spots, and no impurities were detectable with AES.

## 2.3 DATA REDUCTION

To generate photoemission partial cross sections as a function of photoelectron kinetic energy it is necessary to extract the photopeak areas of all

spectra for a given experimental geometry and normalize these areas to one another in order to compensate for the variations in the energy-dependent photon flux and the transmission function of the electron analyzer. Each photoelectron spectrum has three components, the photopeak, an energy loss function, and an inelastic background[19]. In recent ARPEFS studies[22,26] a Voigt (Gaussian convoluted with Lorentzian) function has been used to model the core-level photoelectron peak, accounting for both the lifetime broadening and the limited resolution of the photon source and the electron analyzer. The carbon 1s peaks in this study, however, showed pronounced asymmetry in its shape and cannot be accurately modeled with a Voigt function. This asymmetry in photoemission and photoabsorption line shapes has been discussed by Doniach and Šunjić[27] who attributed it to the Kondo-like many-body electron interaction of the final-state core hole with the conduction electron. Employing a Gaussian-convoluted Doniach-Šunjić function instead of a Voigt function to describe the carbon 1s photopeak indeed improved the modeling greatly. The other functions that were used to least-squares fit each spectrum were a Gaussian-convoluted step function to model the energy loss function and an experimental background template determined using a procedure described elsewhere.[20] Each photoemission spectrum also had a satellite peak appearing at approximately 5.5 eV on the lower kinetic energy (higher binding energy) side of the main line. It could be interpreted as coming from the photoemission final state involving an "unscreened" core hole, while the main line is the result of a "screened" final state.[28] In principle the energy-dependent intensity of this satellite peak could be used to construct ARPEFS curves, which should look the same as the ARPEFS curves constructed from the main peak. However, the statistical error associated

with the area of this satellite peak is quite large in our measurement due to the weak intensity of the peak. We therefore used a Gaussian function to model this satellite, mainly to improve the overall fit of the whole spectrum.

Initially all parameters were allowed to vary during the fit. The values of the some of the parameters, such as the widths and asymmetry of the Doniach-Šunjić function, were then plotted against the electron kinetic energy and modeled as smooth functions using low-order polynomials. Values of these functions were in turn used as fixed values in the next round of fitting. After a few repetitions the Lorentzian width was fixed at 0.3 eV, the asymmetry parameter at 0.15 and the Gaussian width described by a smooth monotonic function with its values varying between 1.0 and 2.5 eV over the kinetic energy range of 60-400eV.

The background template served as an excellent normalization scheme[19] and was also used to subtract carbon KLL Auger peaks from the photoelectron spectra. The energy-dependent photoemission intensity I(E) was generated by plotting the Doniach-Šunjić peak area, divided by the coefficient of the background template, as a function of the mean energy of the peak. I(E) can be expressed as

$$I(E) = I_0(E)[1+\chi(E)], \qquad (1)$$

where $I_0(E)$ is a slowly varying atomic-like partial photoemission cross section for carbon 1s and $\chi(E)$ is the rapid oscillations of this cross section due to the scattering of electrons by nearby atoms. $\chi(E)$ is the ARPEFS and can be obtained from I(E) by the removal of $I_0(E)$,

$$\chi(E) = [I(E) / I_0(E)] - 1. \quad (2)$$

$I_0(E)$ is in principle the carbon 1s atomic cross section of carbon monoxide modified by the change of chemical environment upon adsorption to the Ni surface. It can in principle be calculated theoretically. In practice it can also include other low-frequency variations resulting from our data collection and reduction procedures. Therefore a low-order polynomial was used to least-squares fit I(E) and then used as an approximation to $I_0(E)$. One way to check the validity of this procedure was to multiply I(E) by some slowly varying function and then extract the $I_0(E)$ of this new I(E) curve as described above. The $\chi(E)$'s obtained in this manner were quite reproducible, which indicates that as long as the contributions to $I_0(E)$ are manifested as multiplication of low-frequency functions, they will have little effect on the ARPEFS curve $\chi(E)$. In other words, while the I(E) curve may include low-frequency contributions from other than scattering processes, the $\chi(E)$ curve extracted in this manner has little dependence on these contributions. This is why $\chi(E)$ instead of I(E) is used in comparing the experimental and theoretical curves in the R-factor analysis to be discussed later.

One of the consequences of the above procedure is that any ARPEFS structures that come from scattering at path-length differences (PLD) of less than around 2 Å will be eliminated or distorted. Therefore, structural parameters that would need to be calculated from these path-length differences cannot be determined accurately. Since the oxygen atoms in the CO molecules are situated above the carbon atoms, the path-length differences between the direct carbon 1s photoelectron wave and the oxygen-scattered wave measured at the detector fall

within the range of 0-2Å for all the three experimental geometries described in Section 2.2. Therefore, the C-O bond length and tilt angle cannot be independently determined from our study. However, the tilt angle has previously been determined[3,10,11,13] to be within 3-4° from 19°, as was mentioned in Section 2.1. And since the C-O bond order is not significantly reduced upon adsorption, judging from the C-O stretch frequency of 1984 $cm^{-1}$ as compared to 2143$cm^{-1}$ for gas phase CO molecules, its bond length should stay within a few hundredths of an Å of the 1.13Å for gaseous carbon monoxide.[29] These uncertainties in the bond angle and bond length are about the same magnitudes as would have been possibly determined with ARPEFS. Therefore in later analysis these two parameters will be treated as having almost known values, each with a small adjustable range.

Having extracted the ARPEFS curves $\chi(E)$ using the procedure described above, it is necessary to convert $\chi(E)$ to $\chi(k)$ for Fourier analysis, where k is the magnitude of the photoelectron wavevector inside the Ni crystal and can be calculated using the de Broglie relation:

$$k(\text{Å}^{-1}) = 0.5123[E + V_0(eV)]^{1/2}, \qquad (3)$$

where $V_0$ is the inner potential of the solid. The exact value of $V_0$ is not known but is around 10eV for nickel. It is treated as an adjustable parameter in our R-factor analysis. For the purpose of qualitative Fourier analysis we simply used 10eV to do the conversion. The AEPEFS $\chi(k)$ curves obtained in this manner for the three experimental geometries are presented in Figure 2.2.

## 2.4 STRUCTURAL DETERMINATION

Recent ARPEFS studies[20,22,26] have employed a two-step approach to the surface structural determination using the measured $\chi(k)$ curves. Adsorption sites and approximate interatomic distances could in most cases be determined from simple Fourier analysis, while quantitative surface geometries require theoretical simulations. To understand how structural information can be extracted from the ARPEFS $\chi(k)$ curves it is useful to examine the ARPEFS equation, which in the limit of single-scattering follows the expression

$$\chi(k) = \sum_j A_j(k)\cos[kr_j(1-\cos\theta_j)+\phi_j], \qquad (4)$$

where $A_j(k)$ includes the elastic scattering amplitude, thermal vibrations, inelastic scattering, and other non-structural factors; $\phi_j$ is the scattering phase shift; $r_j$ is the distance between the photoemitting carbon atom and the jth scattering atom; and $\theta_j$ is the scattering angle.

### 2.4.1 Fourier analysis

The sinusoidal form of $\chi(k)$ suggests that if a Fourier transformation is made of the data, the Fourier peaks should appear at the path-length differences $r_j(1\text{-}\cos\theta_j)$, shifted by some small amount if the scattering phase shift $\phi_j$ is energy-dependent. The shift caused by $\phi_j$ is usually less than 0.2 Å and can be ignored for qualitative analysis.

The Fourier spectra for the three geometries are shown in Figure 2.3. There are notable similarities among the three curves. All three spectra have a dominant feature at 3-4Å. However, each one of these features is actually the overlap of many peaks at closely spaced path-length differences that are associated with scattering from the first and second layers of Ni atoms. For example, if we refer to the final results of the structural determination, the first feature in the off-normal-2 geometry can be shown to come from four major single-scattering events with path-length differences at around 2.9Å, 2.9Å, 3.3Å and 4.4Å, respectively, and about a dozen minor peaks. Some of these scattering events followed by a second scattering from the oxygen atoms may also have total path-length differences within the range of the broad feature. It is easy to see that, with two inequivalent carbon photoemitters, adsorption sites that are displaced from high-symmetry positions, and the small Ni interlayer spacing (1.245Å in the bulk), many scattering events will have very closely-spaced path-length differences. The resolution of the above fast Fourier transformation can be estimated[30] to be no better than 1.7 Å. It would still be larger than the separation between the nearest path-length differences even with auto-regressive prediction.[30] It is therefore very difficult to pick a preferred site based on Figure 2.3 alone, given that most sites could have some Fourier peaks falling in this range. It appears that, although Fourier analysis has been demonstrated to be very useful in determining surface adsorption sites and thus narrowing down parameter space for further analysis in the case of simpler systems, such as atomic adsorption in high-symmetry sites with well-spaced path-length differences, it could not be used as effectively for more complex overlayers.

### 2.4.2 MSSW analysis

Another way of looking at the limitation of above Fourier analysis is that it uses only half the information in the original $\chi(k)$ curves — it uses only the frequency, but not the phase. This full information is used in the second method of extracting structural information from ARPEFS curves, by means of multiple-scattering spherical-wave (MSSW) analysis. In this method the experimental curves are compared with theoretical MSSW calculations for various trial structures. The structure that results in the best agreement between the experiment and the theory is considered the most likely structure for the system of interest.

The theoretical background of MSSW has been described in great details elsewhere.[31] A MSSW calculation takes as input a set of trial structural parameters and nonstructural parameters that include atomic partial-wave phase shifts (PWPS), isotropic Debye temperatures of surface atomic layers, photon polarization and electron detection directions, analyzer aperture, mean-free path parameters, experimental temperature, and the inner potential. The theory is most sensitive to structural parameters. Both the overall features and the more subtle details in the structure, such as corrugation and reconstruction, can be revealed with good precision.[20,22]

In the present study the nickel partial-wave phase shifts were from previous calculations.[32,26] The carbon and oxygen phase shifts were calculated with a modified program by Pendry,[33] using a potential obtained from atomic Hartree-Fock wave functions. The exchange potential was treated using the $X\alpha$ approach with the $\alpha$'s taken from the work of Schwarz.[34] The muffin-tin radii for

both atoms were varied between 0.5 and 0.8Å in the calculations and the optimum values were found to be between 0.65Å and 0.7Å. The sum of these muffin-tin radii is about 1.2 times the interatomic distance of 1.13Å for carbon monoxide. Using the phase shifts calculated at these radii gives the best fits between theoretical and experimental curves and the best consistency among results obtained from the three experimental geometries. We do not yet have a definite explanation for this "expansion". One possibility is that it is needed to account for the bonding electrons that are "shared" by both atoms in the molecule. We have also tried the *ab initio* complex partial-wave phase shifts calculated using the program by Rehr *et al.*[35,36] Structural results using these two sets of phase shifts agree very well. A full comparison will be presented in Section 2.5.

Surface thermal vibrations were described by a correlated Debye model.[31] The nickel bulk Debye temperature was set at 375K, while its surface Debye temperature was fixed at 263K, 289K, and 263K for the [001], [1$\bar{1}$0], and [110] directions, respectively. Variations of the oxygen-layer Debye temperatures have very little effect on the carbon 1s ARPEFS curves; they were set at 500K. The carbon Debye temperatures were initially taken at 550K for the three crystalline directions, but were allowed to vary in the calculations. The inelastic scattering was accounted for by including an exponential factor $e^{-r/\lambda}$, where $\lambda = ck$, and $c = 0.753$. The aperture size of the detector was fixed at 3° half angle. The inner potential for Ni was varied between 5 and 15eV in the fit. The experimental temperature (125±10K) and the crystal and analyzer alignments (±3°) were allowed to vary due to the limited accuracy in determining them experimentally.

For structural parameters we considered all the adsorption geometries in which the carbon atoms occupy any sites between two adjacent top sites or two adjacent short-bridge sites along the [001] azimuth, i.e., all the sites along lines AB and CD as illustrated in Figure 2.4. The C-Ni interatomic distance was taken at 1.9±0.2Å, and the first- to second-layer Ni distance was allowed to vary between 1.1 and 1.4 Å. The C-O bond length and tilt angle were varied in the ranges of 1.10-1.20Å and 15-23°, respectively. To preserve the p2mg symmetry of the surface the two CO molecules in the unit cell were treated as having the same bond length, same C-Ni distance, and the same tilt angles. The tilt directions were towards [001] and [00$\bar{1}$], respectively. With the further constraint that the nearest oxygen-to-oxygen distance be greater than 2.8Å, or about 0.2Å shorter than has been observed to be the minimum O-O distance, the structural parameter space could be further reduced into five smaller subspaces, shown as five different structural models in Figure 2.5. The choice of 2.8Å is to allow for the possible small change in the size of the CO molecules upon adsorption to the surface. These models also included some structures that were out of the ranges specified above, and some overlap of parameter space occurs among the five models, specifically between the hollow and the bridge-II sites. The important aspect is that they included <u>all</u> possibilities within the set constraints. It should be noted the top-II site can also be classified as a long bridge site; it is designated as a top site because the carbon atom is bonded closer to one of the two long-bridge atoms.

Each of the five models was characterized by an angular range specifying the C-Ni tilt angle. In the case of the short-bridge site this angle was between the surface normal and the vector connecting carbon and the midpoint of the two

nickel atoms to which the carbon atom is bonded. In the cases of top-site adsorption and hollow-site adsorption, which is actually adsorption on top of second-layer Ni, this angle is simply the tilt of the C-Ni bond from the surface normal.

To determine the geometric structure from the ARPEFS data the experimental $\chi(k)$ curves were compared with MSSW calculations using varying values for the structural and non-structural parameters until the best agreement was reached. This optimization is implemented by minimizing the R-factor, defined as

$$R = \frac{\sum_i [\chi_E(k_i) - \chi_T(k_i,\{P_j\})]^2}{\sum_i \chi_E^2(k_i)} , \qquad (5)$$

where $\chi_E(k)$ is the experimentally determined ARPEFS curve, $\chi_T(k)$ is the MSSW calculation, subscript i indicates the ith data point, and $\{P_j\}$ is the set of parameters to be optimized. The k ranges were 4.2-10.0Å$^{-1}$, 4.5-10.1Å$^{-1}$, and 4.5-9.75Å$^{-1}$ for the near-normal, off-normal-1, and off-normal-2 curves, respectively. Since we had three experimental curves and five possible structural models, there were fifteen possible experimental-theoretical combinations, each with its own parameter subspace. To minimize the R-factors for each of these combinations a simplex routine was used to automatically search both the structural and nonstructural parameters simultaneously until a minimum R factor was reached. Different starting guesses were tried to make sure that results from the fits were reproducible.

The experimental $\chi_E(k)$ curves used in the R factor minimization were smoothed by Fourier-filtering out high-frequency noise. Residual low frequency contributions not removed by the $I_0(E)$ extraction procedure described earlier were also filtered out. The cutoffs were 1.0Å and 10.05Å, 1.0Å and 9.35Å, and 1.0Å and 10.30Å for the near-normal, off-normal-1, and off-normal-2 curves, respectively (Figure 2.2). The theoretical $\chi(k)$ curves are expected to have large contributions from scattering events with low path-length differences (mainly the scatterings off oxygen atoms) and may not oscillate around zero, such as is the case for the off-normal-1 curve illustrated in Figure 2.6. To maintain consistency with the reduction procedure for the experimental data, theoretical $\chi(k)$ curves were calculated for path-length differences between zero and the high path-length-difference cutoffs mentioned above. Each $\chi(k)$ was then added to 1 to obtain I(k) [Eq.(1)], with the atomic-like cross section $I_0(k)$ assumed to be a slowly varying function (Section 2.3) — a constant was used here. A low-order polynomial was then used to extract $I_0'(k)$, which now includes low-frequency oscillations from scattering. A modified $\chi'(k)$ was then constructed using Eq.(2). After Fourier-filtering out the residual low-frequency part we now had the $\chi_T(k)$ used in Eq.(5).

Results of the best fits for the fifteen combinations are summarized in Table 2.1. The partial-wave phase shifts used in these fits are those of our calculations described earlier in this section. Comparisons between experimental and theoretical $\chi(k)$ curves are shown in Figures 2.7(a)-2.7(e). From Table 2.1 it is clear that the short-bridge site represents the most probable adsorption site for carbon monoxide. Not only are the agreements between the experiment and the theory best for this site, with the lowest R-factors, but the final structural and

non-structural parameters determined from the three curves taken at different directions are also the most consistent for adsorption on this site. For the other structural models, although the agreement in the main frequencies between the experimental and the theoretical $\chi(k)$ curves may look reasonable for some of the curves in Figure 2.7(a)-2.7(e), the amplitudes do not match well. Furthermore, parameters determined from the three curves do not match. Had we required each parameter to take the same value for all three curves, the R factors for all but the bridge sites would have been significantly larger. Our analysis therefore points out to the importance of taking multiple $\chi(k)$ curves at different directions, especially for complicated systems for which qualitative structural information cannot be obtained from Fourier analysis.

While the Fourier-transform method discussed in Section 2.4.1 was not used to determine the surface structure, we did Fourier-transform all the above best-fit theoretical $\chi(k)$ curves and compare them with the experimental curves. The results are plotted in Figures 2.8(a)-2.8(e). The MSSW calculations for the Bridge-I structure gave Fourier-transform curves in very good agreement with experiment, while the Fourier transform for the other trial structures showed poor agreement. This constitutes good confirmatory evidence for the adopted structure.

## 2.5 ERROR ANALYSIS

To illustrate the sensitivity of ARPEFS structural determinations we plot the R factor as functions of the C-Ni tilt angle, the C-Ni interatomic distance, and the Ni first- to second-layer distance, shown in Figure 2.9. All parameters except

the abscissas are fixed at their optimal values. It is quite obvious that the three $\chi(k)$ curves have about the same sensitivities to each structural parameter, quite unlike previous ARPEFS studies where directional sensitivities were used to highlight certain backscattering atoms. This is not unexpected since many more important scattering events contribute to the total $\chi(k)$ curve because of this system's structural complexity.

The statistical error associated with each structural parameter for a given $\chi(k)$ curve can also be estimated from Figure 2.9. Since our R factor minimization is in essence a nonlinear least-squares fit, we shall use the $\chi^2$ method[37] in the following error analysis. Using the same notations as in Eq.(5), $\chi^2$ is defined as

$$\chi^2 = \sum_i \frac{[\chi_E(k_i) - \chi_T(k_i)]^2}{\sigma_i^2}, \tag{6}$$

where $\sigma_i$ is the variance of the ith data points. [Notice that $\chi^2$ is to be treated as a symbol here to comply with convention and should not be confused with $\chi(k)$.] In the absence of good independent estimates of $\sigma_i$ we assume that[37]

$$\sigma_i^2 \approx \sigma^2 \approx s^2 = \frac{1}{N-n} \sum_i [\chi_E(k_i) - \chi_T(k_i, \{P_j\})]^2_{min}, \tag{7}$$

where N is the number of independent data points in a given $\chi_E(k)$ curve, n is the number of parameters used in the fit, and the subscript "min" indicates that optimized values of the parameters $P_j$ are used in the summation. Using the Nyquist sampling theorem[38] we estimate that $N = (\Delta k \times \Delta r) / \pi$, where $\Delta k$ is the data range and $\Delta r$ is the range of path-length difference used to filter the experimental data.

In making the assumption of Eq. (7) we do not have an independent assessment of the goodness of fit in the R-factor analysis. However, the statistical error of each structural parameter can still be estimated by

$$\sigma_{P_j}^2 = \frac{2}{\frac{\partial^2 \chi^2}{\partial P_j^2}} \quad . \tag{8}$$

In terms of R-factor Eq.(8) becomes

$$\sigma_{P_j}^2 = \frac{2}{\frac{\partial^2 R}{\partial P_j^2}} \times \frac{R_{min}}{N-n} , \tag{9}$$

where $R_{min}$ is the lowest R factor for the given curve. The partial derivative $\partial^2 R/\partial P_j^2$ is the curvature of the R versus $P_j$ plot near the vicinity of lowest R factor and is obtained by fitting a parabola to the data.

Results of the errors estimated using Eq.(9) are listed in parentheses in Table 2.2. Columns 2-4 gives the statistical errors associated with each parameter for the three data sets. Column 5 lists the weighted average and weighted uncertainty of each parameter, while column 6 lists the simple average and standard deviation of each parameter calculated from the scatter of its value among the three curves, without using the estimated errors from columns 2-4. Listed in Column 7 are the final structural parameters that we assign to this system, with the values taken from column 5 and the errors from the greater of columns 5 and 6, which in this case turn out to be the errors listed in column 6. The fact that the parameter values are more scattered among the three curves than

their *statistical* errors (column 5) would suggest is probably an indication of the existence of *systematic* errors that tend to affect different $\chi(k)$ curves differently. The errors listed in column 6 therefore reflect these errors to a certain extent.

Systematic errors could arise from both experimental and theoretical sources. Experimentally these sources may include the misalignment of the crystal, the electron detector, and the photon beams. The error could also arise from the $I_0(E)$ removal procedure described in Section 2.3. These errors are generally quite small and are further reduced if the relative alignment is allowed to vary within experimental accuracy in the R-factor analysis, and if both experimental and theoretical curves are Fourier filtered identically.

Theoretical sources of error in principle include all approximations used in modeling the scattering of electron in the solid. The major source, however, is the partial-wave phase shifts used in the MSSW calculation. Because of the angular dependence of the total scattering amplitude and scattering phase that are calculated from the partial-wave phase shifts, the resulting errors could be different for the $\chi(k)$ curves measured in different directions. By varying the muffin-tin radii until the resulting atomic phase shifts give the best agreement among the three curves (Section 2.4.2), we hoped to at least partly reduce the errors from the scatter of parameter values. However, the underlying theoretical approximation of atomic scattering potential used in various phase-shift programs could also cause the derived structural parameters to be biased either high or low for most or all of the curves, thereby giving rise to higher or lower final interatomic distances and other structural parameters. It has been estimated[40] that the derived nearest-neighbor distances could in some cases vary by as much as 0.02-0.03 Å using phase shifts calculated from various sources.

Much effort has been made to improve the phase shift calculation by adopting better approximations to the atomic charge densities and atomic potentials. The recent theoretical work of Rehr *et al.*[35,36] has been very successful in modeling EXAFS data to an accuracy of better than 0.02Å for nearest-neighbor distances. Their *ab initio* phase shift calculations require only inputs of atomic numbers, interatomic distance, and coordination numbers. To arrive at some estimate of the possible bias in our structural determination we have used their program to calculate the phase shifts, and used these phase shifts in an independent R-factor analysis for the bridge-I adsorption geometry. The results are listed in Table 2.3, along with the estimated errors using the procedure described earlier in this section. The $\chi(k)$ curves are plotted in Figure 2.7(f) and the Fourier-transform curves plotted in Figure 2.8(f).

Comparing Table 2.2 and Table 2.3 one finds excellent agreements between the structural parameters determined using the two sets of partial-wave phase shifts. A close examination reveals generally larger C-Ni tilt angles, shorter C-Ni bond lengths and larger first- to second-layer Ni distances using the phase shifts of Rehr *et al.*, with the differences averaging 0.01Å for distance and 1° for tilt angle. (The weighted averages of Ni interlayer spacing are both reported as 1.27Å due to round-offs.) The error associated with each parameter and the best R-factor are also very close for both sets of phase shifts. The optimal inner potentials are lower using Rehr's phase shifts, but the relative magnitudes among the three data sets remain little changed. Given that different theoretical approaches were used to describe the atomic potential that is used in the calculations of the two sets of phase shifts, the agreement is indeed very good.

Small systematic biases may exist in our structural results, but they should not be greater than the estimated statistical and random errors.

Although we have shown that both sets of phase shifts result in the same structure, the program by Rehr *et al.* has apparent advantages. With a more complete theoretical model that takes into account the atomic coordination and chemical environment, it eliminates the tedious and somewhat arbitrary procedure of searching for the optimal muffin-tin radii in the phase shift calculations. This is particularly important for molecules like CO because an isolated atomic potential model does not adequately address the effect of the valence bonding electrons on the atomic scattering potential. For atomic adsorption the choice of muffin-tin radii was shown to affect the structural determination to a lesser degree.[32,20-22,39]

## 2.6 DISCUSSION AND CONCLUSIONS

The optimized structure of a saturated overlayer of CO molecules on the Ni(110) surface is illustrated in Figure 2.10. The values listed in Table 2.2 are chosen as the final structural parameters, although the results listed in Tables 2.2 and 2.3 are almost identical. Our detailed analysis strongly favors the tilted short-bridge site for the adsorbed CO molecules. The C-Ni interatomic distance is 1.94±0.02Å, with the two adjacent carbon atoms along the [1$\bar{1}$0] zigzag chain displaced from their ideal bridge sites along the [001] and [00$\bar{1}$] directions, respectively. The C-Ni tilt angle projected onto the (001) plane, or the angle between the surface normal and the vector connecting the carbon atom and the midpoint of the two Ni atoms to which the carbon is bonded to, is 16±2°. The displacement of carbon from the ideal bridge site is 0.41±0.05Å. The first- to

second-layer spacing of nickel increases from 1.10Å for clean Ni(110) surface[17] to 1.27±0.04Å upon the adsorption of CO molecules, probably because the chemical bond between the carbon atom and the first layer Ni atom weakens the Ni-Ni bond. The value of 1.27Å is very close to the bulk Ni interlayer spacing of 1.25Å.

The C-O bond length and tilt angle cannot be independently determined from this study. The main reason for our inability to locate the position of the oxygen atoms is that they are situated above the carbon photoemitters. The path-length differences for the scattering of photoelectrons from the oxygen atoms are therefore small, and would show up as very low-frequency modulations in the $\chi(k)$ curves. These low-frequency modulations are either removed or distorted during the data reduction, and cannot be used for reliable structural determination. Fortunately, the CO bond length and tilt angle had been obtained or inferred with good precision by other studies. These predetermined values were used in the R-factor optimization, as discussed in Sections 2.3 and 2.4.2. They were allowed to vary along with the other parameters, but they were varied only through the limited ranges of 1.10-1.20Å and 15-23°, as noted in Section 2.4.2, thereby covering the values reported from previous studies. As expected, the R-factors were less sensitive to these two parameters, which affected mainly the amplitude of the $\chi(k)$ curves because of forward scattering through the oxygen atoms, but nonetheless optimized values were obtained. For the Bridge-I structure the optimal values from the fitting of the three experimental $\chi(k)$ curves all fell within the ranges of 1.15-1.18Å and 18.5-20.5°, with averages at 1.16Å and 19°, respectively. Error limits do not follow readily from this approach, but if we conservatively take the errors equal to the entire ranges through which the CO

bond length and tilt angle were varied in the R-factor analysis, or ±0.05Å and ±4°, respectively, then the shift of oxygen from carbon along the [001] direction can then be calculated as 0.38±0.08Å, for a total oxygen-atom displacement of 0.79±0.09Å from the ideal "vertical" short-bridge site.

We discussed in Section 2.1 that the main reason the CO molecules are shifted towards the [001] and [00$\bar{1}$] azimuths is to avoid the strong repulsive force among these molecules, especially the larger oxygen end, in the [1$\bar{1}$0] direction. Assuming all the oxygen atoms are separated by equal distance, which can be shown to be 3.05Å for this system, the displacement of the oxygen atoms from the bridge site would have to be 0.88Å. Our value of 0.79±0.09Å would produce a distance of 2.95±0.02Å between the two closest oxygen atoms for CO molecules adsorbed on the same Ni [1$\bar{1}$0] row and 3.16±0.02Å between the two closest oxygen atoms in adjacent rows. The nearest C-C distance can also be estimated to be 2.62Å. These numbers compare well to those shown in Figure 2.1(a).

Our conclusion that the CO molecules are adsorbed on the displaced bridge sites is in disagreement with the HREELS work[9] of Voigtländer *et al.* who proposed the CO molecules occupy the displaced top sites, but agrees with the LEED study of Hannaman and Passler[7] who favored the displaced short bridge sites. However, the C-Ni tilt angle of 27(5)° determined by the LEED study is 11° greater than the 16(2)° from our study. This difference is greater than the uncertainties of both experiments. It is interesting to note that from the LEED study, the nearest O-O distance is 3.21Å for CO molecules adsorbed to the same Ni [1$\bar{1}$0] row and 2.91Å for CO molecules in the adjacent rows, almost opposite our results. This difference is illustrated in Figure 2.11. The smallest lateral

separation between oxygen atoms in the [001] direction is 2×0.79Å from this work, separating oxygen atoms on the same Ni-atom row, and 2×0.75Å from the LEED study, separating oxygen atoms on adjacent rows. Both values agree well with the 2×0.74Å proposed by a recent He-diffraction study.[41]

# REFERENCES


1. P. Uvdal, P.-A. Karlssson, C. Nyberg, and S. Andersson, Surf. Sci. **202**, 167 (1988).
2. M.I. Ban, M.A. van Hove, and G.A. Somorjai, Surf. Sci. **185**, 355 (1987).
3. W. Riedl and D. Menzel, Surf. Sci. **163**, 39 (1985).
4. H.H. Madden, J. Kuppers and G. Ertl, J. Chem. Phys. **58**, 3401 (1973).
5. R.M. Lambert, Surf. Sci. **49**, 325 (1975).
6. R.J. Behm, G. Ertl, and V. Penka, Surf. Sci. **160**, 387 (1985).
7. D.J. Hannaman and M.A. Passler, Surf. Sci. **203**, 449 (1988).
8. M. Nishijima, S. Masuda, Y. Sakisaka, and M. Onchi, Surf. Sci. **107**, 31 (1981).
9. B. Voigtländer, D. Bruchmann, S. Lehwald, and H. Ibach, Surf. Sci. **225**, 151 (1990).
10. J. Lee, J. Arias, C. Hanrahan, R. Martin, H. Metiu, C. Klauber, M.D. Alvey, and J.T. Yates, Jr., Surf. Sci. **159**, L460 (1985); M. Alvey, M.J. Dresser, and J.T. Yates, Jr., Surf. Sci. **165**, 447 (1986).
11. H. Kuhlenbeck, M. Neumann, and H.-J. Freund, Surf. Sci. **173**, 194 (1986).
12. H. Kuhlenbeck, H.B. Saalfeld, U. Buskotte, M. Neumann, H.-J. Freund, and E.W. Plummer, Phys. Rev. B **39**, 3475 (1989).
13. D.A. Wesner, F.P. Coenen, and H.P. Bonzel, Phys. Rev. Lett. **60**, 1045 (1988).
14. D.A. Wesner, F.P. Coenen, and H.P. Bonzel, Phys. Rev. B **39**, 10770 (1989).
15. H.-J. Freund, J. Rogozik, V. Dose, and M. Neumann, Surf. Sci. **175**, 651(1986).
16. N. Memmel, G. Rangelov, E. Bertel, V. Dose, K. Kometer, and N. Rosch, Phys. Rev. Lett. **63**, 1884 (1989).
17. M.L. Xu and S.Y. Tong, Phys. Rev. B **31**, 6332 (1985).

18. P. Chini, Gazz. Chim. Ital. **109**, 225 (1979).

19. J.J. Barton, C.C. Bahr, S.W. Robey, Z. Hussain, E. Umbach, and D.A. Shirley, Phys. Rev. B **34**, 3807 (1986).

20. L.J. Terminello, X.S. Zhang, Z.Q. Huang, S.Kim, A.E. Schach von Wittenau, K.T. Leung, and D.A. Shirley, Phys. Rev. B **38**, 3879 (1988).

21. L.J. Terminello, K.T. Leung, Z.Hussain, T. Hayashi, X.S. Zhang, and D.A. Shirley, Phys. Rev. B **41**, 12787 (1990).

22. A.E. Schach von Wittenau, Z. Hussain, L.Q. Wang, Z.Q. Huang, and D.A. Shirley, Phys. Rev. B **45**, 13614 (1992).

23. S.D. Kevan, R.F. Davis, D.H. Rosenblatt, J.G. Tobin, M.G. Mason, D.A.Shirley, C.H. Li and S.Y. Tong, Phys. Rev. Lett. **46**, 1629 (1981).

24. J.J. Barton, C.C. Bahr, Z. Hussain, S.W. Robey, J.G. Tobin, L.E. Klebanoff and D.A. Shirley, Phys. Rev. Lett. **51**, 272 (1983).

25. S.D. Kevan, Ph.D. thesis, University of California, Berkeley, 1980.

26. L.Q. Wang, Z. Hussain, Z.Q. Huang, A.E. Schach von Wittenau, D.W. Lindle, and D.A. Shirley, Phys. Rev. B **44**, 13711 (1991).

27. S. Doniach and M. Sunjic, J. Phys. C **3**, 285 (1970).

28. O. Gunnarsson and K. Schönhammer, Phys. Rev. B **26**, 2765 (1982).

29. F.A. Cotton and G. Wilkinson, Advanced Inorganic Chemistry (Wiley-Interscience, New York, 1972), Chap. 3.

30. J.J. Barton, Ph.D. thesis, University of California, Berkeley, 1985.

31. J.J. Barton, S.W. Robey, and D.A. Shirley, Phys. Rev. B **34**, 778 (1986).

32. S.W. Robey, J.J. Barton, C.C. Bahr, G. Liu, and D.A. Shirley, Phys. Rev. B **35**, 1108 (1987).

33. J.B. Pendry, *Low Energy Electron Diffraction* (Academic, London, 1974).

34. K. Schwarz, *Phys. Rev.* B **5**, 2466 (1972).

35. J.J. Rehr, J. Mustre de Leon, S.I. Zabinsky and R.C. Albers, J. Am. Chem. Soc. **113**, 5135 (1991).

36. J. Mustre de Leon, J.J. Rehr, S.I. Zabinsky and R.C. Albers, Phys. Rev. B **44**, 4146 (1991).

37. P.R. Bevington, *Data Reduction and Error Analysis for the Physical Sciences* (Mcgraw-Hill, New York, 1969).

38. F.W. Lytle, D.E. Sayers and E.A. Stern, Physica B **158**, 701 (1988).

39. L.Q. Wang, A.E. Schach von Wittenau, Z.G. Ji, L.S. Wang, Z.Q. Huang and D.A. Shirley, Phys. Rev. B **44**, 1292 (1991).

40. Yu Zheng and D.A. Shirley, private communication.

41. G. Parschau and K.H. Rieder, Surf. Sci. Lett. **257**, L628 (1991).

Table 2.1: Summary of the results of R-factor analysis for different trial models.

| Geometry | Emission direction | C-(Ni) tilt angle (degrees) | C-Ni distance (Å) | $Ni_1$ to $Ni_2$ distance (Å) | Inner potential (eV) | R-factor |
|---|---|---|---|---|---|---|
| Bridge-I | near-normal | 15 | 1.93 | 1.26 | 12.9 | 0.08 |
| | off-normal-1 | 19 | 1.93 | 1.24 | 12.5 | 0.11 |
| | off-normal-2 | 16 | 1.96 | 1.31 | 13.6 | 0.09 |
| Hollow | near-normal | 26 | 1.76 | 1.35 | 10.8 | 0.40 |
| | off-normal-1 | 9 | 2.05 | 1.27 | 5.0 | 0.39 |
| | off-normal-2 | 6 | 1.91 | 1.18 | 15.0 | 0.56 |
| Bridge-II | near-normal | 43 | 1.91 | 1.30 | 5.0 | 0.57 |
| | off-normal-1 | 75 | 1.76 | 1.21 | 5.0 | 0.26 |
| | off-normal-2 | 47 | 1.93 | 1.12 | 7.0 | 0.20 |
| Top-I | near-normal | 15 | 2.05 | 1.19 | 7.1 | 0.31 |
| | off-normal-1 | 28 | 1.97 | 1.26 | 15.0 | 0.34 |
| | off-normal-2 | 16 | 1.83 | 1.33 | 15.0 | 0.20 |
| Top-II | near-normal | 42 | 1.94 | 1.21 | 15.0 | 0.38 |
| | off-normal-1 | 28 | 1.97 | 1.26 | 15.0 | 0.34 |
| | off-normal-2 | 29 | 2.01 | 1.32 | 9.8 | 0.29 |

Table 2.2. Summary of selected parameters determined from MSSW analysis using the complex partial-wave phase shifts calculated from our calculations (Sec. 2.4.2). The uncertainties are listed in parentheses.

| | near-normal | off-normal-1 | off-normal-2 | avg[a] (stat) | avg[b] (scat) | assigned value |
|---|---|---|---|---|---|---|
| C-Ni tilt angle (degrees) | 15(2) | 19(2) | 16(1) | 16(1) | 17(2) | 16(2) |
| C-Ni bond length (Å) | 1.93(.01) | 1.93(.02) | 1.96(.02) | 1.94(.01) | 1.94(.02) | 1.94(.02) |
| $Ni_1$-$Ni_2$ spacing (Å) | 1.26(.02) | 1.24(.03) | 1.31(.03) | 1.27(.02) | 1.27(.04) | 1.27(.04) |
| Inner potential (eV) | 12.9 | 12.5 | 13.6 | | | |
| Best R-factor | 0.08 | 0.11 | 0.09 | | | |

a) Weighted average and weighted uncertainty.

b) Simple average and standard deviation calculated from the scatter of results.

Table 2.3. Summary of selected parameters determined from MSSW analysis using the complex partial-wave phase shifts calculated from Rehr's program. The uncertainties are listed in parentheses.

| | near-normal | off-normal-1 | off-normal-2 | avg[a] (stat) | avg[b] (scat) | assigned value |
|---|---|---|---|---|---|---|
| C-Ni tilt angle (degrees) | 17(1) | 20(2) | 16(1) | 17(1) | 18(2) | 17(2) |
| C-Ni bond length (Å) | 1.93(.01) | 1.92(.02) | 1.95(.02) | 1.93(.01) | 1.93(.02) | 1.93(.02) |
| $Ni_1$-$Ni_2$ spacing (Å) | 1.25(.02) | 1.27(.03) | 1.31(.03) | 1.27(.02) | 1.28(.03) | 1.27(.03) |
| Inner potential (eV) | 11.5 | 10.2 | 12.2 | | | |
| Best R-factor | 0.08 | 0.13 | 0.11 | | | |

a) Weighted average and weighted uncertainty.

b) Simple average and standard deviation calculated from the scatter of results.

# FIGURE CAPTIONS

Figure 2.1. Schematic of the structure of p2mg(2×1)CO/Ni(110) and the experimental geometries. (a) Top view of the surface with the carbon and oxygen atoms drawn in their van der Waals sizes (Ref. 18). (b) Side view of the hard-sphere model of this overlayer. (c) The three experimental geometries for which the $\chi(k)$ curves were measured. In the near-normal geometry the photon polarization direction (not shown) is 35° from surface normal towards [001]. For the off-normal-1 and off-normal-2 geometries the photon polarization directions are the same as the directions of electron detection.

Figure 2.2. Experimental $\chi(k)$ curves. The darker curves represent filtered data. The lower cutoffs are 1Å for all three curves. The higher cutoffs are 10.05Å, 9.35Å, and 10.30Å for the near-normal, off-normal-1, and off-normal-2 curves, respectively. Also see Figure 2.3.

Figure 2.3. Fourier transformation of the three raw $\chi(k)$ curves shown in Figure 2.2. The three Fourier spectra are plotted on the same scale. The vertical bars near 10Å indicate the high-frequency cutoffs for the filtered data shown in Figure 2.2.

Figure 2.4. This figure illustrates the CO adsorption sites considered in the search for the optimal structure. They are all the sites between the

two ideal top sites, A and B, and all the sites between the two ideal short-bridge sites, C and D.

Figure 2.5. Reduced structural models based on Figure 2.4 and on the parameter ranges discussed in Section 2.4.2. Figures (a)-(c) and Figures (d)-(e) illustrate the transition from point C to point D and from point A to point B (Figure 2.4), respectively. [Notice that significant overlap occurs between (b) and (c).] The ranges of the carbon-nickel tilt angle $\alpha$ for these models are also shown.

Figure 2.6. This figure illustrates the procedure for reducing theoretical $\chi$ curves. The calculated curve $\chi(k)$ is converted to $\chi'(k)$ $[\chi'(k)=I(k)/I_0'(k)-1]$, which oscillates around zero and is used to compare with an experimental curve that also oscillates around zero.

Figure 2.7. (a)-(e) Comparison between experimental $\chi(k)$ curves and best-fit MSSW calculations for the structural models shown in Figure 2.5. The structural parameters used to generate the theoretical curves are listed in Table 2.1. (f) Best-fit $\chi(k)$ curves for the structure in Figure 2.5a using Rehr's partial-wave phase shifts (Ref. 34&35). Experimental $\chi(k)$ curves do not line up exactly for the different models because the optimized inner potentials are different (Eq. 3). The solid lines are experimental data and the dashed lines are MSSW calculations.

Figure 2.8. Fourier transform of the $\chi(k)$ curves in Figure 2.7. The solid lines are experimental data and the dashed lines are MSSW calculations.

Figure 2.9. Values of the R-factor as functions of C-Ni tilt angle, C-Ni distance, and first- to second-layer Ni spacing.

Figure 2.10. Optimized structure of p2mg(2x1)CO/Ni(110).

Figure 2.11. Comparison of the structures obtained from this work (a) and the LEED study of Hannaman and Passler (b) (Ref. 7).

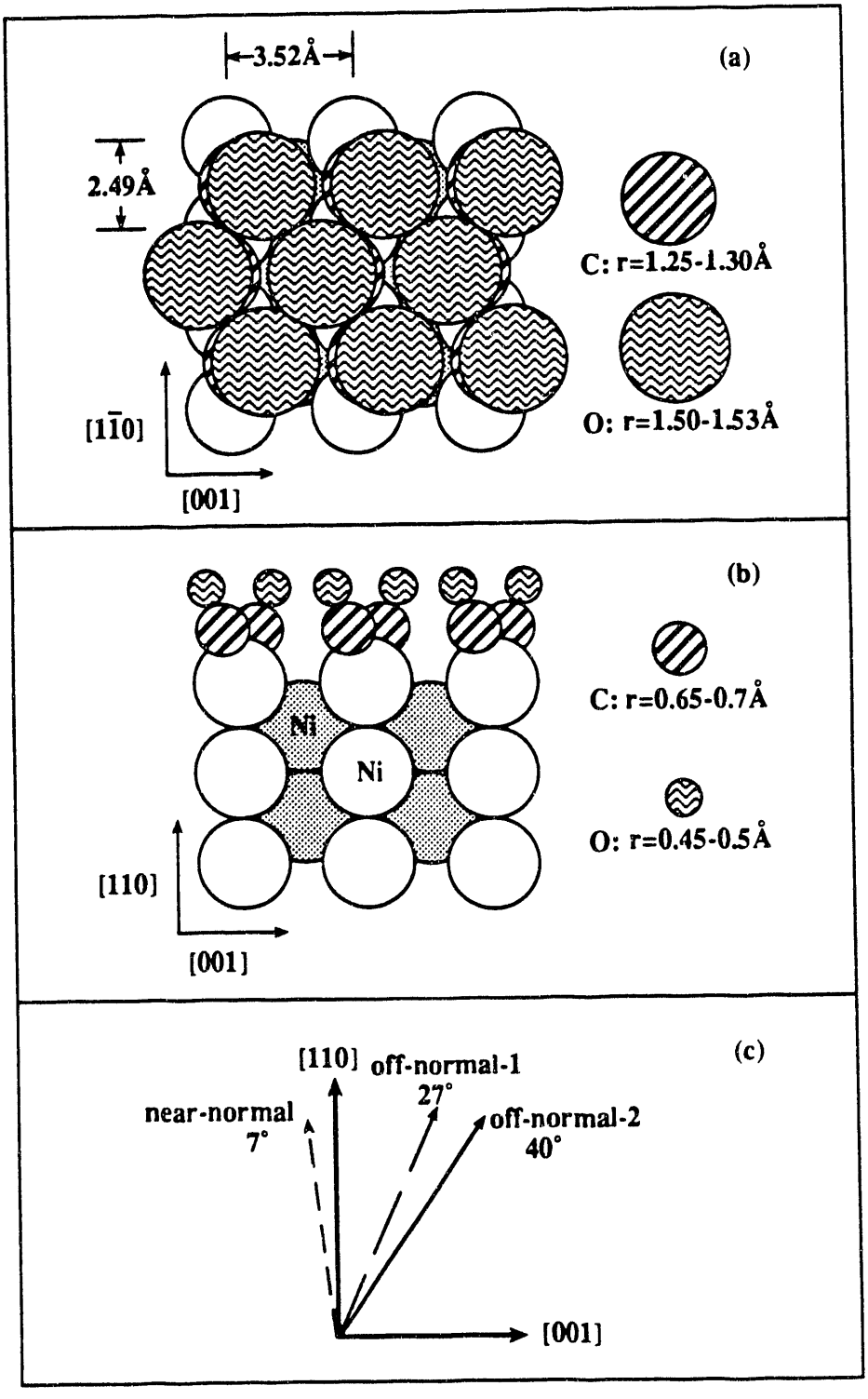
3.52Å
(a)
2.49Å
C: r=1.25-1.30Å
O: r=1.50-1.53Å
[1$\bar{1}$0]
[001]
(b)
Ni
Ni
C: r=0.65-0.7Å
O: r=0.45-0.5Å
[110]
[001]
(c)
[110]
off-normal-1
27°
near-normal
7°
off-normal-2
40°
[001]

Figure 2.1

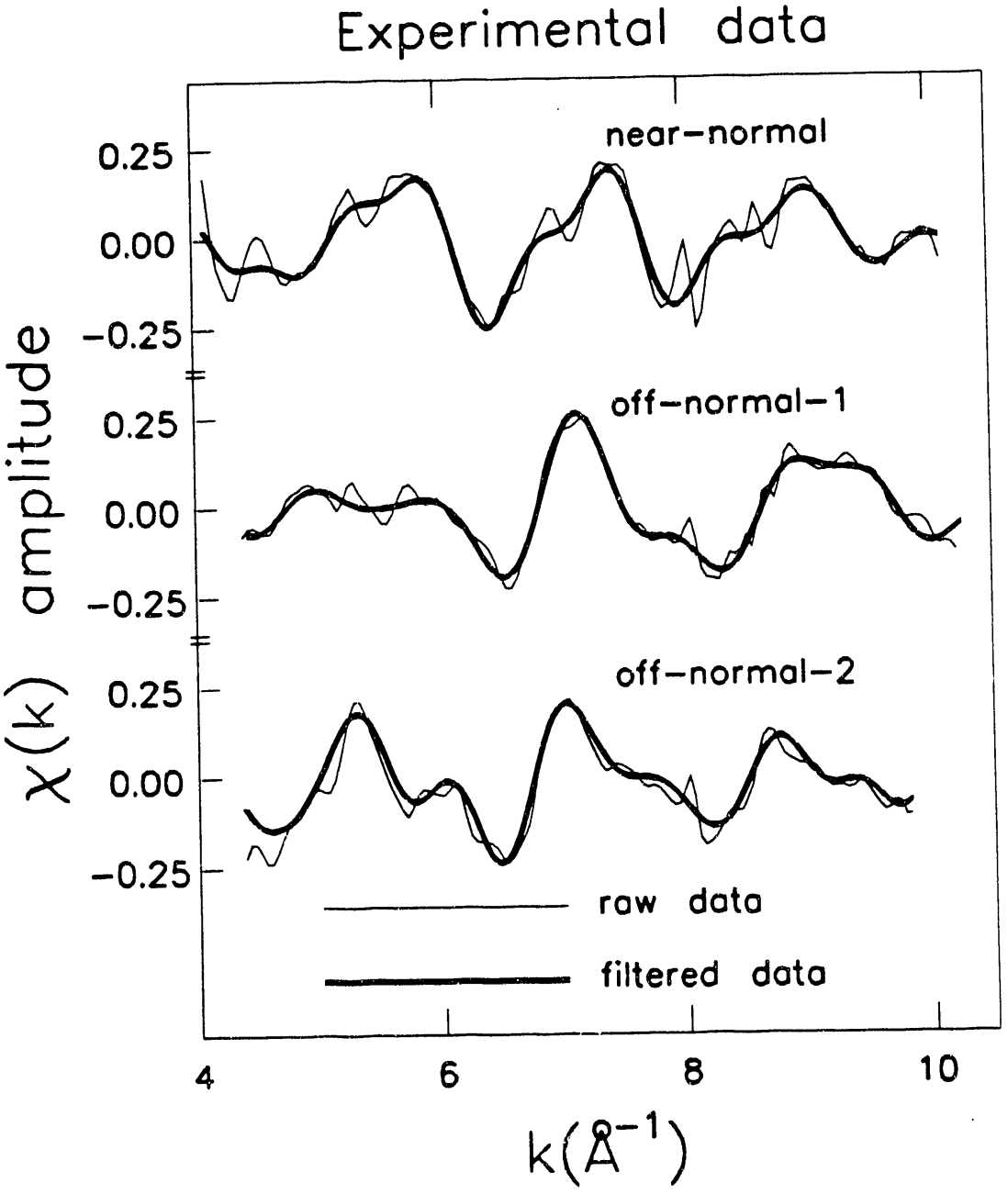
Experimental data
near-normal
off-normal-1
off-normal-2
0.25
0.00
-0.25
χ(k) amplitude
raw data
filtered data
4
6
8
10
k(Å⁻¹)

Figure 2.2

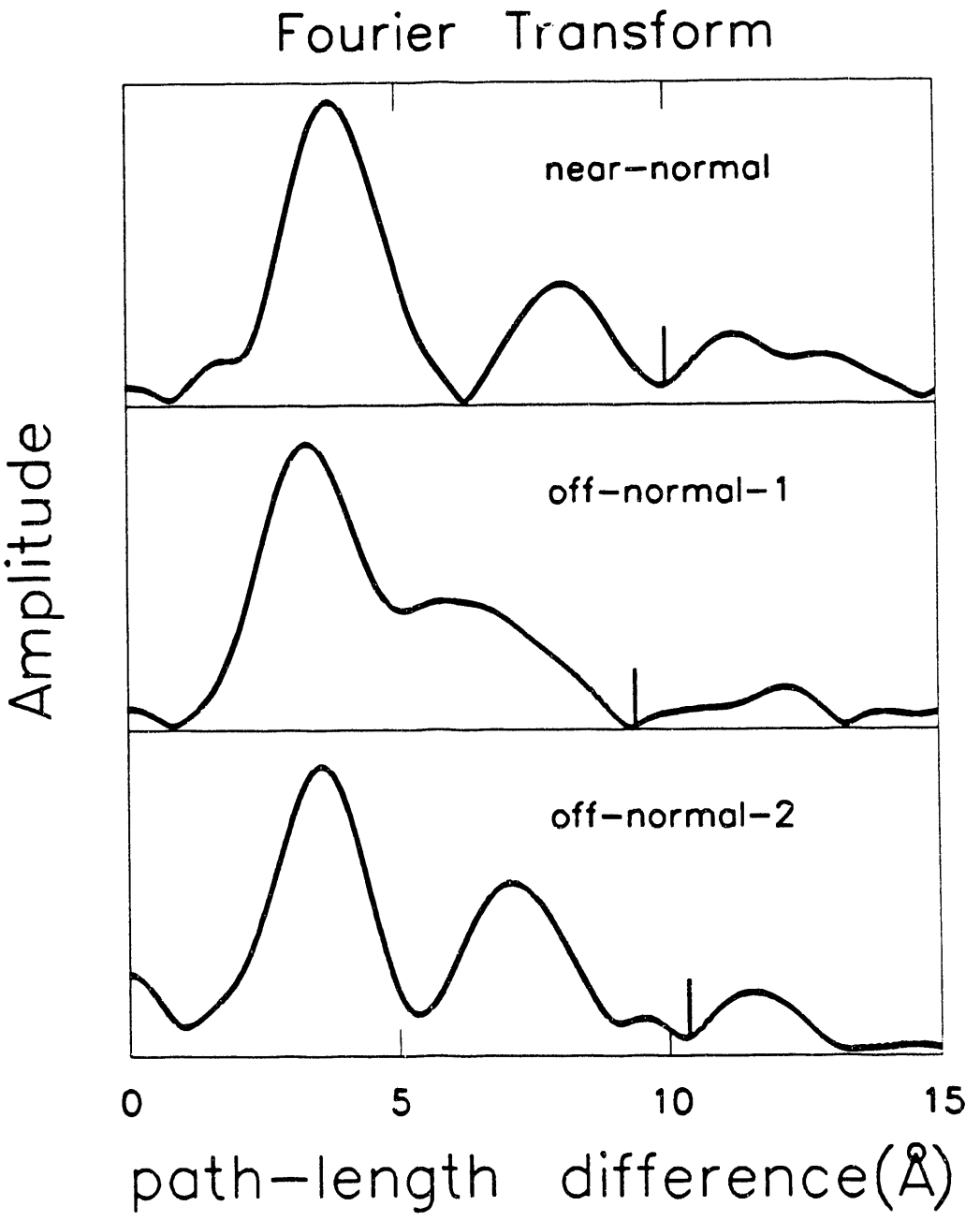
Fourier Transform
near-normal
off-normal-1
off-normal-2
Amplitude
0
5
10
15
path-length difference(Å)

Figure 2.3

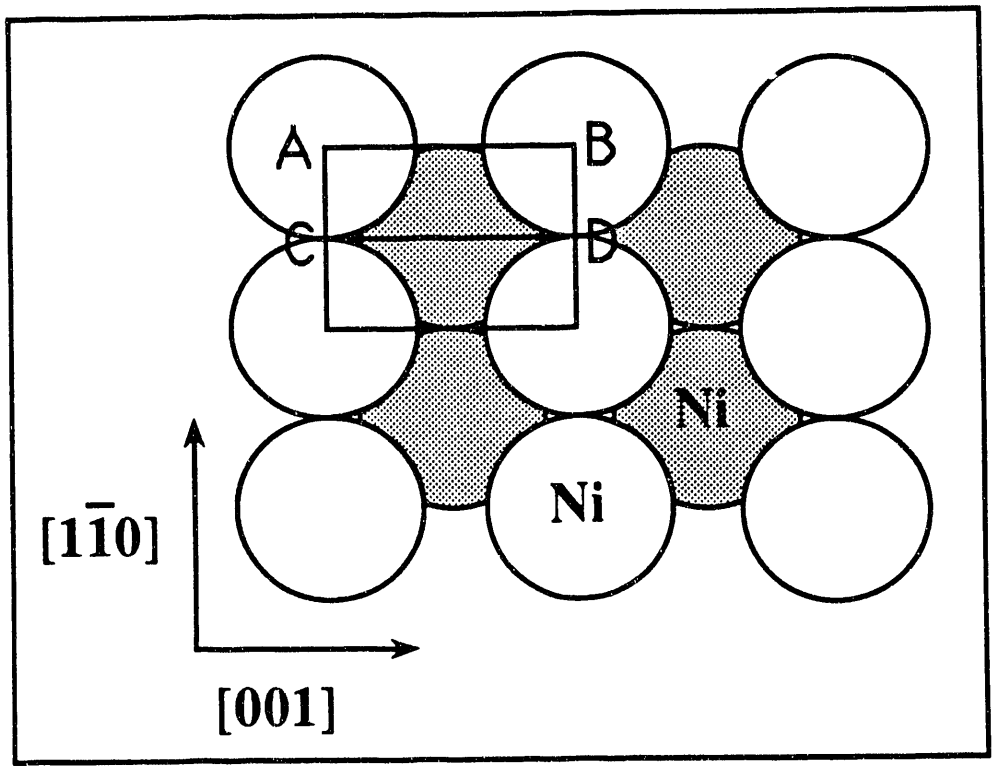


Figure 2.4

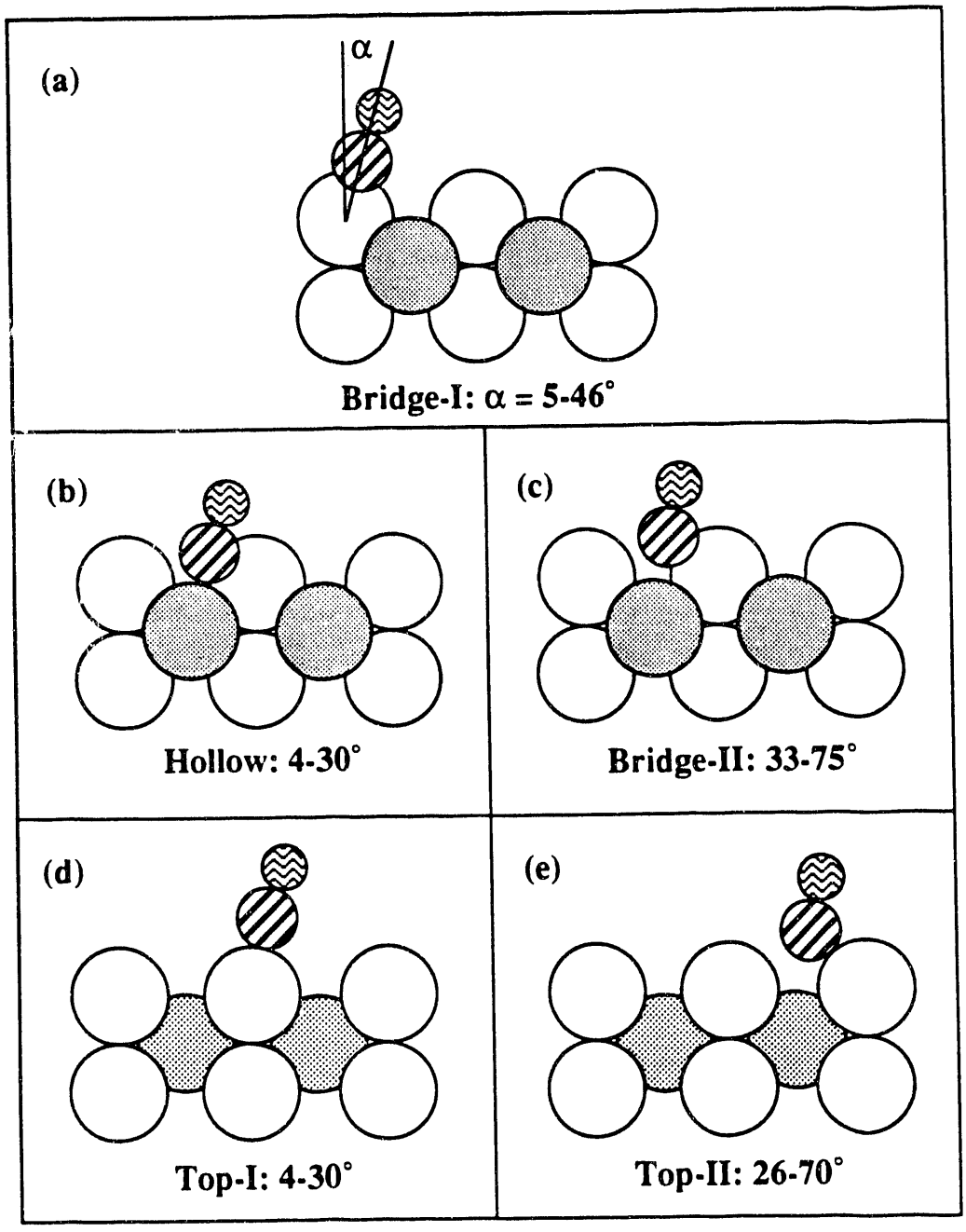
(a)
α
Bridge-I: α = 5-46°
(b)
Hollow: 4-30°
(c)
Bridge-II: 33-75°
(d)
Top-I: 4-30°
(e)
Top-II: 26-70°

Figure 2.5

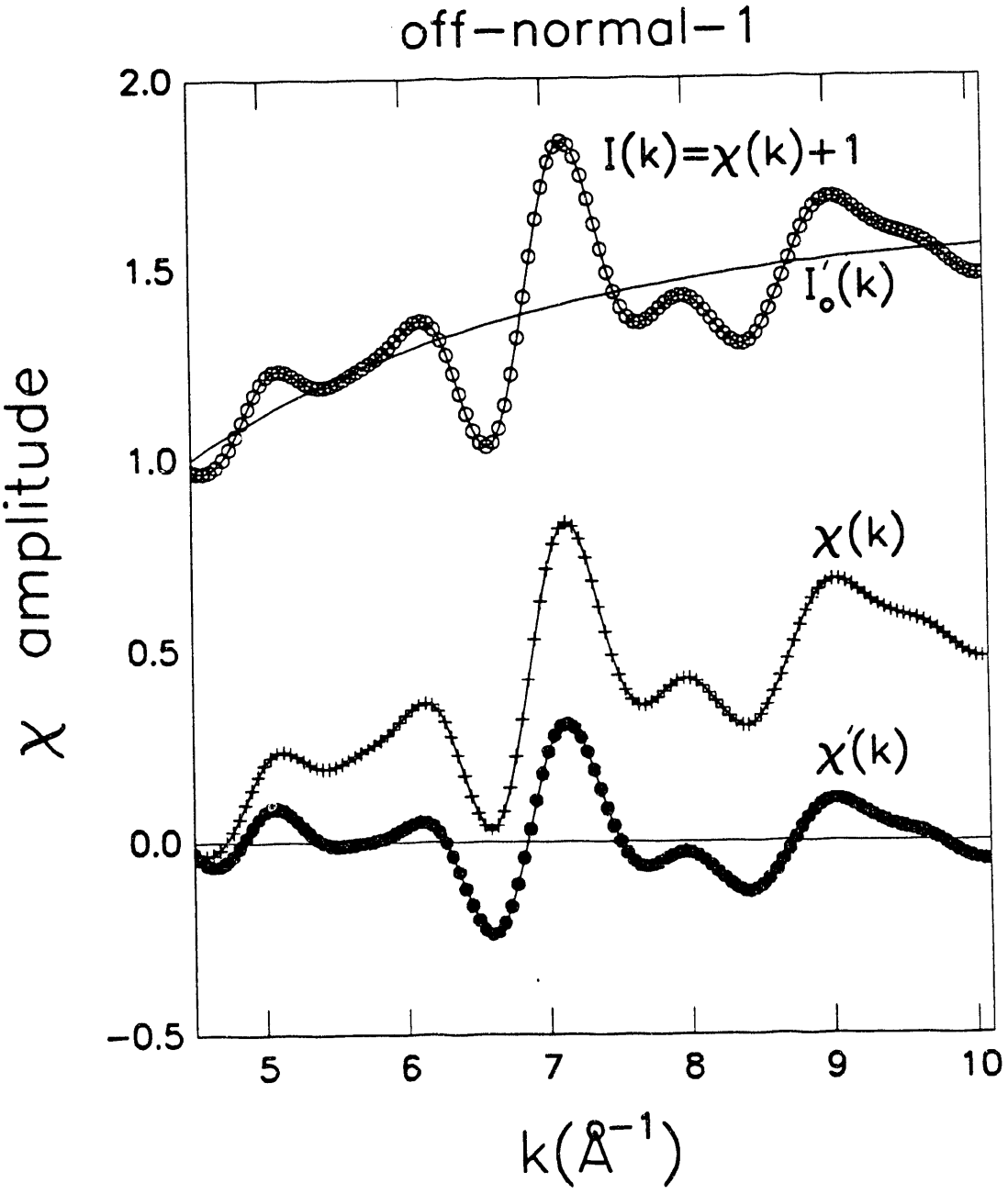
off−normal−1
I(k)=χ(k)+1
I'o(k)
χ(k)
χ'(k)
χ amplitude
2.0
1.5
1.0
0.5
0.0
−0.5
5
6
7
8
9
10
k(Å−1)

Figure 2.6

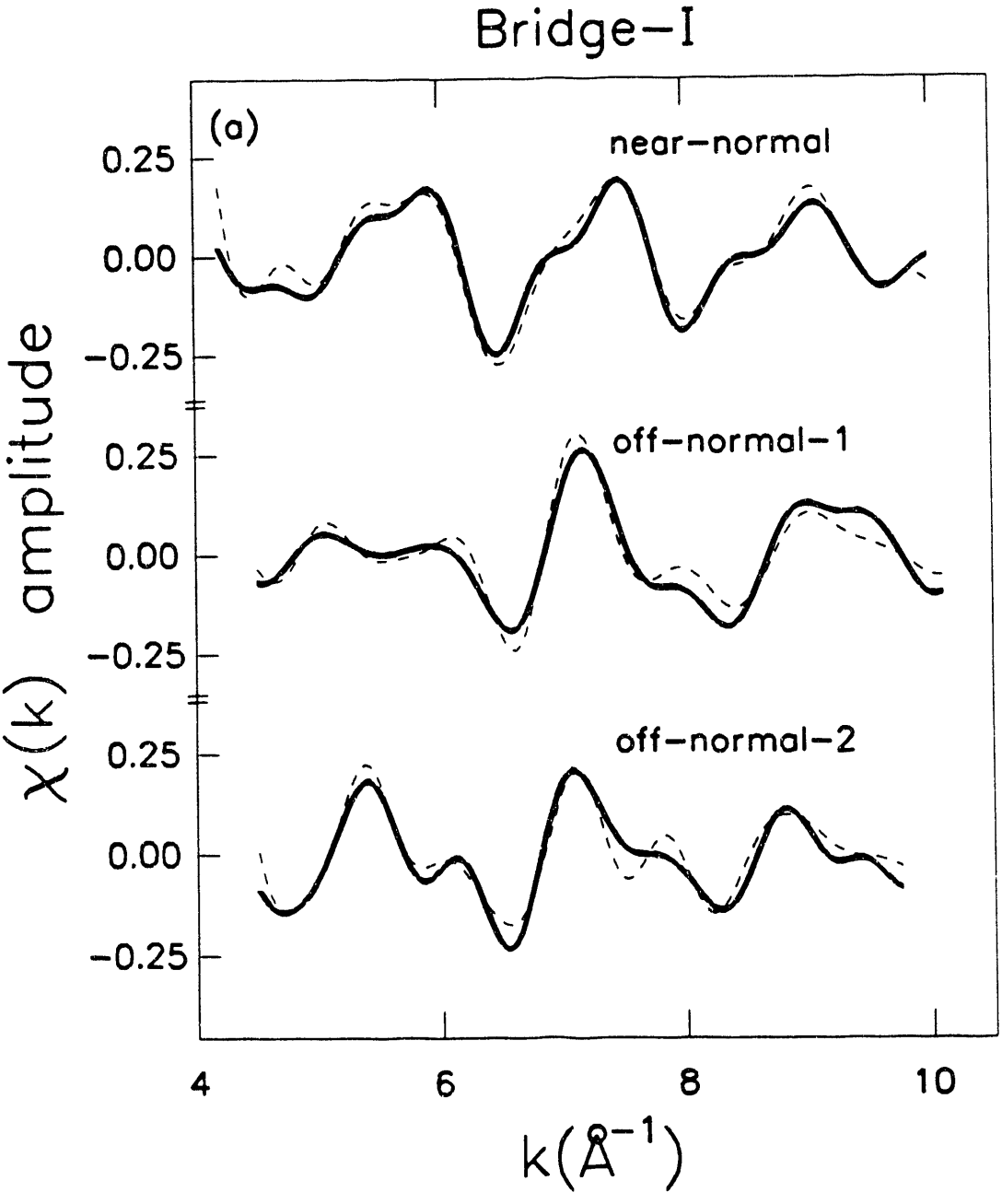
Bridge–I
(a)
near–normal
off–normal–1
off–normal–2
0.25
0.00
−0.25
χ(k) amplitude
4
6
8
10
k(Å$^{-1}$)

Figure 2.7(a)

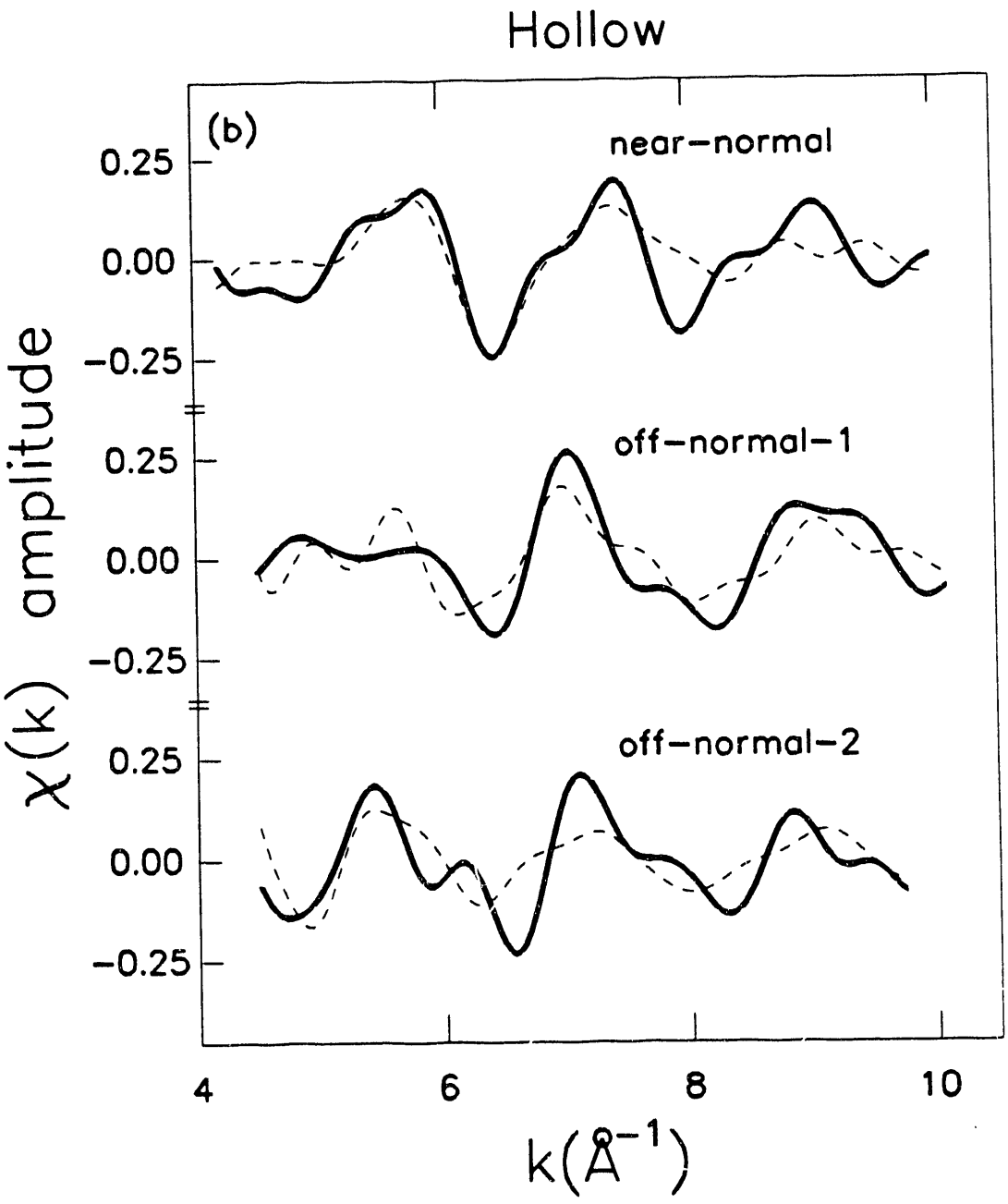
Hollow
(b)
near−normal
off−normal−1
off−normal−2
0.25
0.00
−0.25
0.25
0.00
−0.25
0.25
0.00
−0.25
χ(k) amplitude
4
6
8
10
k(Å⁻¹)

Figure 2.7(b)

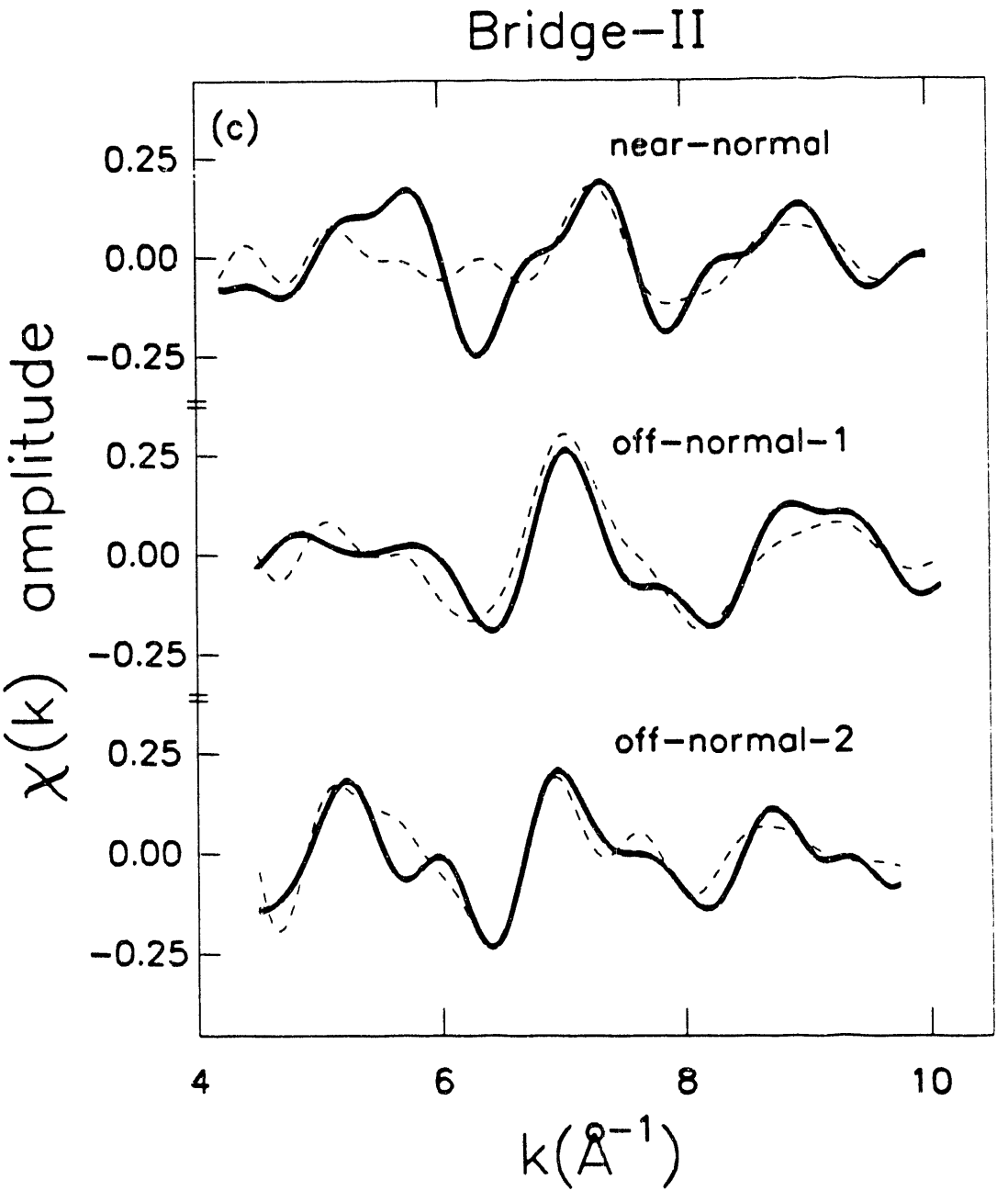
Bridge–II
(c)
near–normal
off–normal–1
off–normal–2
0.25
0.00
−0.25
χ(k) amplitude
4
6
8
10
k(Å$^{-1}$)

Figure 2.7(c)

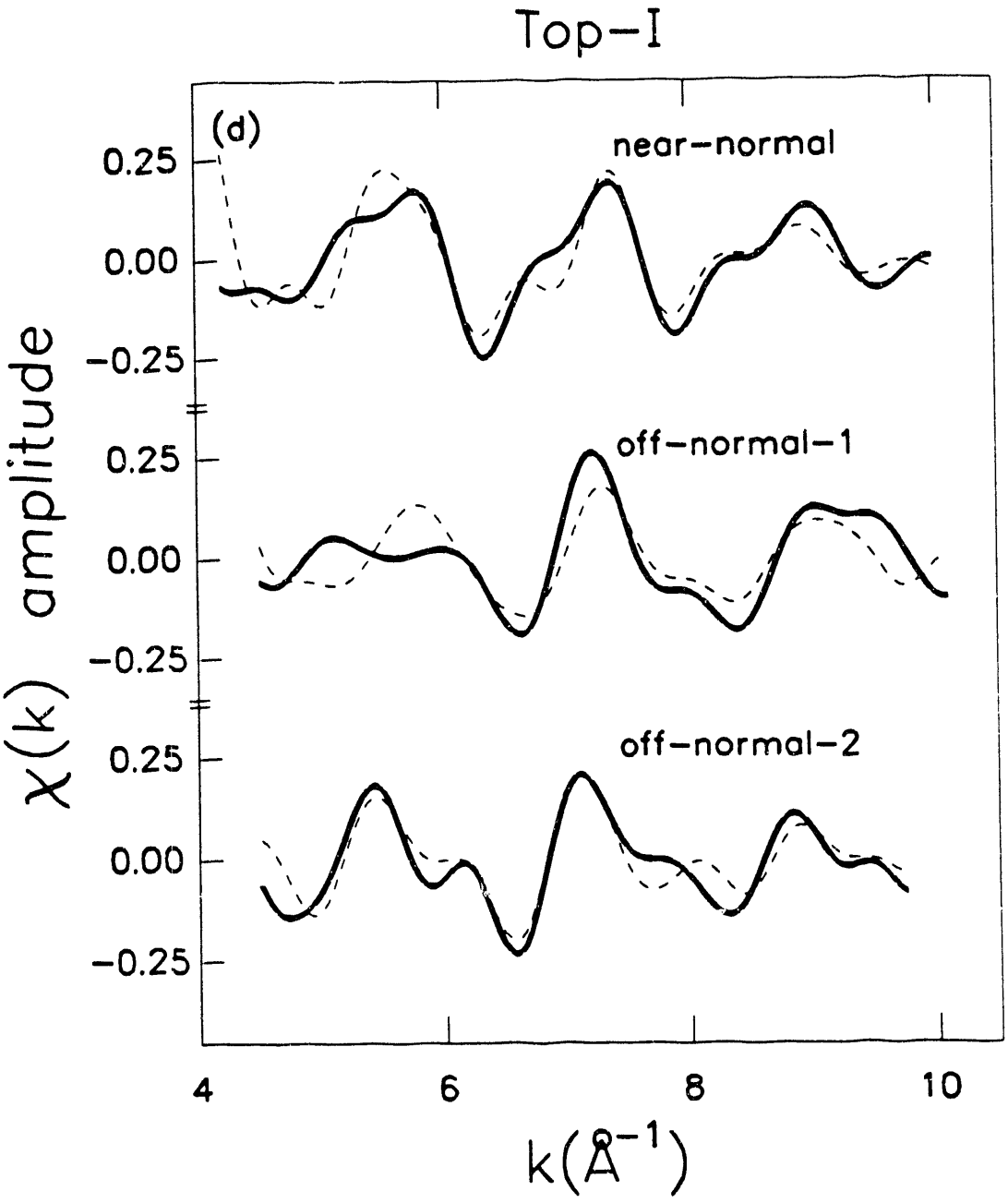
Top–I
(d)
near–normal
off–normal–1
off–normal–2
0.25
0.00
−0.25
0.25
0.00
−0.25
0.25
0.00
−0.25
χ(k) amplitude
4
6
8
10
k(Å⁻¹)

Figure 2.7(d)

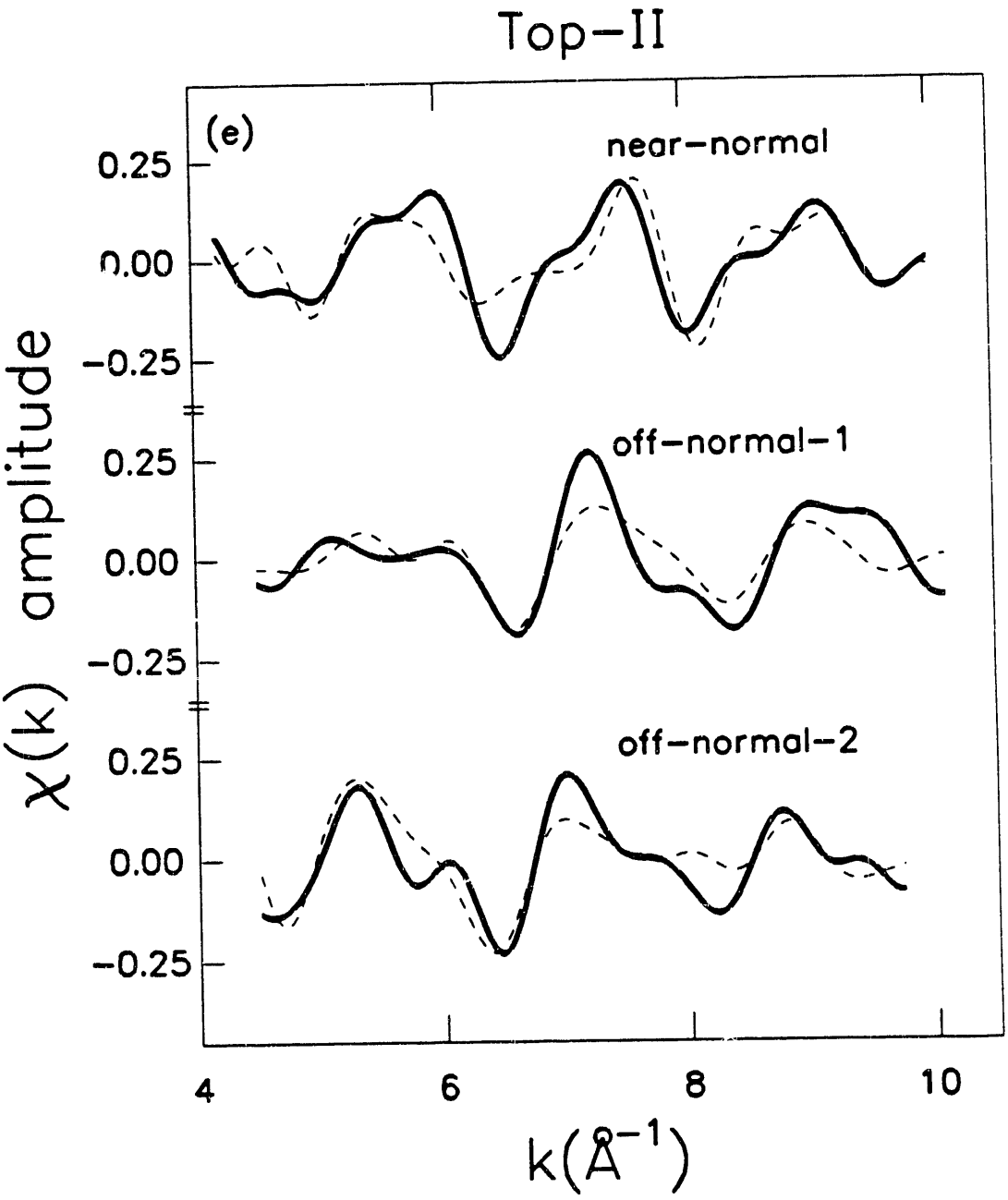
Top–II
(e)
near–normal
off–normal–1
off–normal–2
0.25
0.00
−0.25
0.25
0.00
−0.25
0.25
0.00
−0.25
χ(k) amplitude
4
6
8
10
k(Å$^{-1}$)

Figure 2.7(e)

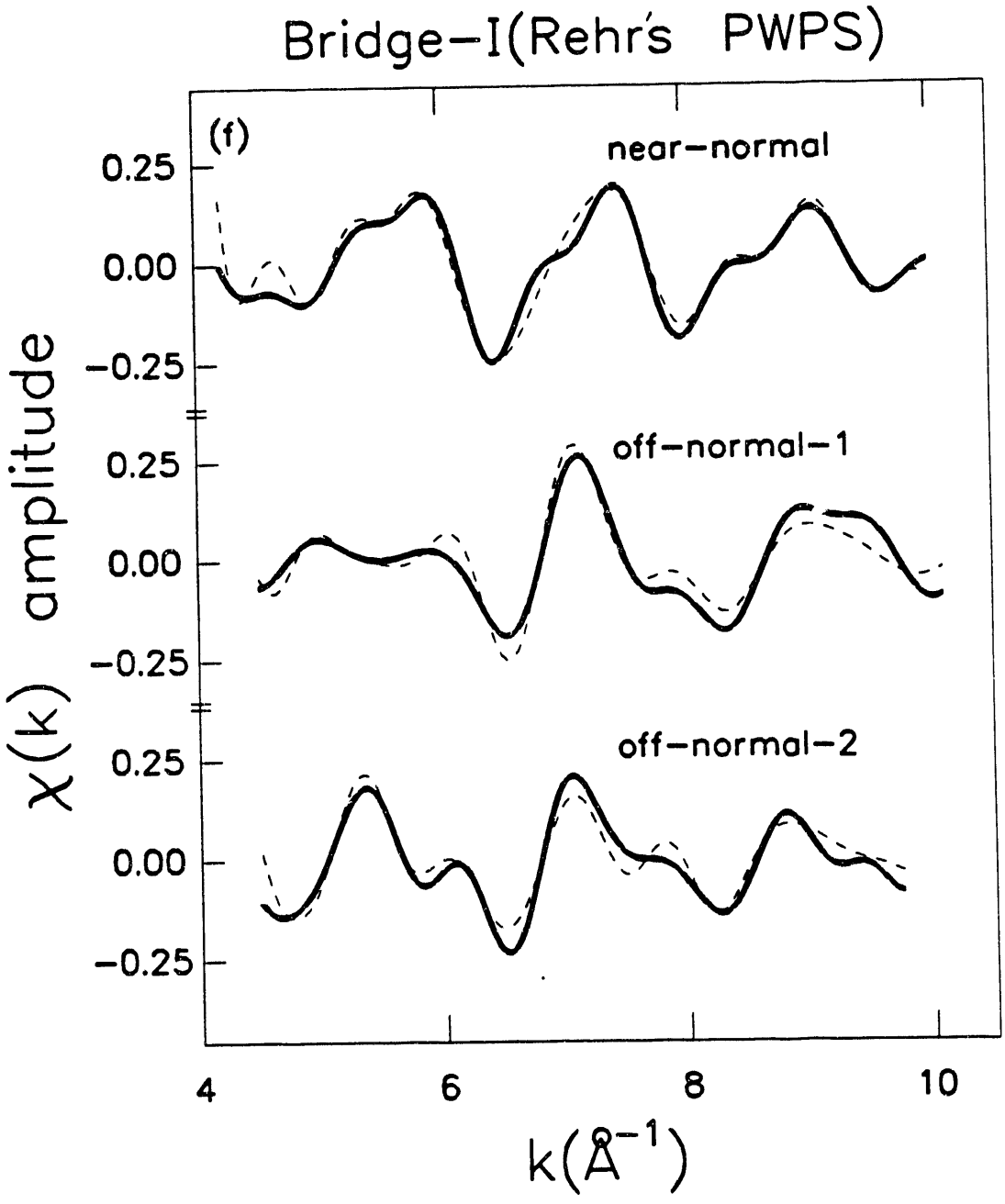
Bridge-I(Rehr's PWPS)
(f)
near-normal
off-normal-1
off-normal-2
0.25
0.00
-0.25
0.25
0.00
-0.25
0.25
0.00
-0.25
χ(k) amplitude
4
6
8
10
k(Å⁻¹)

Figure 2.7(f)

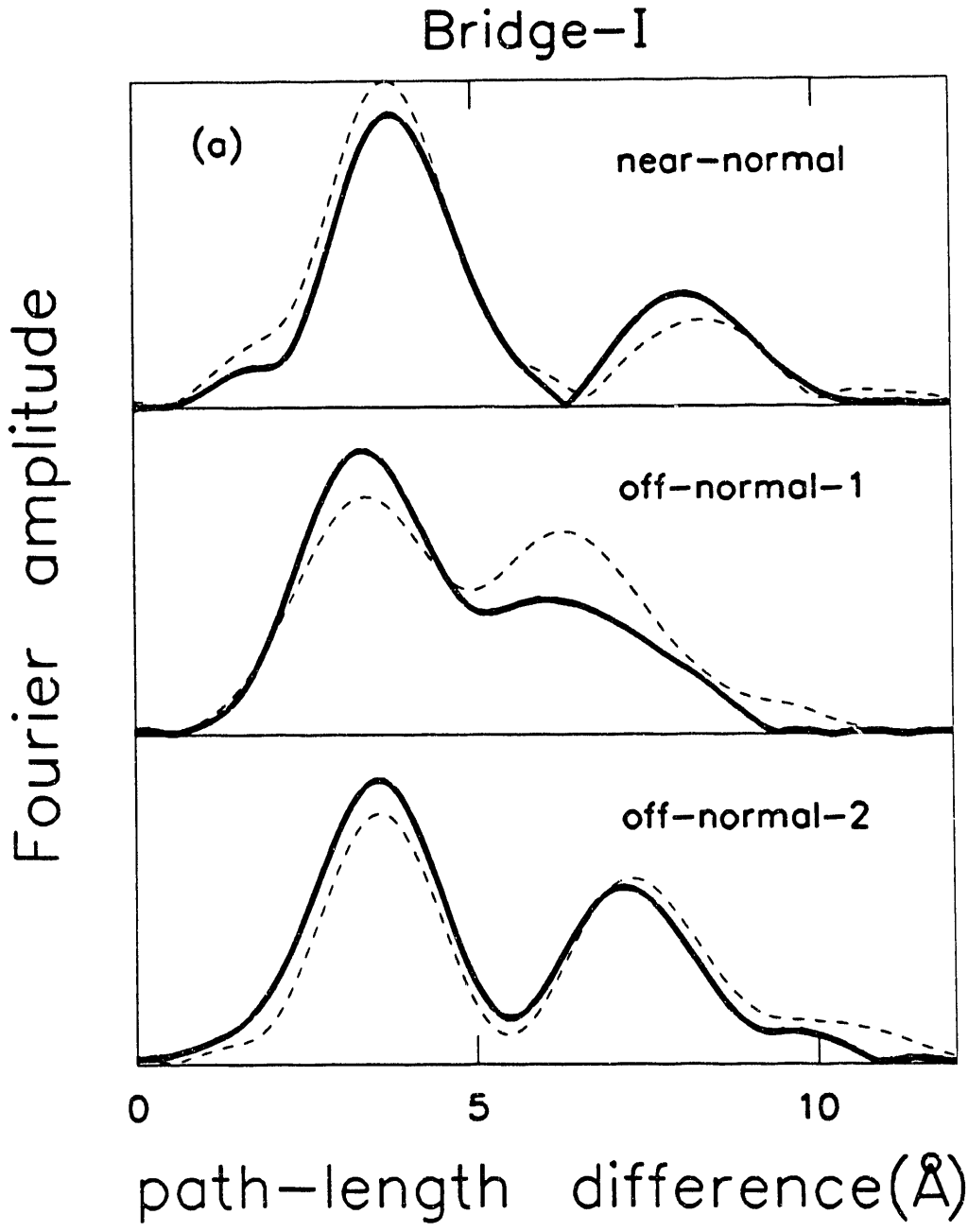
Bridge–I
(a)
near–normal
off–normal–1
off–normal–2
Fourier amplitude
0
5
10
path–length difference(Å)

Figure 2.8(a)

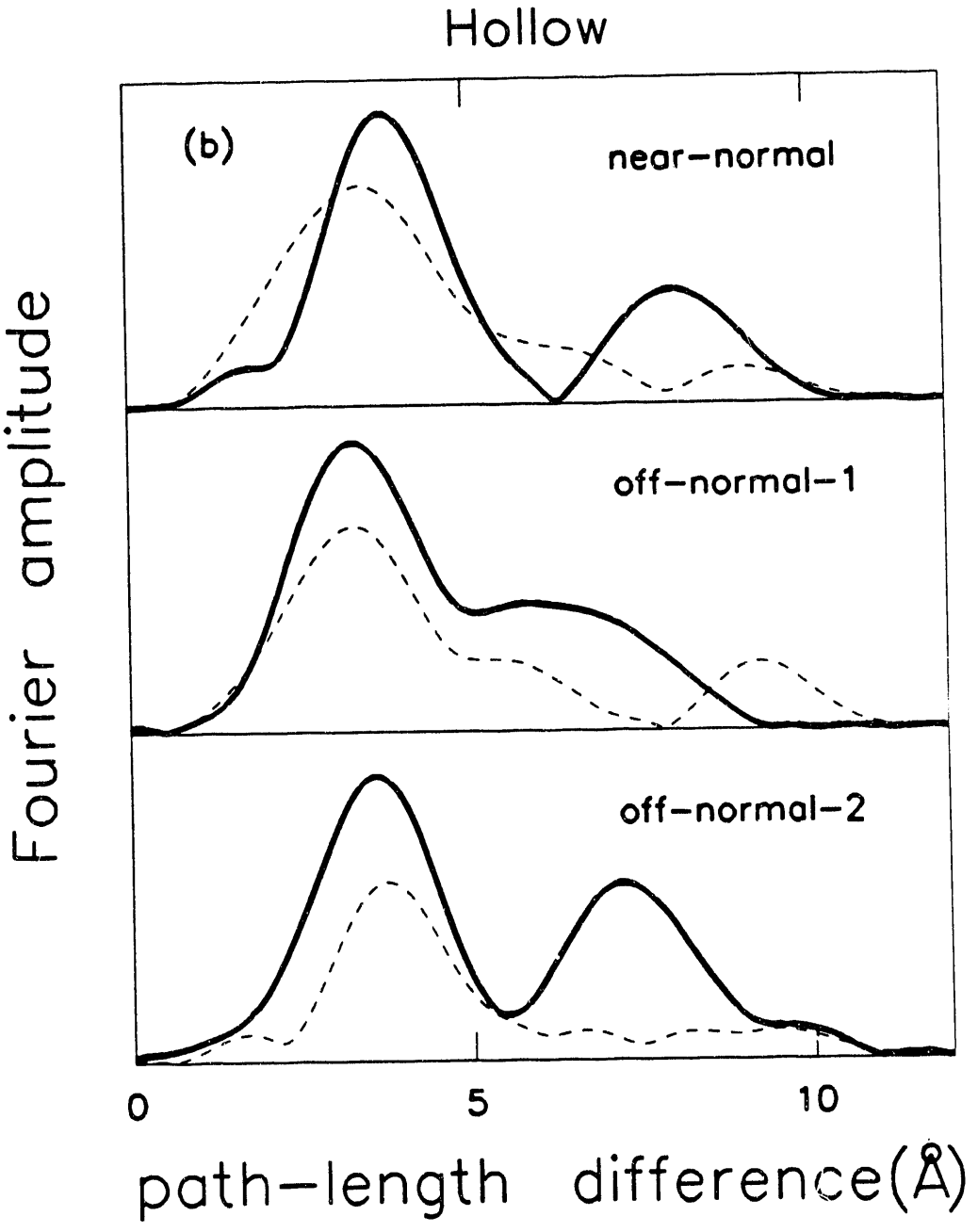
Hollow
(b)
near–normal
off–normal–1
off–normal–2
Fourier amplitude
0
5
10
path–length difference(Å)

Figure 2.8(b)

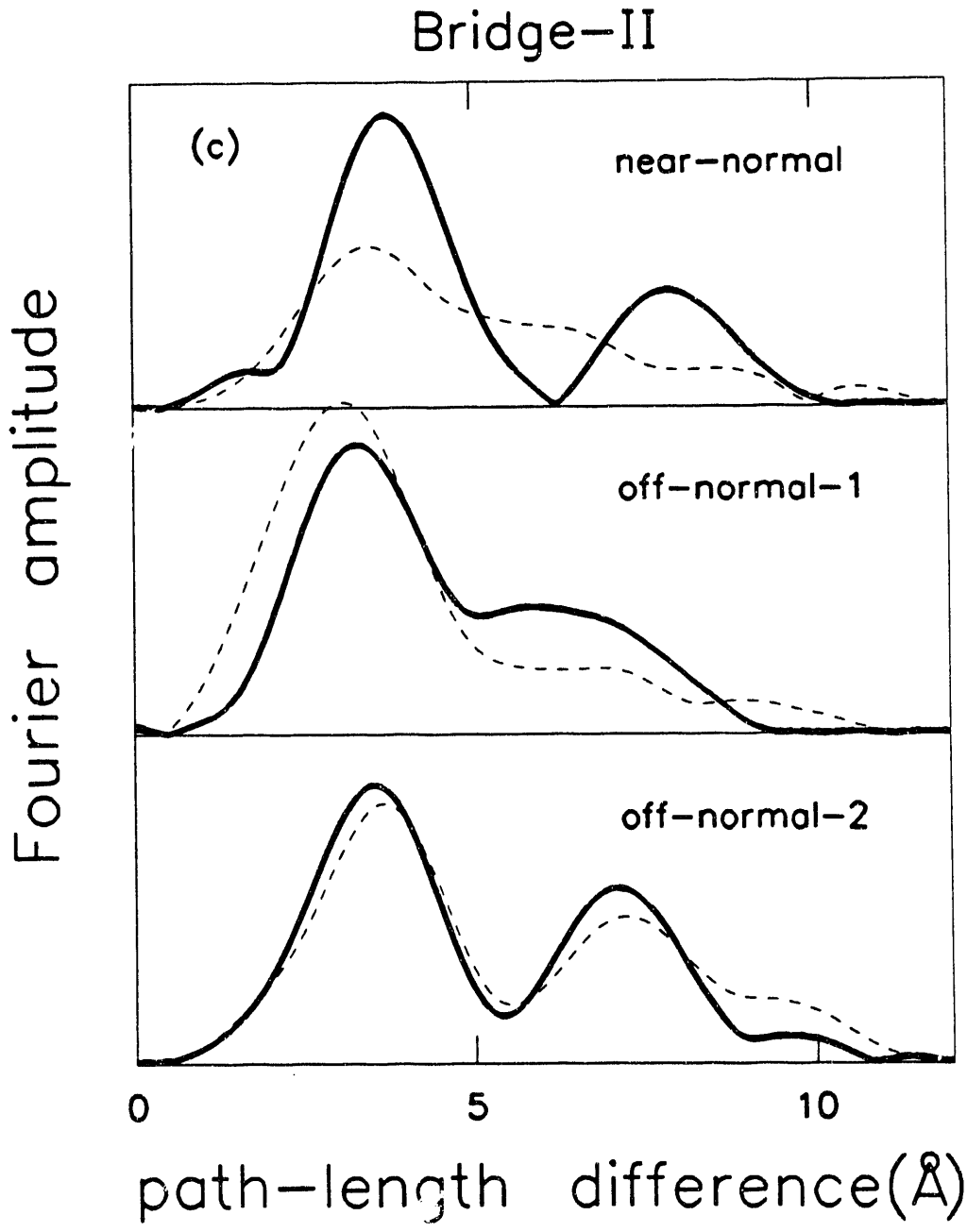
Bridge–II
(c)
near–normal
off–normal–1
off–normal–2
Fourier amplitude
0
5
10
path–length difference(Å)

Figure 2.8(c)

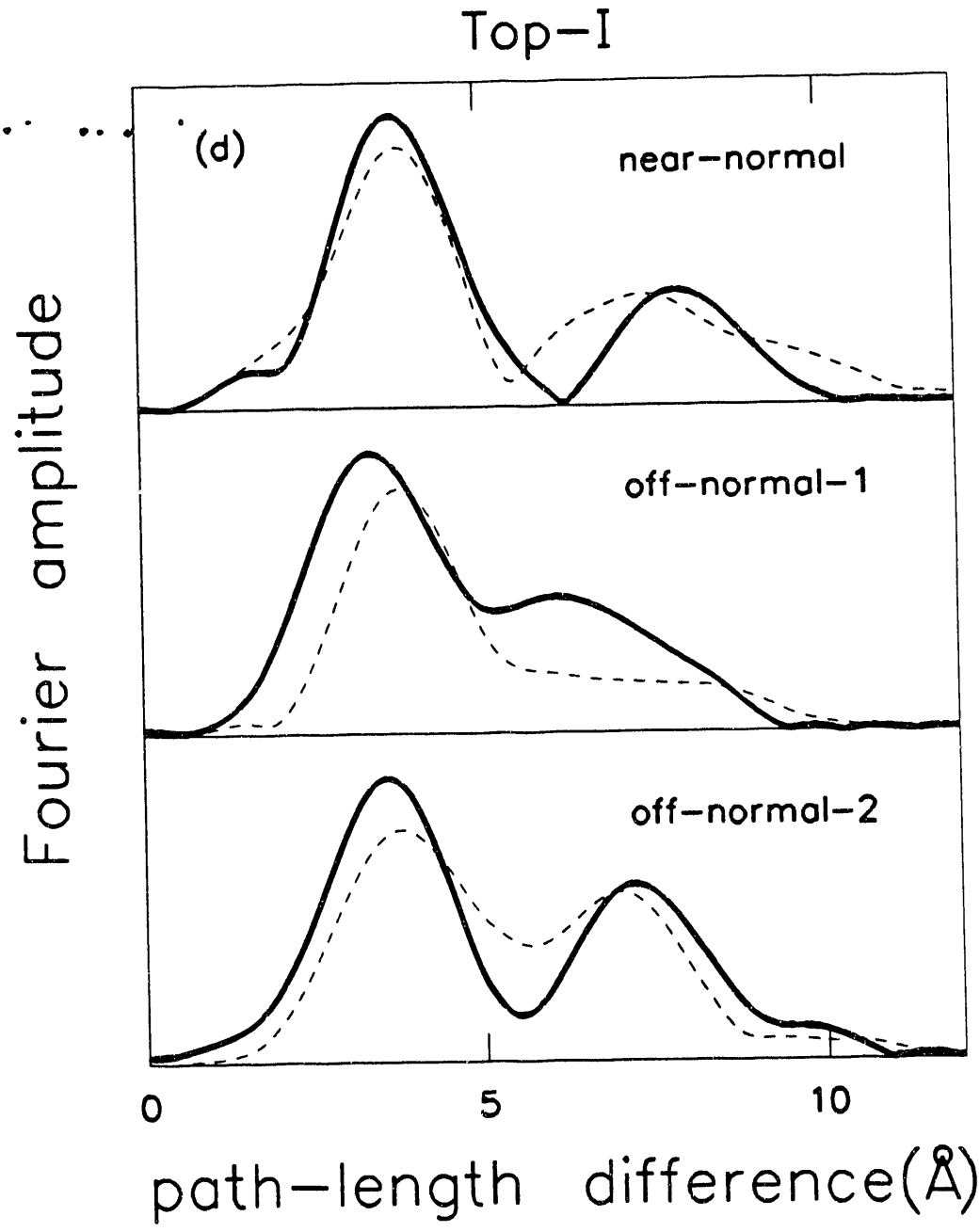
Top-I
(d)
near-normal
off-normal-1
off-normal-2
Fourier amplitude
0
5
10
path-length difference(Å)

Figure 2.8(d)

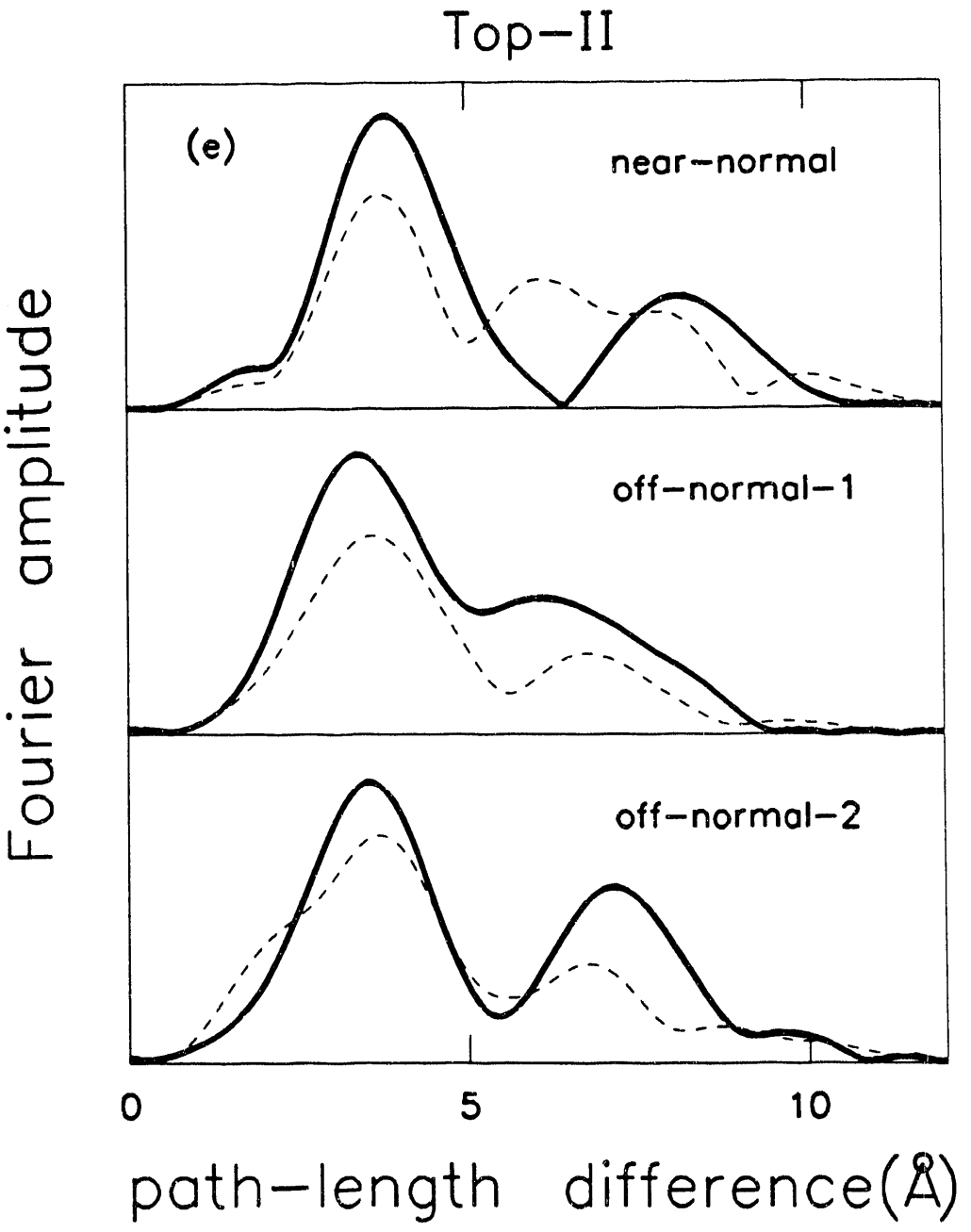
Top–II
(e)
near–normal
off–normal–1
off–normal–2
Fourier amplitude
0
5
10
path–length difference(Å)

Figure 2.8(e)

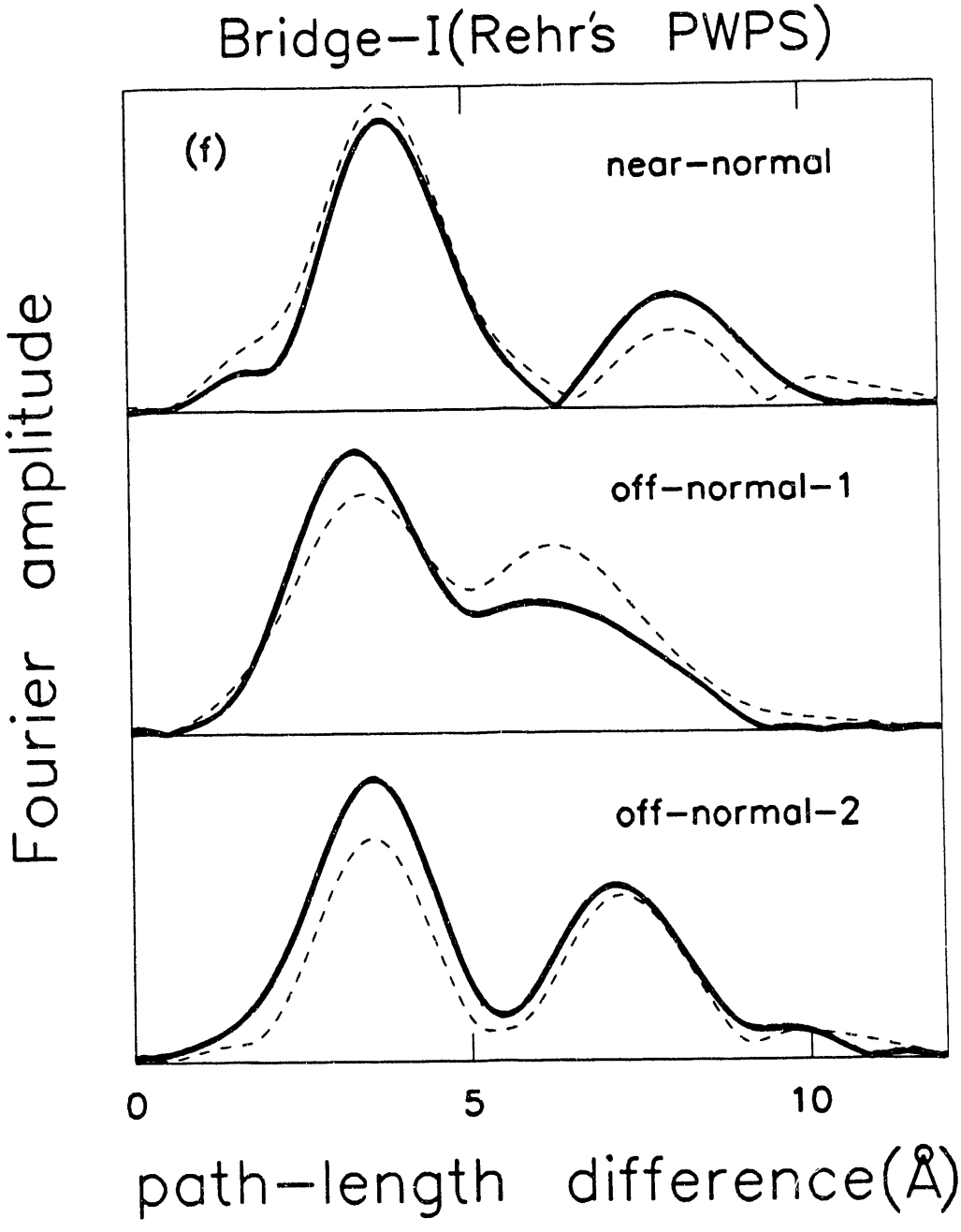
Bridge–I(Rehr's PWPS)
(f)
near–normal
off–normal–1
off–normal–2
Fourier amplitude
0
5
10
path–length difference(Å)

Figure 2.8(f)

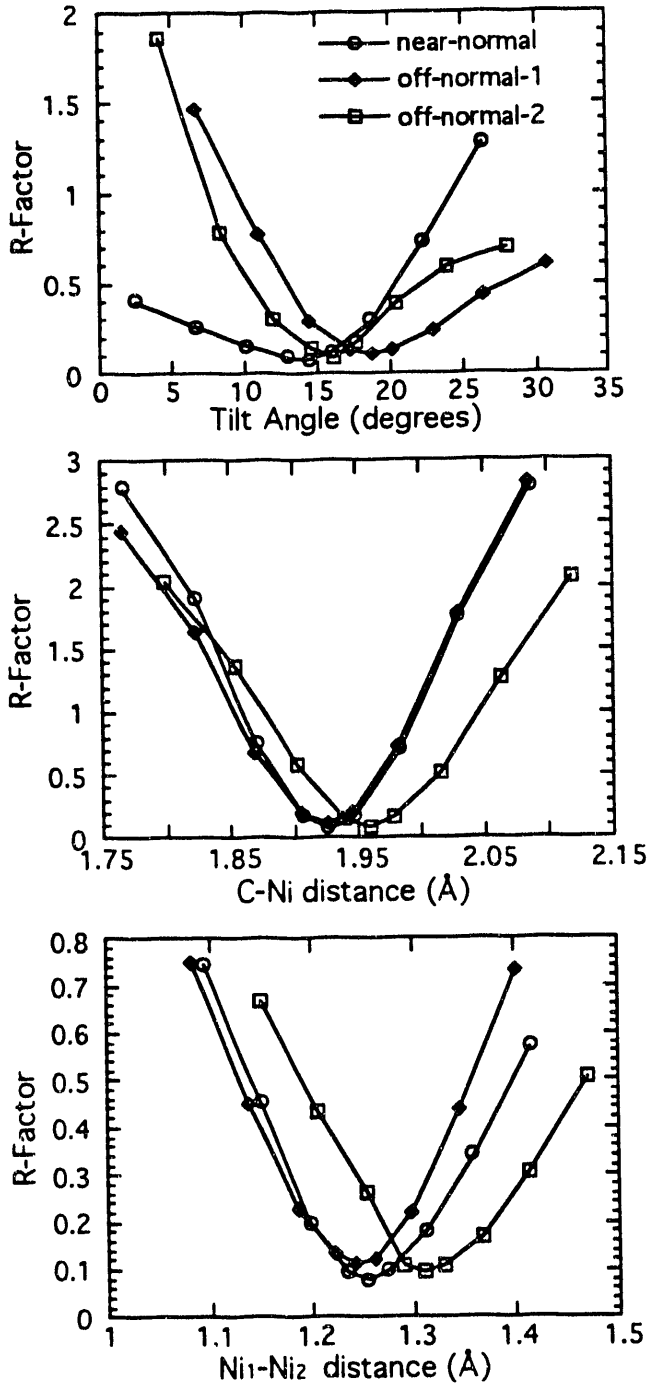
near-normal
off-normal-1
off-normal-2
R-Factor
Tilt Angle (degrees)
C-Ni distance (Å)
Ni1-Ni2 distance (Å)

Figure 2.9

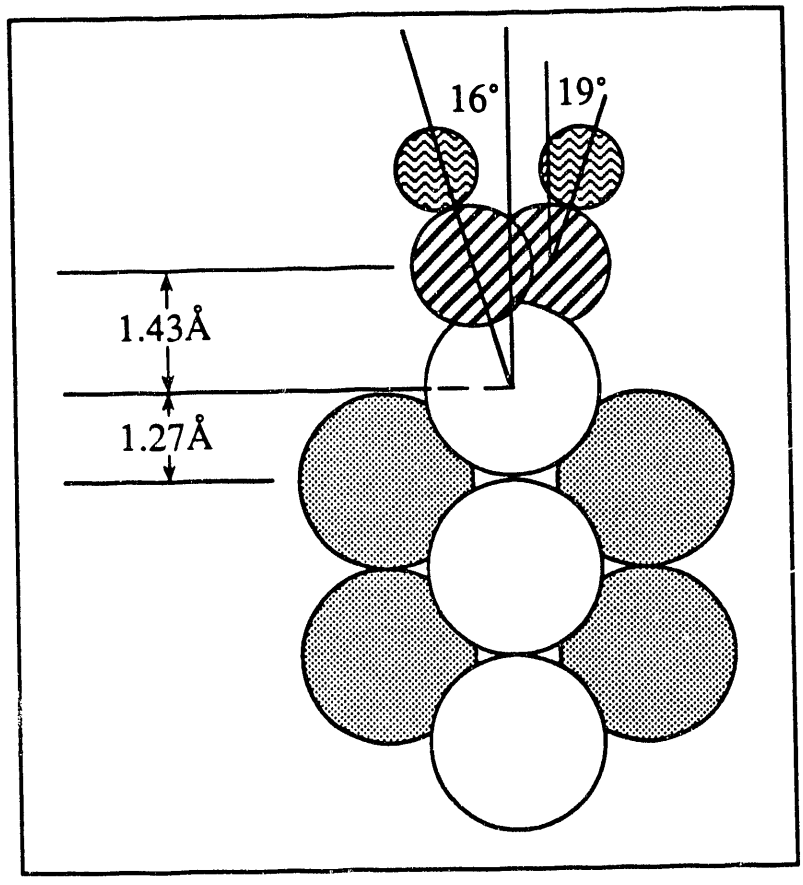


Figure 2.10

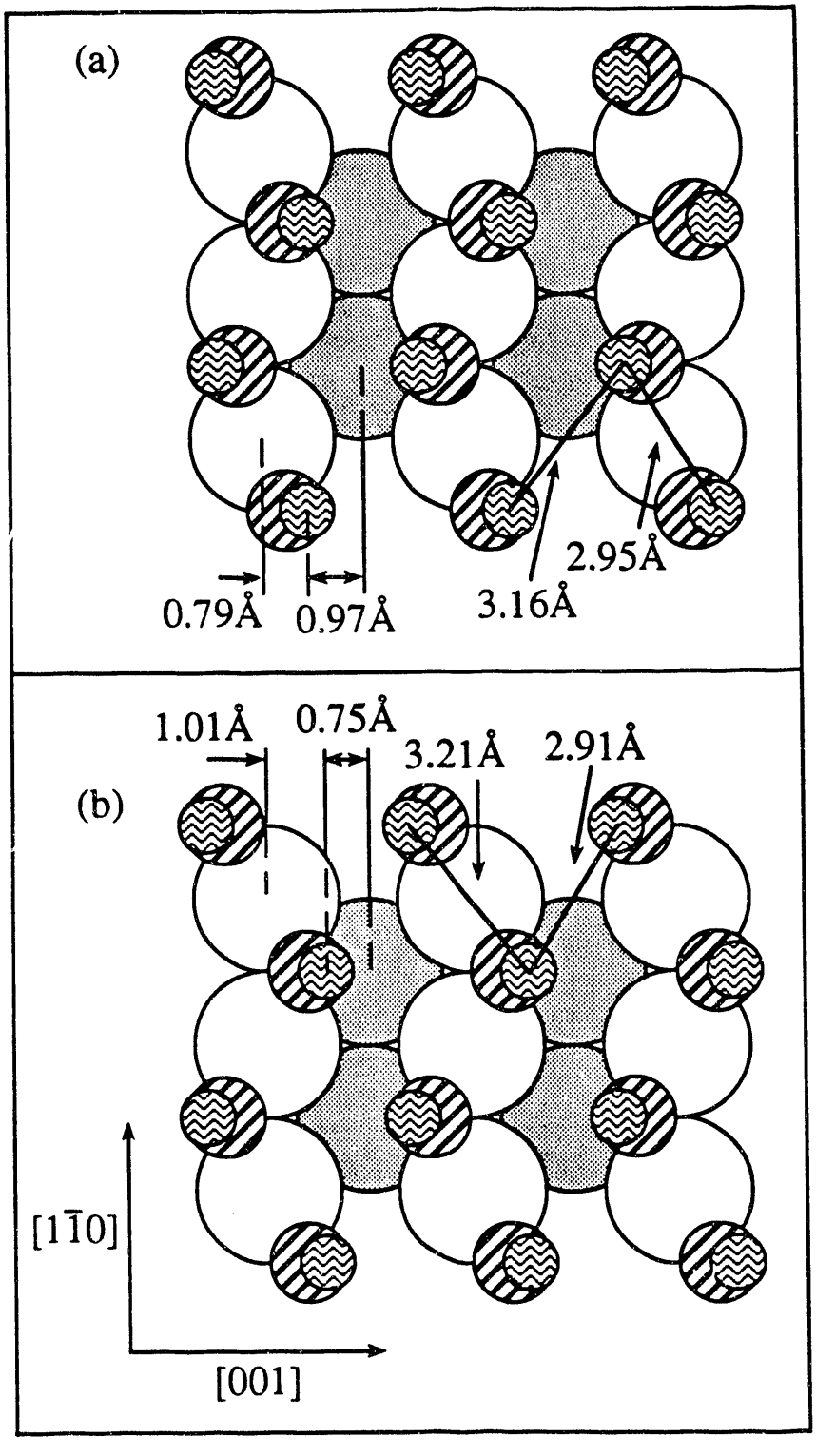


Figure 2.11

# Chapter 3

# ARPEFS Study of the Structure of p(2×2)K/Ni(111)

## Abstract

Angle-resolved photoemission extended fine structure (ARPEFS) from the potassium 1s core level was measured for the quantitative structural determination of the p(2×2)K/Ni(111) overlayer at 130K. This is the first ARPEFS study of an alkali-metal adsorption system. Our analysis of the ARPEFS $\chi(k)$ curves detected along [111] and [771] showed that the potassium atoms are preferentially adsorbed on the atop sites, in agreement with a previous low energy electron diffraction (LEED) study of the same system. The K-Ni bond length is 3.02 ± 0.01Å, yielding an effective hard-sphere radius of 1.77Å for potassium. The first-to second-layer spacing of nickel is 1.90 ± 0.04Å, a 6.5% contraction from the bulk spacing of 2.033Å. Furthermore, the first nickel layer shows neither lateral reconstruction (0.00 ± 0.09Å) nor vertical corrugation (0.00 ± 0.03Å). A comparison of the structural parameters with those determined from the LEED study is presented. The limitations of Fourier analysis for site determination and the importance of comparing ARPEFS experimental data with theoretical simulations in both k space and r space are also discussed.

# 3.1 INTRODUCTION

Recently there has been increasing interest in, and controversy over, the structure and bonding of adsorbed submonolayer alkali metals on surfaces.[1-4] Alkali metals have long been known[5] to lower the work function of both metals and semiconductors substantially when adsorbed on these surfaces, and have been widely used in technological applications such as heterogeneous catalysis[6] and thermionic energy conversion.[7] Extensive experimental[1,3,4] and theoretical[2,8,9] work has been undertaken to study the chemical bonding between the adsorbed alkali atoms and the metal substrate. While it has long been held[1] that this bonding is mainly ionic at low coverage due to the charge donation by the strongly electropositive alkali metals, and then becomes more metallic at higher coverage due to the depolarization of the adsorbate dipoles, some recent studies[2,3,9] have suggested that there is no charge transfer at all coverages, and the adsorbate-substrate bonding is better described as covalent at low coverage and metallic at high coverage.[3]

Few complete determinations of the adsorption geometries of the alkali-metal overlayers have been reported, probably due to the relatively complex phase diagrams of these systems where commensurate structures are usually possible only within small coverage and temperature ranges. Among the structures determined, an interesting trend is that the alkali atoms are found to adsorb on the atop sites for p(2×2) structures formed at 0.25 monolayer coverage on the close-packed hexagonal surfaces, as demonstrated in the Low Energy Electron Diffraction (LEED) studies of p(2×2)Cs/Cu(111) (Ref. 10) and more recently, of p(2×2)Cs/Rh(0001) (Ref. 11) and p(2×2)K/Ni(111) (Ref. 12). These

studies also showed that the effective hard-sphere radius (adsorbate-substrate bond-length less the metallic radius of the substrate) of the atop-adsorbed alkali metal is much smaller than its metallic radius. For Cs/Rh(0001) it was found that at the higher coverage of 0.33 monolayer, where the cesium overlayer forms a $\sqrt{3}\times\sqrt{3}$ R30° structure, the Cs atoms are favored to adsorb on the three-fold hollow sites and have larger hard-sphere radii (+0.3Å) than in the p(2×2) structure. A recent normal incidence standing X-ray wave-field absorption (NISXW) study[13] of Rb/Al(111), however, showed that the Rb atoms are adsorbed on the top sites and that the Rb-Al bond length does not change (±0.10Å) over the coverage range 0.12-0.33 monolayers. Again, interpretations of the coverage dependence (or independence) of adsorption site and bond length cover both the ionic-metallic and covalent-metallic bonding models. It appears that the nature of the chemical bonding is a complicated function of the metals involved, the surface atomic density and symmetry, and the coverage of the alkali atoms. More experimental and theoretical studies are needed to further the understanding of the chemistry of alkali-metal adsorbates on metal surfaces.

In this chapter we report the structural study of the p(2×2)K/Ni(111) surface using angle-resolved photoemission extended fine structure (ARPEFS).[14] Most earlier ARPEFS work has concentrated on the atomic overlayers of phosphorus, sulfur, and chlorine on surfaces.[14-17] With the exception of (1×1)P/Ge(111) (Ref. 16), all these atomic species were found to occupy high-symmetry sites — the highest coordination sites (hollow sites) for adsorption on metals and lower coordination sites (bridge sites) for adsorption on semiconductors. A recent study of the unusual p2mg(2×1)CO/Ni(110) structure[18] extended the application of ARPEFS to the study of molecules adsorbed on

surfaces. It also demonstrated that ARPEFS is capable of determining the structures of more complex systems, in this case a surface layer with two inequivalent molecules in a unit cell and tilted molecules occupying positions that are displaced from high-symmetry sites. The structural study of the p(2×2)K/Ni(111) surface reported here represents the extension of the ARPEFS technique to the study of yet another type of surface overlayer, the adsorption of metals on other metal substrates. It is important that structural determination of surface overlayers be confirmed by more than one technique. The recent LEED study[12] of the p(2×2)K/Ni(111) adsorption system by Fisher *et al.*, in which the potassium atoms were found to adsorbed on atop sites with a rather short K-Ni bond length of 2.82Å, provides an opportunity for comparison of the structural results for this system.

The ARPEFS technique used in this work has been described in detail elsewhere.[19] A brief summary is given here. In an ARPEFS study, the photoemission partial cross-section of a core level (such as the 1s level) of the adsorbed atoms is measured in one or more emission directions as a function of the photoelectron kinetic energy in the range of approximately 50-500eV. Because the photoelectron wave is emitted in all directions (p-wave for 1s electrons), part of the wave will have been scattered by nearby substrate and adsorbate atoms before it reaches the detector. The scattered waves and the unscattered wave undergo interference, either constructively or destructively depending on their path-length differences and the electron kinetic energy. The interference pattern shows up in the measured energy-dependent photoelectron intensity as peaks and valleys in the otherwise slowly-varying atomic-like cross section. This oscillatory part, which contains information about the local

geometry of the photoemitting atom, is what constitutes the ARPEFS. Experimental ARPEFS curves could in many simple cases be Fourier-transformed to obtain qualitative structural information such as adsorption sites and approximate interatomic distances, while comparison with multiple-scattering spherical wave (MSSW) calculations is necessary for a quantitative determination of the structure.

This chapter is organized as follows: Section 3.2 describes the experiment, in particular the preparation of potassium overlayers and the collection of potassium 1s photoemission data. Section 3.3 gives a brief account of the procedure used to reduce experimental photoemission spectra into an ARPEFS curve. Section 3.4 describes a detailed analysis of the surface structure and presents optimized structural parameters and their estimated errors. Section 3.5 discusses the results of this work and compares them with results from the LEED study.

## 3.2 EXPERIMENT

The experiments were performed in an ion-pumped ultrahigh-vacuum chamber with a typical base pressure of $7\times10^{-11}$ Torr. The Ni(111) crystal was cleaned by the standard method of repeated cycles of sputtering and annealing prior to this work. Laue backscattering verified its orientation to be within $\pm1^\circ$ of the (111) plane. The crystal was then spot-welded between two tungsten wires onto a tantalum plate that was mounted on a high-precision manipulator equipped with a liquid-nitrogen cooling system. The manipulator allowed linear motions along three perpendicular axes as well as rotations in both the polar and

the azimuthal angles. To accommodate the azimuthal rotation, cooling of the sample was accomplished by attaching the tantalum plate to a copper liquid-nitrogen reservoir through a thick, but flexible, copper braid. With this setup the crystal could be cooled to around 120-130K. The temperature of the crystal was measured using a chromel-alumel thermocouple spot-welded to the tantalum plate and very close to the Ni crystal. The readings of the thermocouple were calibrated at higher temperatures using an optical pyrometer. Routine sample cleaning was done by sputtering with a 500 - 1000eV $Ar^+$ beam and annealing at 800 - 1000K with electron-beam bombardment from behind the crystal. To remove the carbon contaminant more effectively, the sample was occasionally exposed to 1-5L of $O_2$ at room temperature before the annealing. The surface was considered clean when LEED showed sharp (1×1) pattern with little background, and Auger electron spectroscopy (AES) revealed no impurities.

Potassium was evaporated onto the Ni(111) surface from commercial alkali-metal dispensers (SAES Getters). Three potassium dispensers were mounted on a flange previously used for titanium sublimation-pump filaments. This configuration allows a long total evaporation time without the chamber having to be vented for replacement of K sources. The flange was placed in a stainless steel enclosure with a three-quarter inch opening that allowed the potassium vapor to be directed at the Ni surface with minimum contamination to other parts of the chamber. A shuttle installed behind the opening provided accurate timing of potassium evaporation. Each source was outgassed at a current of 3-4 Amp for two to three days. During this period the source was also brought to gradually higher current (up to the operating current of ~6-6.5 Amp for potassium deposition) briefly until the pressure inside the chamber did not rise by more than

$1\times10^{-10}$ Torr during evaporation. Relative coverage was assumed to be proportional to evaporation time, while the absolute coverage was calibrated to the evaporation time required to produce the p(2×2) LEED pattern that should appear at 0.25 monolayer (one potassium atom for every four surface Ni atoms). This work was mainly concerned with the commensurate p(2×2) structure, and evaporation was stopped when a low-background, sharp p(2×2) LEED pattern appeared. The Ni(111) substrate was held at room temperature during potassium deposition. The crystal was then cooled to ~130K for low-temperature measurements. It was found[12] that if ~0.25 monolayer of potassium was adsorbed on Ni(111) at 120K and the crystal was heated to ~225K, the p(2×2) LEED spots would become *irreversibly* sharper, indicative of some type of "frozen-in" disorder for adsorption at 120K that could be "annealed" into large crystallites at ~225K. If the depositions were undertaken at 293K to form the p(2×2) structure and then cooled to 120K, the overlayer remained well-ordered.

An ARPEFS experiment involves detecting the angle-resolved photoelectron intensity of a certain atomic core level (potassium 1s level in this study) as a function of electron kinetic energy in one or more directions. Therefore a variable-energy vacuum ultraviolet or X-ray source is required. These experiments were conducted on beamline X24A at the National Synchrotron Light Source at Brookhaven National Laboratory. X-ray photons from the storage ring were monochromatized using a Si(111) double-crystal assembly and focused onto the sample by a toroidal nickel-coated quartz mirror. ARPEFS curves were measured at 130K along two emission directions, the surface normal [111] and 30° from [111] towards [11$\bar{2}$]. The off-normal direction is very close to [771] (29.5° from [111] towards [11$\bar{2}$]), and will for simplicity be denoted as such

hereafter. The photon polarization directions were along [771] for both the [111] and [771] curves. These two experimental geometries, along with a model of the p(2×2)K/Ni(111) structure, are illustrated in Figure 3.1.

For each of the two geometries described above, the potassium 1s photoemission spectra were measured in increments of 0.08 $Å^{-1}$ (corresponding to 3-6eV depending on the kinetic energy) over the kinetic energy range of approximately 70-370eV (photon energy in the range of 3070-3370eV). Each photoemission spectrum had an energy window of 25-30eV, with the photopeak appearing approximately at the center. Data were collected using an angle-resolved and rotatable electrostatic hemispherical analyzer operating at 160eV pass energy. The angular resolution ( half solid-angle) of the input lens is 3°. The combined resolution of the photon source and the electron energy analyzer was around 2.0eV throughout the energy range of this experiment. Each ARPEFS curve consisted of approximately 100 photoelectron spectra and entailed about three hours of measurement. The major contaminants were carbon and oxygen, whose concentrations were estimated with AES to be around 0.15 monolayer 12 hours after the potassium overlayers were prepared. Assuming the adsorption of these contaminants was of constant rate, their coverages would have been less than 0.04 monolayer at the end of the measurement of each truncated ARPEFS curve. As the energy was scanned across the carbon KLL Auger lines near 275eV, about three-quarters into the measurement of an ARPEFS curve, no detectable carbon Auger peaks were observed. This provided additional evidence that the level of impurities on the surface was quite low during the experiment.

## 3.3 DATA REDUCTION

To generate photoemission partial cross sections as a function of photoelectron kinetic energy it is necessary to extract the photopeak areas of all spectra for a given geometry and normalize these areas to one another in order to compensate for the variations in the energy-dependent photon flux and the transmission function of the electron analyzer. Details of this procedure have been described elsewhere.[18] In brief, each photoelectron spectrum was least-squares fitted using a Gaussian-convoluted Doniach-Šunjić function,[20] a Gaussian-convoluted step function, and an experimentally determined background template. These functions modeled the photoemission peak, the energy loss function, and the inelastic background, respectively. The background template also served as an excellent normalization scheme and was also used to subtract the potassium LMM Auger peaks from those photoelectron spectra in which these Auger features appeared.

Once the photoelectron spectra were fitted with the above-mentioned functions, the energy-dependent photoemission intensity I(E) was generated by plotting the Doniach-Šunjić peak area, divided by the coefficient of the background template, as a function of the mean energy of the peak. I(E) can be described by

$$I(E) = I_0(E)[1 + \chi(E)], \tag{1}$$

where $I_0(E)$ is a slowly varying atomic-like partial photoemission cross section for potassium 1s and $\chi(E)$ is the rapid oscillation of this cross section due to the

scattering of electrons by nearby atoms. $\chi(E)$ is the ARPEFS and can be obtained from I(E) by the removal of $I_0(E)$,

$$\chi(E) = [I(E) / I_0(E)] - 1. \quad (2)$$

$I_0(E)$ is the potassium 1s atomic cross section modified by the change of chemical environment upon adsorption to the Ni surface. In principle it can be obtained from theoretical calculations. In practice it could also include other low-frequency variations resulting from our data collection and reduction procedures. Therefore a low-order polynomial was used to least-squares fit I(E) and then used as an approximation to $I_0(E)$. This procedure was shown[18] to reproduce $\chi(E)$ curves very well except for the ARPEFS oscillations that come from those scattering events with path-length differences of less than around 2Å, which could be distorted or eliminated depending on the choice of the particular polynomial. Since the path length differences were much larger than 2Å for all the structural models that we considered in this study, this method of $I_0(E)$ extraction did not cause any significant errors in the derived $\chi(E)$ curves.

Having extracted the ARPEFS $\chi(E)$ curves, it is necessary to convert $\chi(E)$ into $\chi(k)$ for Fourier analysis, where k is the magnitude of the photoelectron wavevector inside the Ni crystal and can be calculated using the de Broglie relation:

$$k(\text{Å}^{-1}) = 0.5123[E + V_0(\text{eV})]^{1/2}, \quad (3)$$

where $V_0$ is the inner potential of the solid. The exact value of $V_0$ is not known, but is around 10eV for nickel and possibly a few eV less after the adsorption of potassium due to the lower work function. $V_0$ is treated as an adjustable parameter in our R-factor analysis; for the purpose of qualitative Fourier analysis we simply used 8eV to do the conversion. The ARPEFS $\chi(k)$ curves obtained in this manner are illustrated in Figure 3.2. The [111] $\chi(k)$ curve represents the average of two separate runs on separately prepared potassium overlayers. The [771] $\chi(k)$ curve was also measured on newly prepared overlayer.

## 3.4 RESULTS AND ANALYSIS

This section is divided into two parts. Section 3.4.1 presents procedures and results of detailed structural analysis using the [111] data. The [771] curve has very small oscillations and was not used to search for the structure. It will be presented in Section 3.4.2 as supporting evidence for the top-site adsorption geometry that was favored from the analysis of Section 3.4.1. In Section 3.4.3 we discuss the results of structural refinements for the atop site with consideration to the possibility of surface reconstructions, and present estimates of uncertainties associated with the optimized structural parameters.

### 3.4.1 The [111] Data

Recent ARPEFS studies[15-18] have employed a two-step approach to the surface structural determination using the measured $\chi(k)$ curves. Adsorption sites and approximate interatomic distances could in many cases be determined from

simple Fourier analysis, while quantitative surface geometries require theoretical simulations. To understand how structural information can be extracted from the ARPEFS $\chi(k)$ curves it is useful to examine the ARPEFS equation, which in the limit of single-scattering follows the expression,

$$\chi(k) = 2\sum_j \frac{\cos\beta_j}{\cos\gamma}\frac{|f(\theta_j)|}{r_j}\cos[kr_j(1-\cos\theta_j)+\phi_j]e^{-\Delta R_j/\lambda}e^{-\sigma_j^2(1-\cos\theta_j)k^2}, \qquad (4)$$

where j indexes all atoms near the potassium atom from which the 1s core-level photoemission is measured. The angle $\beta_j$ is between the photon polarization vector and the vector connecting the photoemitting potassium atom and the jth scattering atom; $\gamma$ is the angle between the polarization and the electron emission directions; and $r_j$ is the interatomic distance between the photoemitter and the jth surrounding atom. The emission-angle dependent path-length difference is given by $\Delta R_j = r_j(1-\cos\theta_j)$, where $\theta_j$ is the scattering angle. The k-dependent complex scattering factor $f(\theta_j)$ represents the jth atom in the scattering problem, and can be decomposed into the amplitude $|f(\theta_j)|$ and the phase $\phi_j$. It is well known that the scattering amplitude $|f(\theta_j)|$ is strongly peaked in the forward scattering ($\theta_j = 0°$) and backscattering ($\theta_j = 180°$) directions, with backscattering followed by forward scattering (double scattering) having the largest combined amplitude. Surface thermal vibrations are described using a correlated Debye-Waller model[21] and represented in Eq. 4 by $e^{-\sigma_j^2(1-\cos\theta_j)k^2}$, where $\sigma_j^2$ is the mean-square relative displacement (MSRD) between the photoemitter and the jth scattering atom, projected on the photoelectron momentum change direction. The inelastic losses due to the excitation of plasmons and electron-hole pairs by the energetic

photoelectrons are described empirically the exponential decay factor $e^{-\Delta R_j/\lambda}$, where $\lambda$ stands for the electron mean free path.

### 3.4.1.1 Fourier analysis

The sinusoidal form of $\chi(k)$ in Eq.(4) suggests that if a Fourier transformation is made of the data, the positions of the peaks in the Fourier transform should appear near the path-length differences $\Delta R_j = r_j(1-\cos\theta_j)$, shifted by some small amount due to the scattering phase function $\phi_j$. The shift caused by $\phi_j$ is usually less than 0.2 Å and can be ignored for qualitative analysis. In systems where different adsorption sites yield significantly different path-length differences, usually only one of the possible sites considered would have path-length differences that match the Fourier peak positions within physically reasonable range for the adsorbate-substrate bond length. In addition, the intensities of the Fourier peaks should also reflect the influence of the various terms in Eq. (4), especially the strong dependence of the scattering amplitude on the scattering angle. A good match of peak positions and relative intensities provides the basis for the selection of a favored site.

The Fourier transform spectrum for the [111] $\chi(k)$ curve (Figure 3.2) is shown in Figure 3.3. The dominant feature around 6Å in comparison with other peaks indicates that, under our experimental condition where potassium 1s electrons are detected along the [111] direction, this feature is mainly associated with electrons being scattered from first-layer nearest-neighbor nickel atoms directly (or nearly directly) under the potassium atoms along [111]. Since the resolution of the Fourier spectrum is estimated to be ~2Å, and the 6Å peak is

broad and asymmetric, it could actually be the overlap of two or more closely spaced peaks. It can be shown that, for the various potassium adsorption sites that we shall consider, namely atop site, hcp and fcc hollow sites, and bridge site, scattering of photoelectrons by the next nearest-neighbor first-layer nickel atoms could make a small contribution to the broad 6Å, with path-length difference of ~7Å. However, the major contribution is from the strong scattering at ~6Å, and the following discussion should not be affected by the smaller contribution at 7Å. The much weaker second peak at ~9.3Å is at least partly due to backscattering (or near backscattering) from nearest second-layer nickel atoms. Using 6Å as the path-length difference associated with scattering from the nearest-neighbor nickel atoms and 2.0Å as the first-to-second layer spacing of nickel, we could estimate the scattering path-length differences and scattering angles associated with these two features for the four possible potassium adsorption sites mentioned above. The results are listed in Table 3.1.

From Table 3.1 we can see that, due to the close-packing of the Ni(111) surface and the large size of the potassium atoms, it is possible for all the adsorption sites considered to match path length differences determined from the experiment within physically reasonable range of K-Ni bond lengths. However, because in the case of atop adsorption the potassium atom has a first-layer nickel atom directly underneath along the [111] surface normal, and the second-layer nickel atoms lie at angles somewhat removed from the backscattering (followed by forward-scattering) geometry, Fourier transform of the [111] $\chi(k)$ curve should show a large intensity ratio ($I_{6Å}/I_{9.5Å}$) of the resulting two peaks. For the other candidate sites this intensity ratio is expected to be smaller. Therefore, the large intensity ratio of these two peaks in the experiment results alone would seem to

favor the atop site. However, since factors other than the scattering angle, such as the number of scattering atoms, thermal vibrations, and the distances of scattering atoms from emitter (Eq. 4) can also affect the overall intensity of a peak, the above analysis alone does not exclude the other sites, especially considering that the scattering angles for the other sites are not too far away from the backscattering or forward scattering conditions. To distinguish among the various sites a more quantitative knowledge of how these various factors affect the scattering process is required. For this we will use a R-factor minimization procedure based on theoretical multiple-scattering spherical-wave (MSSW) simulations.

### 3.4.1.2 MSSW analysis

The theoretical background of MSSW has been described in great detail elsewhere.[21] It can be simplified as Eq. (4), but MSSW is a much more complete and complicated theory that correctly takes into account, among other things, multiple-scattering and spherical-wave effects to numerically calculate $\chi(k)$. A MSSW calculation requires a set of trial structural parameters, like adsorption site(s), atomic interlayer spacings, surface reconstruction and corrugation, as well as nonstructural parameters that include atomic partial-wave phase shifts (PWPS), isotropic Debye temperatures of surface atomic layers, photon polarization and electron detection directions, analyzer aperture, mean-free path parameters, and experimental temperature. Values of the some of the parameters are varied to calculate a series of $\chi(k)$ curves, which are then compared with the experimentally determined $\chi(k)$ curves. Typically one structure gives the best agreement

between the theory and the experiment, and can be taken as the most likely structure.

In the present study five different adsorption sites were evaluated for the geometric structures of the potassium overlayer. In addition to the above-mentioned atop site, fcc hollow site, hcp hollow site, and bridge site, we also included the substitutional site, in which one out of every four first-layer nickel atoms is replaced by a potassium atom while still preserving the p(2×2) superlattice symmetry. Only two structural parameters, namely the potassium-nickel interatomic distance and the first- to second-nickel interlayer spacing, were varied in the initial search. Their ranges are 2.5 - 3.7Å and 1.75 - 2.3Å, respectively. For the bridge-site adsorption the $\chi(k)$ curves for three domains were calculated and averaged.

Amongst the nonstructural parameters, only the potassium surface Debye temperatures and the inner potential were varied. The nickel bulk Debye temperature was fixed at 375K, while the surface Debye temperature was fixed at 265K, which assumes that the mean-square relateive displacement of the surface nickel atoms is twice that of the bulk. The horizontal and vertical Debye temperatures for the potassium layer were varied independently between 50-300K. The inner potential $V_0$ in Eq. (3), used to convert experimental data from energy space into k-space for comparison with theory, was treated as an adjustable parameter and allowed to vary between 4 and 12eV.

The nickel and potassium partial-wave phase shifts used in the present study were calculated using a modified program by Pendry,[22] with the atomic scattering potentials taken from the calculations of Moruzzi, Janak, and Williams.[23] A total of twenty partial-wave phase shifts were calculated. The nickel

phase shifts derived in this manner were the same as those used in previous studies.[24,18] The inelastic scattering was accounted for by including an exponential factor $e^{-r/\lambda}$ in the scattering amplitude, where $\lambda = ck$, and $c = 0.753$. The aperture size of the hemispherical electron analyzer was fixed at 3° half angle. The photon polarization and electron detection directions, and the crystal temperature (130K) were experimentally determined quantities. Although they could also be varied in the calculations, they were set at their experimental values to avoid a cumbersomely large parameter set.

To determine the geometric structure from the ARPEFS data the experimental $\chi(k)$ curve was compared with MSSW calculations by varying the values of the above-mentioned five structural and non-structural parameters until the best agreement was reached. This optimization was implemented by minimizing the R-factor, defined as

$$R = \frac{\sum_i [\chi_E(k_i) - \chi_T(k_i, \{P_j\})]^2}{\sum_i \chi_E^2(k_i)} , \qquad (5)$$

where $\chi_E(k)$ is the experimentally determined ARPEFS curve, $\chi_T(k)$ is the MSSW calculation, subscript i indicates the ith data point, and $\{P_j\}$ is the set of parameters to be optimized. The k range was 4.8-9.7Å$^{-1}$. To minimize the R-factors for each of the five test structures, a simplex routine was used to automatically search both the structural and nonstructural parameters simultaneously until a minimum R factor was reached. Different initial guesses were tried to make sure that results from the fits were reproducible.

The experimental $\chi_E(k)$ curve used in the R factor minimization was smoothed by Fourier-filtering out high-frequency noise. Residual low-frequency contributions not removed by the $I_0(E)$ extraction procedure described in Section 3.3 were also filtered out. The cutoff range was 2-15Å. The theoretical $\chi(k)$ curves were calculated for path-length differences between zero and 15.5 Å, then filtered at 2 - 15Å, as was the experimental curve.

The structural and non-structural parameters determined from the best fits for the five test sites are summarized in Table 3.2. Comparison between the experimental and theoretical $\chi(k)$ curves is presented in Figure 3.4. Table 3.2 shows that the agreement between experiment and theory is best for the atop site, with the lowest R-factor, though the R-factors for the fcc and hcp sites are not too bad. This can also be seen in Figure 3.4, where the experimental and the theoretical $\chi(k)$ curves have the best visual match for the atop site, but for the fcc site and the hcp site the match in the gross peak positions (but not in the $\chi(k)$ amplitudes) is also reasonable. However, if we Fourier-transform all the above best-fit theoretical $\chi(k)$ curves and compare them with the experimental curve, as shown in Figure 3.5, it is clear that the atop site stands out as having a much better match between theory and experiment in both the Fourier-peak positions and the relative amplitudes of these peaks. Since the determination of the adsorption site relies in large part on the first and second peaks, the superior agreement for the atop site provides strong evidence that it is the most probable site for potassium.

One might ask why the fits for the other (than atop) sites look better in k space (Figure 3.4) than in r space (Figure 3.5), especially since the k-space data are usually thought to contain more information. A possible explanation is that in

the k space fitting, many scattering events (from first layer, second layer, etc.) combine to make the total set of frequency, phase and amplitude parameters. For the fcc, hcp, bridge, and substitutional sites the relative contribution from the second layer is quite important (as can be seen from the strong Fourier peak near 10Å in the calculated curves). They can combine with the less important (compared with top site) contribution from the first layer to make the overall fit look reasonable. On the other hand, if we were to do the R-factor analysis using the Fourier transform of the experimental and theoretical curves (*i.e.*, in the r space), it is conceivable that the fit for these sites could be improved, but the optimized structural parameters for all but the atop-site would be quite different from those obtained from the k-space fit! Therefore it is very important to Fourier transform the best-fit $\chi(k)$ curves and compare them in the r space, especially when the k-space fit does not strongly favor a site. In summary, while the k-space R-factor minimization tries to fit the overall phase, amplitude and frequency of a calculated $\chi(k)$ curve with those of an experimental $\chi(k)$ curve, the Fourier transform breaks down the $\chi(k)$ curves into individual frequencies corresponding to scattering path-length differences and allows us to examine whether each frequency is well represented in the $\chi(k)$ curves. Good experimental-theoretical agreement in both k space and R space enhances the confidence for selecting a given parameter set (including adsorption site) over the others.

### 3.4.2 The [771] Data

Additional evidence for atop-site adsorption can be obtained from the off-normal [771] $\chi(k)$ curve. Ideally we could have applied the above R-factor

minimization to this $\chi(k)$ curve to obtain another set of optimized structural and nonstructural parameters, which would have allowed us to verify if consistent results were obtained from independent measurements. In cases where only one of the tested sites has consistent results and also has the lowest R-factors, such as in the case of p2mg(2×1)CO/Ni(110) (Ref. 18), one can say with confidence that the preferred site is correct. The independently determined sets of parameters also provide a more meaningful mechanism for the estimation of errors. In the present study, however, the small oscillations and the rather large relative uncertainties (±3.5% maximum oscillations vs. 2% uncertainty) in the experimental [771] $\chi(k)$ curve could either make the R-factor optimization non-convergent, or they could translate into large error bars for the structural parameters. Our approach was instead to calculate theoretical [771] $\chi(k)$ curves using the optimized parameters (Table 3.2) for each of the five trial sites from the [111] data and compare these calculated $\chi(k)$ curves with the experimental curve. Figure 3.6 shows the results. Again, due to the small oscillations and the large error bars, what we will focus on here is not the point-by-point fit of the curves, but the overall agreement in the peak and valley positions and the overall magnitude of the oscillations. From Figure 3.6 we see that the experimental-theoretical agreement is very poor for the substitutional site and the fcc and hcp hollow sites. If the potassium atoms were to occupy one of these sites, the large oscillations in the $\chi(k)$ curves ( 6-10%) as modeled by the MSSW theory should have shown up in the experimental $\chi(k)$ curve as well, even given the large error bars. The match in peak positions for these sites were also quite poor. For the atop and bridge sites the experimental-theoretical fits are about equally good, but for atop-site adsorption the match in

the peak positions is significantly better, wht the largest deviation coming in the low-k range, where the MSSW theory is less accurate.

### 3.4.3 Structural refinement and error analysis

Combining the results of Sections 3.4.1 and 3.4.2 we conclude that the potassium atoms are strongly favored to adsorb on the atop sites in the p(2×2)K/Ni(111) surface layer. We have also determined that the K-Ni bond length is 3.02Å and the first- to second-layer spacing of nickel is 1.90Å, or about 6.5% contraction from the bulk spacing of 2.033Å. In this section we will explore the possibility that the surface layer may arrange itself in more complicated ways. In particular we will consider whether, in the p(2×2) superlattice in which only one out of every four first-layer nickel atoms is directly bonded to a potassium atom and the other three do not have direct bonding with potassium, the first-layer nickel atoms without the potassium bonding may undergo reconstructions both in the vertical and lateral directions, while at the same time preserving the p(2×2) symmetry. These possible reconstructions are illustrated in Figure 3.7.

We searched the optimal values of the lateral and vertical displacements of these nickel atoms using the [111] $\chi(k)$ curve and the above-mentioned R-factor minimization in two ways, by varying these two parameters while fixing the other parameters at their previously optimized values (Table 3.2) and by varying all the parameters at the same time. In both cases we found little reconstruction (<0.01Å) of the first-layer nickel, and the R-factor was not improved, either. In the second method the other parameters were also found to change little (<0.01Å, 5K, and 0.6eV for distances, Debye temperatures and inner potential, respectively) from

those values in Table 3.2. Therefore, we conclude that the surface does not reconstruct upon the adsorption of potassium, except for the downward shift of the first- to second layer nickel spacing from the bulk value.

To estimate the uncertainty associated with each of the structural parameters that were varied (the K-Ni bond length $D_{K\text{-}Ni}$, the vertical distance between the potassium-covered first-layer nickel and the second-layer nickel $Z_{12}$, and the vertical displacement $Z_{11}$ and lateral displacement $X_{11}$ between the occupied and unoccupied nickel atoms in the first layer), we calculated how the R-factor changes when these parameters are varied around their optimal values. Figure 3.8 plots R-factor versus the deviation $(P_j - P_j^{best})$ of parameter j from its optimized value $P_j^{best}$. All parameters except the abscissas were fixed at their optimal values obtained from the above-mentioned "second" method in which all parameters were changed at the same time. What we observe in Figure 3.7 is that the R-factor — hence the $\chi(k)$ curve — is much more sensitive to the change in the K-Ni distance, with a well-defined, steep R-factor minimum, and less sensitive to the other three parameters, particularly the lateral reconstruction $X_{11}$. The statistical error associated with each parameter can be estimated from the curvature of these R-factor plots using a previously described method[18,25]. Table 3.3 lists estimated errors, along with the final optimized values of these parameters. The varying degree of uncertainties for the various parameters is consistent with the observation of the dominant Fourier peak (Figure 3.3) attributable to the backscattering from the occupied nickel atoms. The large uncertainty of the lateral displacement (±0.09Å) as compared to that of the vertical displacement (±0.03Å) is in large part the result of the strong horizontal thermal vibrations (low Debye temperature) of the potassium surface layer. It

underscores the "high" surface mobility (frustrated translations) of adsorbed species on smooth surfaces such as Ni(111), especially for large adsorbates such as alkali metals. In the case of atop adsorption this thermal motion is even more important because the interaction of the adsorbate with the substrate atoms is much smaller in the lateral direction than in the vertical direction where there is a strong direct bonding. The low Debye temperature in the lateral direction also helps to explain why the [771] $\chi(k)$ curve has very small oscillations: In addition to the absence of a backscattering nickel atom directly behind the photoemitting potassium atom in the [771] direction, the large lateral thermal vibrations have a greater projection on the off-normal direction [771] than on the normal direction [111] for scattering angles close to 180°. Accordingly, the [771] $\chi(k)$ curve is attenuated more severely by the thermal vibrations (see Eq. 4).

## 3.5 DISCUSSION AND CONCLUSIONS

Our result that the potassium atoms are favored to adsorb on the atop sites in the p(2×2)K/Ni(111) overlayer agrees with the LEED study of Fisher *et al.*, but there are some discrepancies in the final structural parameters. Table 3.3 compares the optimized structural parameters from the two studies. Both the LEED and the present ARPEFS studies show that the vertical spacing between the potassium-covered first-layer nickel and second-layer nickel $Z_{12}$ is 1.90Å, or about 0.13Å contraction from the bulk value. The agreement in the horizontal displacement $X_{11}$ is also reasonable given the large error bars of both studies. However, the K-Ni bond length of 3.02±0.01Å determined from this study is 0.2Å larger than the 2.82±0.04Å obtained by LEED. Another discrepancy is that the ARPEFS study

finds no corrugation ($Z_{12}$ = 0.00±0.03Å) of the first nickel layer, while from the LEED work the first-layer nickel atoms not occupied by potassium atoms are raised by 0.12±0.02Å outward (toward the vacuum) relative to those that are covered. It should be pointed out that the errors quoted in Table 3.3 for this work only include *statistical* errors from the least-square R-factor minimization. Other possible sources of error, such as the calculated scattering phase shifts used in the MSSW simulation and the alignments of the crystal and electron analyzer, may increase the uncertainty of the measured K-Ni bond length by about 0.03Å, but they still cannot account for the 0.2Å difference. Sizable differences in the structural results obtained from different techniques have also been reported on other surfaces. For example, studies[26-28] of p(2×2)S/Ni(111) using LEED, ARPEFS, and SEXAFS (surface extended X-ray adsorption fine structure) yielded S-Ni bond lengths ranging from 2.10Å to 2.23Å. For some other systems the structural results are quite consistent among the various techniques. In the case of c(2×2)S/Ni(100) the S-Ni bond length varies only by 0.04Å (between 2.19Å and 2.23Å) among LEED, ARPEFS, and SEXAFS studies.[29,14,30] It is not clear what the causes are that the K-Ni bond length differs by 0.2Å between the LEED study of Fisher *et al.* and this work. A SEXAFS experiment on p(2×2)K/Ni(111) may help resolve this difference.[31]

The effective hard-sphere radius of potassium from this work is 1.77Å; in comparison the metallic radius of potassium is 2.38Å. Therefore it appears that the bonding between potassium and nickel is not likely to be purely metallic: we do not expect to see a change of 0.6Å in the sum of their metallic radii if both the initial and final states are metallic. However, a down shift of the interatomic distance is expected if the K-Ni bond is partly ionic or covalent. A simplistic

explanation is that in the case of covalent bonding the two atoms are pulled closer by the overlapping bonding electrons, while in the case of ionic bonding the ionic radius of potassium is much smaller than its metallic radius. For 6-coordinated potassium ions the radius is around 1.33Å; it is 0.83Å for on-top $K^+$ after correcting for coordination numbers.[32] On the other hand, in the case of ionic bonding one might reasonably assume that the charge transfer to the nickel atoms will increase their radii by some amount. It is clear that the distinction between ionic and covalent bonding requires more than knowing the bond length. In their Cs/Ru(0001) paper[11] Over *et al.* suggested that the atop sites are favored in the p(2×2) structure because the substrate atoms between neighboring adatoms in the p(2×2) structure enhance the screening between the Cs-Ru dipoles. Their observation of the buckling of the first Ru layer ($Y_{11}>0$) seems to support this explanation. Since $Y_{11}= 0.00 \pm 0.03$Å from this work, it is possible that the quantitative details of the K-K and K-Ni interactions are somewhat different from the Cs-Cs and Cs-Rh interactions, or it might suggest that the K-Ni bond is somewhat covalent — after all the bonding is quite directional for on-top adsorption. More experimental and theoretical work is needed to achieve a better understanding of the bonding between adsorbed alkali metals and substrate metals. What may be implied from the structural studies done so far on alkali metals adsorbed on metal surfaces is that, regardless of the bond character, the energy difference between the atop site and the hollow sites is so small because of the smoothness of the close-packed (111) surfaces and the large size of the alkali metals that other factors, such as the specific alkali metal and substrate metal involved and their relative electronegativity, may tip the balance in favor of one of the possible sites.

# REFERENCES


1. *Physics and Chemistry of Alkali Metal Adsorption*, edited by H.P. Bonzel, A.M. Bradshaw, and G. Ertl (Elsevier, Amsterdam, 1989).
2. H. Ishida and K. Terakura, Phys. Rev. B **38**, 5752 (1988); H. Ishida, Phys. Rev. B **39**, 5492 (1989); H. Ishida, Surf. Sci. **242**, 341 (1991).
3. D.M. Riffe, G.K. Wertheim, and P.H. Citrin, Phys. Rev. Lett. **64**, 571 (1990).
4. G.M. Lamble, R.S. Brooks, D.A. King, and D. Norman, Phys. Rev. Lett. **61**, 1112 (1988).
5. I. Langmuir, J. Amer. Chem. Soc. **54**, 2798 (1932); I. Langmuir and J.B. Taylor, Phys. Rev. **40**, 464 (1932); I. Langmuir and J.B. Taylor, Phys. Rev. **44**, 423 (1933).
6. R. Schlögl, in Ref. 1.
7. G.N. Hatsopoulos and E.P. Gyftopoulos, Thermionic Energy Conversion (MIT Press, Cambridge, Massachusetts, 1977).
8. N.D. Lang, in Ref. 1.
9. E. Wimmer, A.J. Freeman, J.R. Hiskes, and A.M. Karo, Phys. Rev. B **28**, 3074 (1983).
10. S.Å. Lindgren, L. Walldén, J. Rundgren, P. Westrin, and J. Neve, Phys. Rev. B **28**, 6707 (1983).
11. H. Over, H. Bludau, M. Skottke-Klein, G. Ertl, W. Moritz, and C.T. Campbell, Phys. Rev. B **45**, 8638 (1992).
12. D. Fisher, S. Chandavarkar, I.R. Collins, R.D. Diehl, P. Kaukasoina, and M. Lindroos, Phys. Rev. Lett. **68**, 2786 (1992).

13. M. Kerkar, D. Fisher, D.P. Woodruff, R.G. Jones, R.D. Diehl, and B. Cowie, Phys. Rev. Lett. **68**, 3204 (1992).

14. J.J. Barton, C.C. Bahr, S.W. Robey, Z. Hussain, E. Umbach, and D.A. Shirley, Phys. Rev. B **34**, 3807 (1986).

15. L.J. Terminello, X.S. Zhang, Z.Q. Huang, S.Kim, A.E. Schach von Wittenau, K.T. Leung, and D.A. Shirley, Phys. Rev. B **38**, 3879 (1988).

16. L.J. Terminello, K.T. Leung, Z.Hussain, T. Hayashi, X.S. Zhang, and D.A. Shirley, Phys. Rev. B **41**, 12787 (1990).

17. L.Q. Wang, Z. Hussain, Z.Q. Huang, A.E. Schach von Wittenau, D.W. Lindle, and D.A. Shirley, Phys. Rev. B **44**, 13711 (1991).

18. Z.Q. Huang, Z. Hussain, W.T. Huff, E.J. Moler, and D.A. Shirley, Phys. Rev. B, submitted.

19. J.J. Barton, Ph.D. thesis, University of California, Berkeley, 1985.

20. S. Doniach and M. Šunjić, J. Phys. C **3**, 285 (1970).

21. J.J. Barton, S.W. Robey, and D.A. Shirley, Phys. Rev. B **34**, 778 (1986).

22. J.B. Pendry, *Low Energy Electron Diffraction* (Academic, London, 1974).

23. V. Moruzzi, J. Janak, and A. Williams, *Calculated Electronic Properties of Metals* (Pergamon, New York, 1978).

24. S.W. Robey, J.J. Barton, C.C. Bahr, G. Liu, and D.A. Shirley, Phys. Rev. B **35**, 1108 (1987).

25. P.R. Bevington, *Data Reduction and Error Analysis for the Physical Sciences* (Mcgraw-Hill, New York, 1969).

26. Y.K. Wu and K.A.R. Mitchell, Can. J. Chem. **67**, 1975 (1989).

27. A.E. Schach von Wittenau, L.Q. Wang, Z. Hussain, Z.Q. Huang, and D.A. Shirley, (unpublished).

28. T. Yokoyama, M. Funabashi, Y. Kitajima, T. Ohta, and H. Kuroda, Physica B, **158**, 643 (1989).

29. U. Starke, F. Bothe, W. Oed, and K. Heinz, Surf. Sci. **232**, 56 (1990).

30. J. Stohr, R. Jaeger, and S. Brennan, Surf. Sci. **117**, 503 (1982).

31. R.D. Diehl, private communication.

32. C. Kittel, *Introduction to Solid State Physics*, 6th ed. (Wiley, New York, 1986), p.77.

Table 3.1. Estimated scattering angles of major scattering events contributing to the 6Å and 9.3Å Fourier peaks (Fig.3) for the various test adsorption sites.

| Adsorption site | 6Å peak | | | 9.3Å peak |
|---|---|---|---|---|
| | path length difference (Å) | bond length(Å) | scattering angle (degrees) | scattering angle (degrees) |
| top | 6.0 | 3.0 | 180 | 165 |
| | 6.0 | | 180 followed by 0 | |
| fcc hollow | 6.0 | 3.2 | 155 | 165 |
| | 6.3 | | 180 followed by 25 | |
| hcp hollow | 6.0 | 3.2 | 155 | 180 |
| | 6.3 | | 180 followed by 25 | |
| bridge | 6.0 | 3.1 | 155 | 170 |
| | 6.2 | | 180 followed by 25 | |

Table 3.2: Optimized parameters obtained from the R-factor minimization for the various tested adsorption sites.

| Adsorption site | K-Ni bond length (Å) | Ni(1)-Ni(2) distance (Å) | Debye temperature of potassium (K) | | Inner potential (eV) | R-factor |
|---|---|---|---|---|---|---|
| | | | horizontal | vertical | | |
| substituted | 3.60 | 1.99 | 105 | 265 | 4.0 | 0.62 |
| bridge | 3.20 | 1.96 | 60 | 275 | 7.9 | 0.36 |
| hcp hollow | 3.27 | 2.01 | 60 | 200 | 4.0 | 0.32 |
| fcc hollow | 3.26 | 1.94 | 85 | 175 | 7.7 | 0.31 |
| top | 3.02 | 1.90 | 75 | 175 | 6.6 | 0.21 |

Table 3.3: Best-fit structural parameters and statistical errors (in parentheses) from this work and the LEED study, Ref. 12.

| Source | $D_{K\text{-}Ni}$ (Å) | $Y_{12}$ (Å) | $Y_{11}$ (Å) | $X_{11}$ (Å) |
|---|---|---|---|---|
| ARPEFS | 3.02 (.01) | 1.90 (.04) | 0.00 (.03) | 0.00 (.09) |
| LEED | 2.82 (.04) | 1.90 (.03) | 0.12 (.02) | 0.06 (.06) |

# FIGURE CAPTIONS

Figure 3.1. The p(2×2)K/Ni(111) surface is shown with the potassium atoms occupying the atop sites. The emission directions in which the electrons are detected are labeled [111] and [771]. The photon polarization directions are along [771] for both experimental geometries. For ease of viewing the potassium atoms (shaded) are reduced.

Figure 3.2. Experimental $\chi(k)$ curves. The path-length-difference cutoffs for the filtered data are 2 - 15Å for both [111] and [771] curves. The [111] curve is the average of two curves, each measured on a newly prepared potassium overlayer.

Figure 3.3. Fourier transformation of the [111] $\chi(k)$ curve pictured in Figure 3.2.

Figure 3.4. Comparison between the [111] experimental $\chi(k)$ curve and best-fit MSSW calculations for the various trial adsorption sites. The solid lines are experimental curves and the dashed lines are MSSW calculations. The structural and nonstructural parameters used to generate the theoretical curves are listed in Table 3.2. Experimental curves do not line up exactly for the different sites because the optimized inner potentials are different (Eq. 3).

Figure 3.5. Fourier transformation of the $\chi(k)$ curves in Figure 3.4. The solid lines are experimental data and the dashed lines are MSSW calculations.

Figure 3.6. Comparison between the [771] experimental $\chi(k)$ curve and the MSSW calculations for the various trial adsorption sites. The solid lines are experimental curves and the dashed lines are MSSW calculations. The structural and nonstructural parameters used to generate the theoretical curves are those of the best-fit results using the [111] curve (Table 3.2).

Figure 3.7. (a) Top view and (b) side view of p(2×2)K/Ni(111) showing the vertical and lateral reconstruction of the first-layer nickel atoms. The larger open circles represent potassium atoms, the smaller open circles the first-layer nickel atoms and the shaded smaller circles the second-layer nickel atoms. The structural parameters used in the final R-factor minimization are defined in the side view. The light circles seen in the side view denote first-layer nickel atoms in the unreconstructed geometry.

Figure 3.8 Plots of R-factor versus the deviation $(P_j - P_j^{best})$ of parameter j from its optimized value $P_j^{best}$ for the four structural parameters defined in Figure 3.7. Note the large R-factor range of the ordinate.

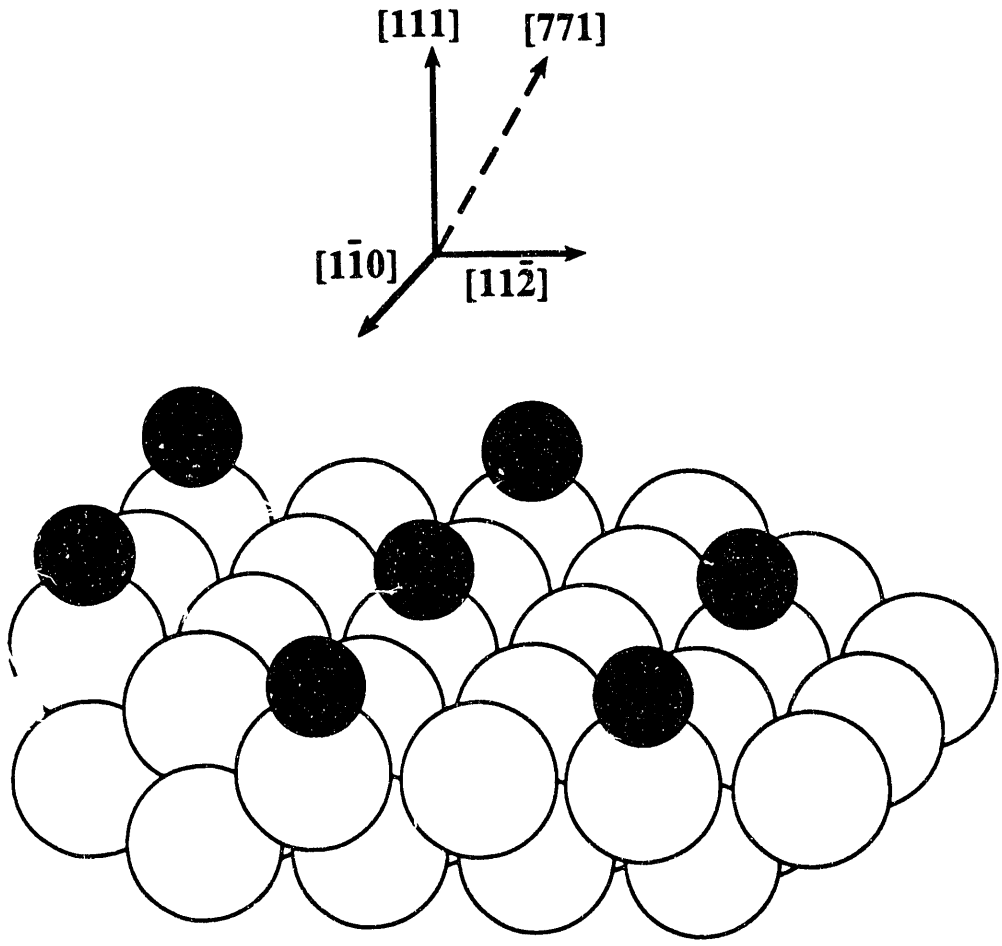


Figure 3.1

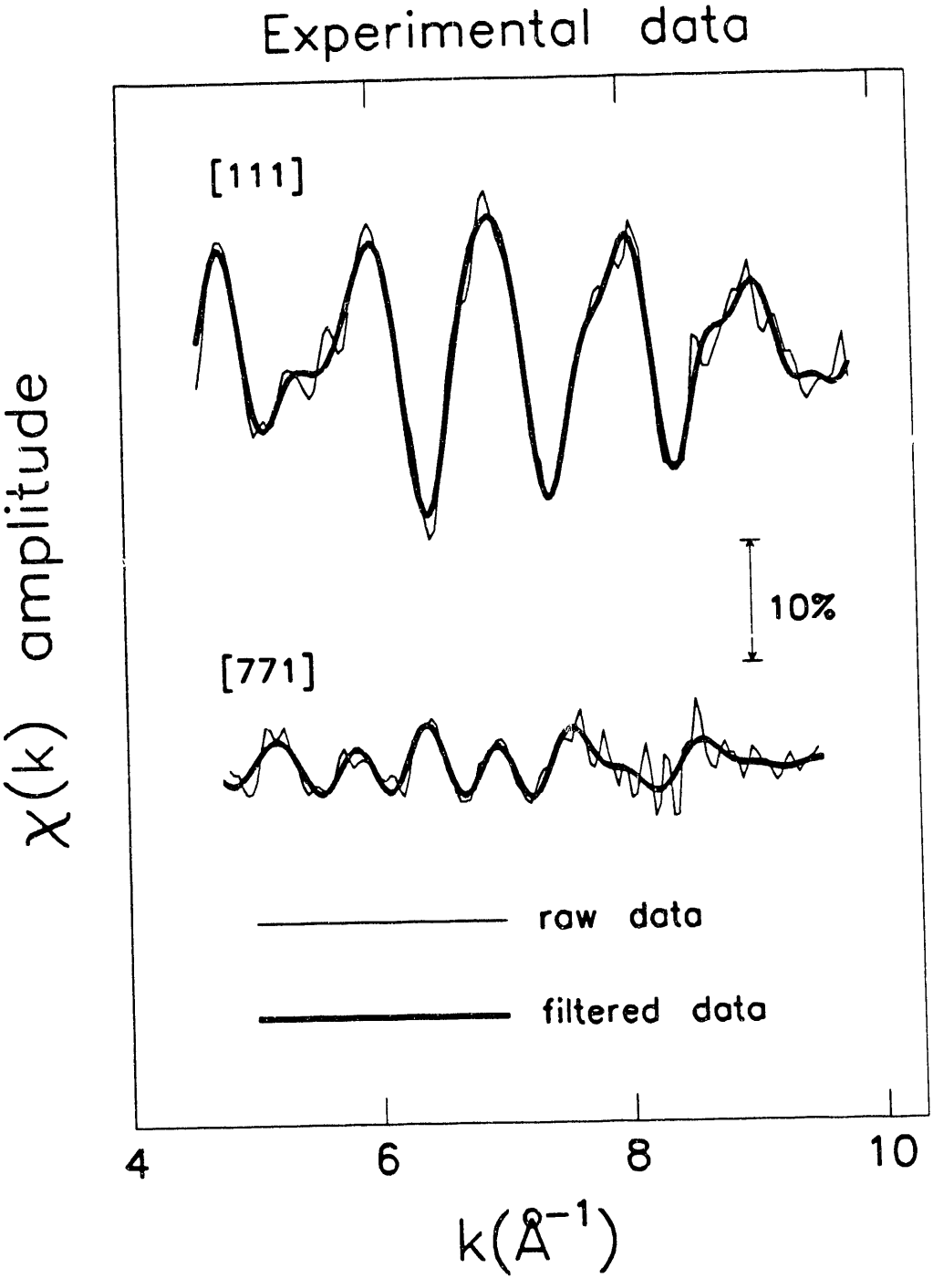
Experimental data
[111]
[771]
10%
raw data
filtered data
χ(k) amplitude
4
6
8
10
k(Å⁻¹)

Figure 3.2

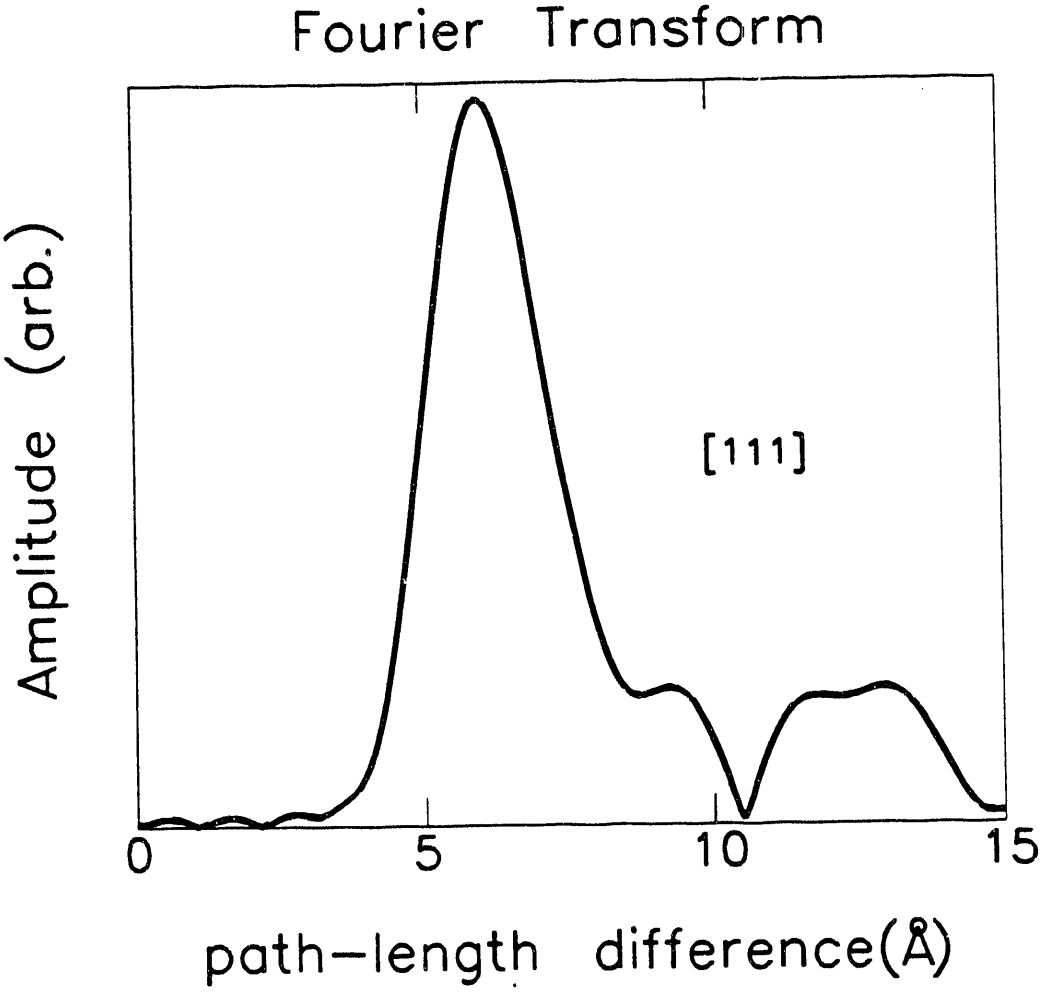
Fourier Transform
Amplitude (arb.)
[111]
0
5
10
15
path-length difference(Å)

Figure 3.3

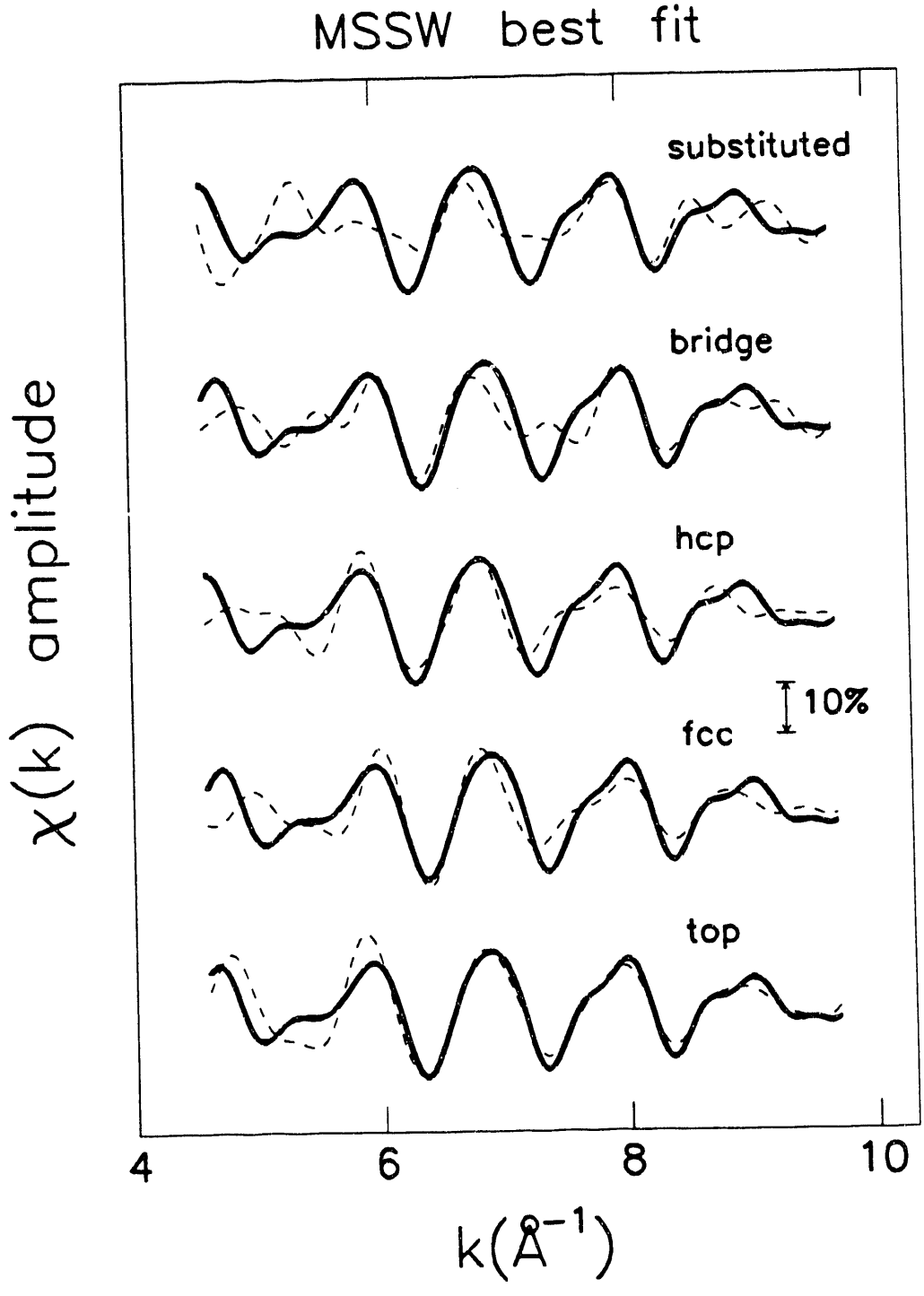
MSSW best fit
substituted
bridge
hcp
10%
fcc
top
χ(k) amplitude
4
6
8
10
k(Å⁻¹)

Figure 3.4

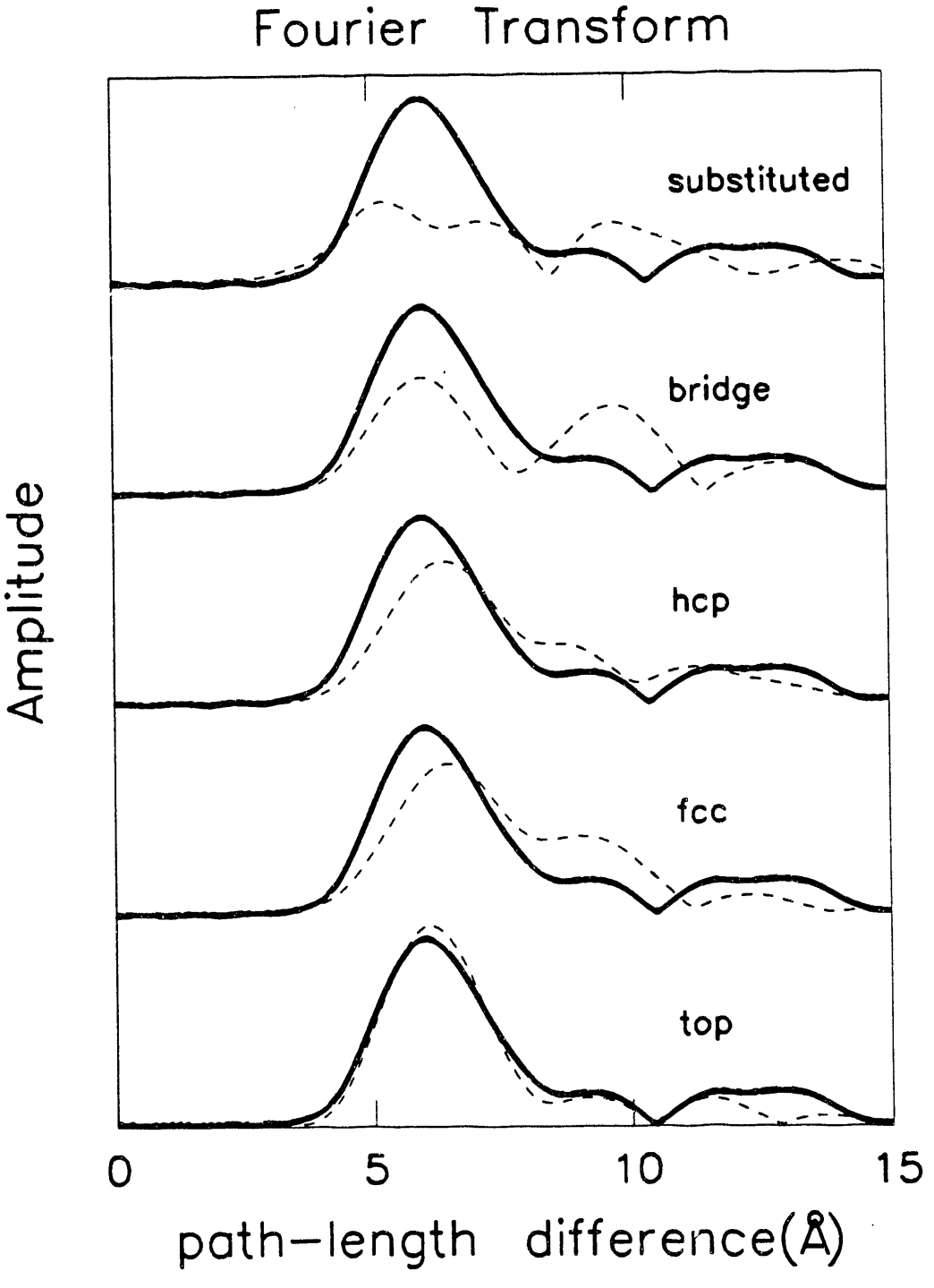
Fourier Transform
substituted
bridge
hcp
fcc
top
Amplitude
0
5
10
15
path-length difference(Å)

Figure 3.5

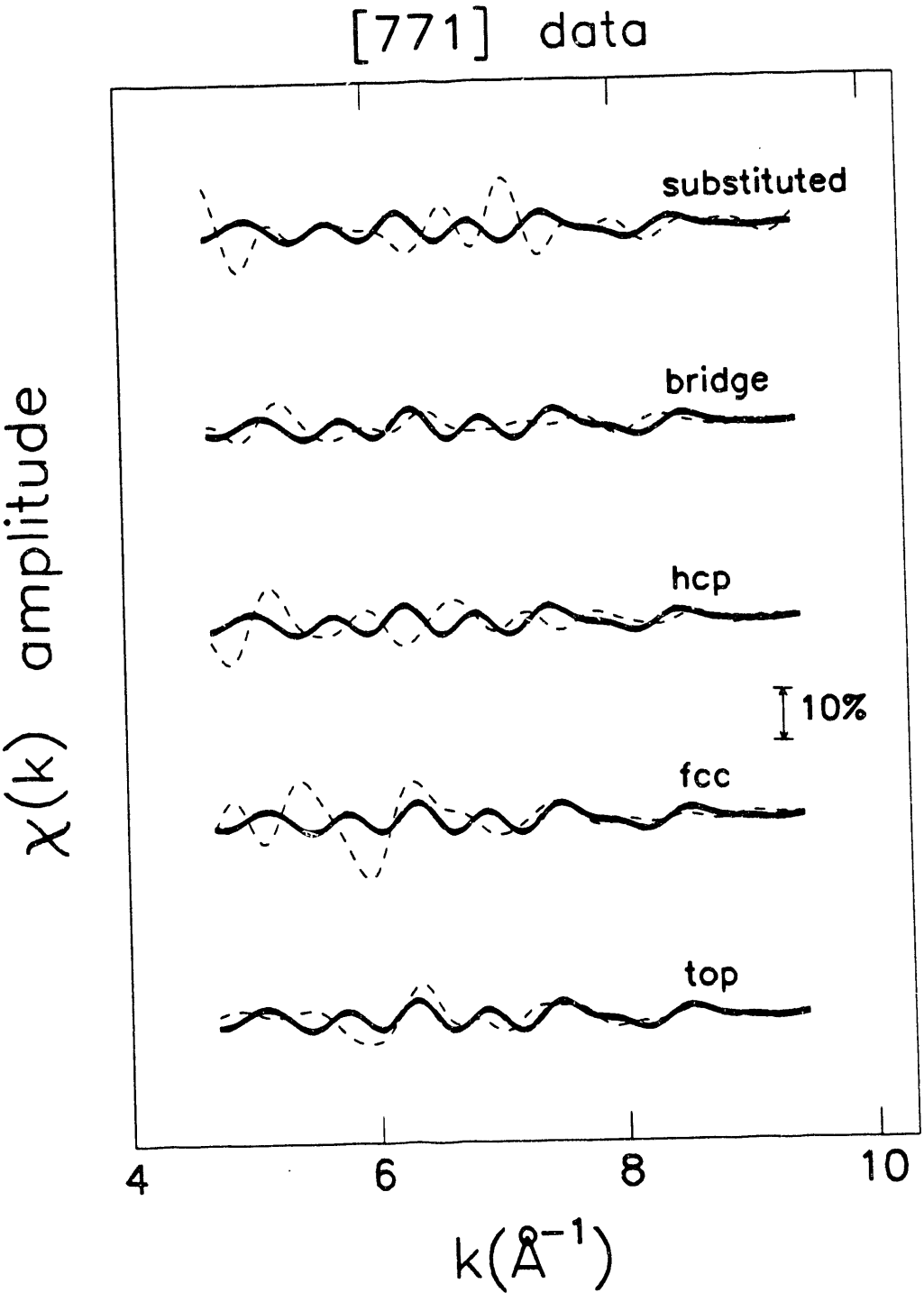
[771] data
substituted
bridge
hcp
10%
fcc
top
χ(k) amplitude
4
6
8
10
k(Å⁻¹)

Figure 3.6

# p(2x2)K/Ni(111)

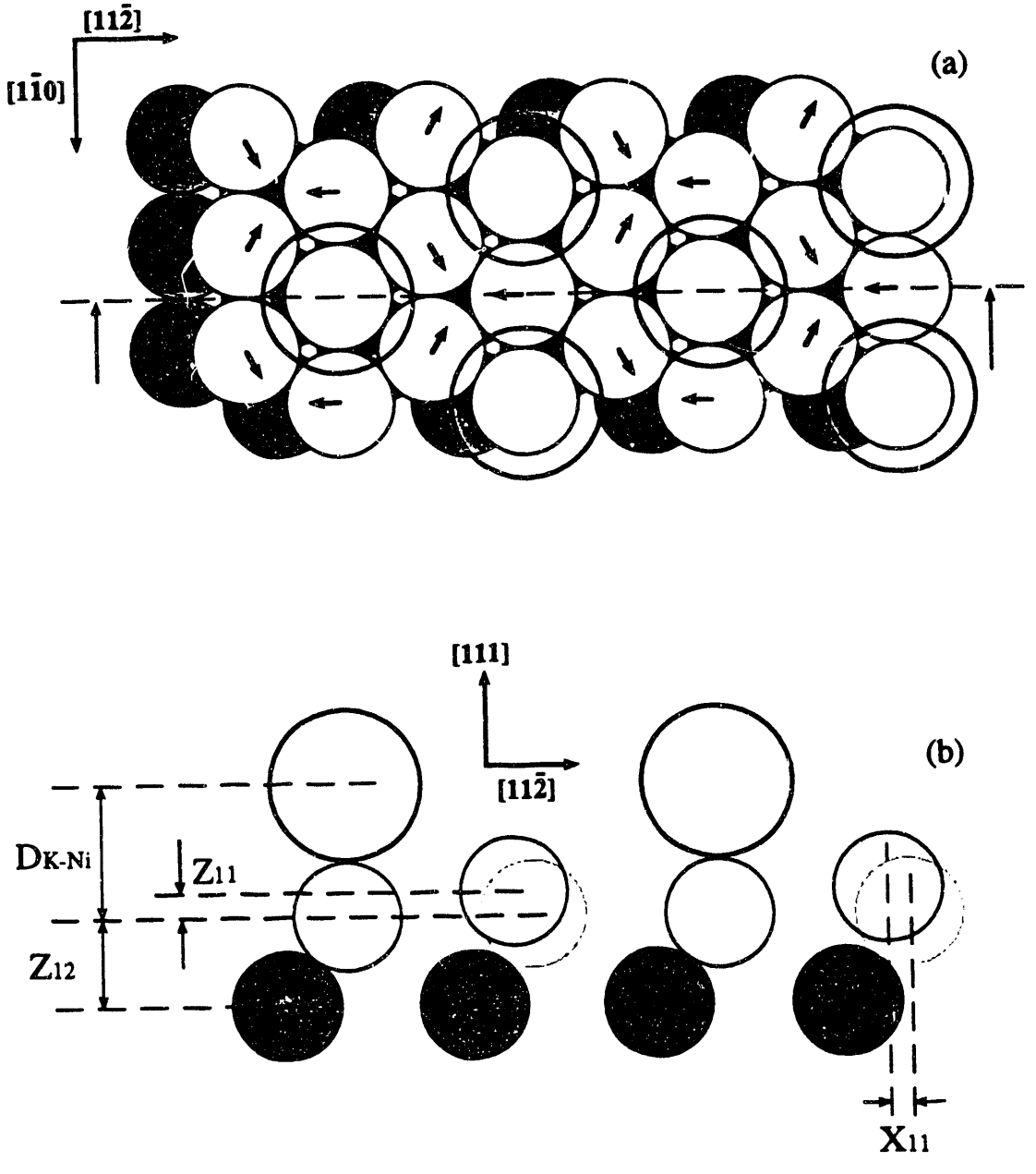


Figure 3.7

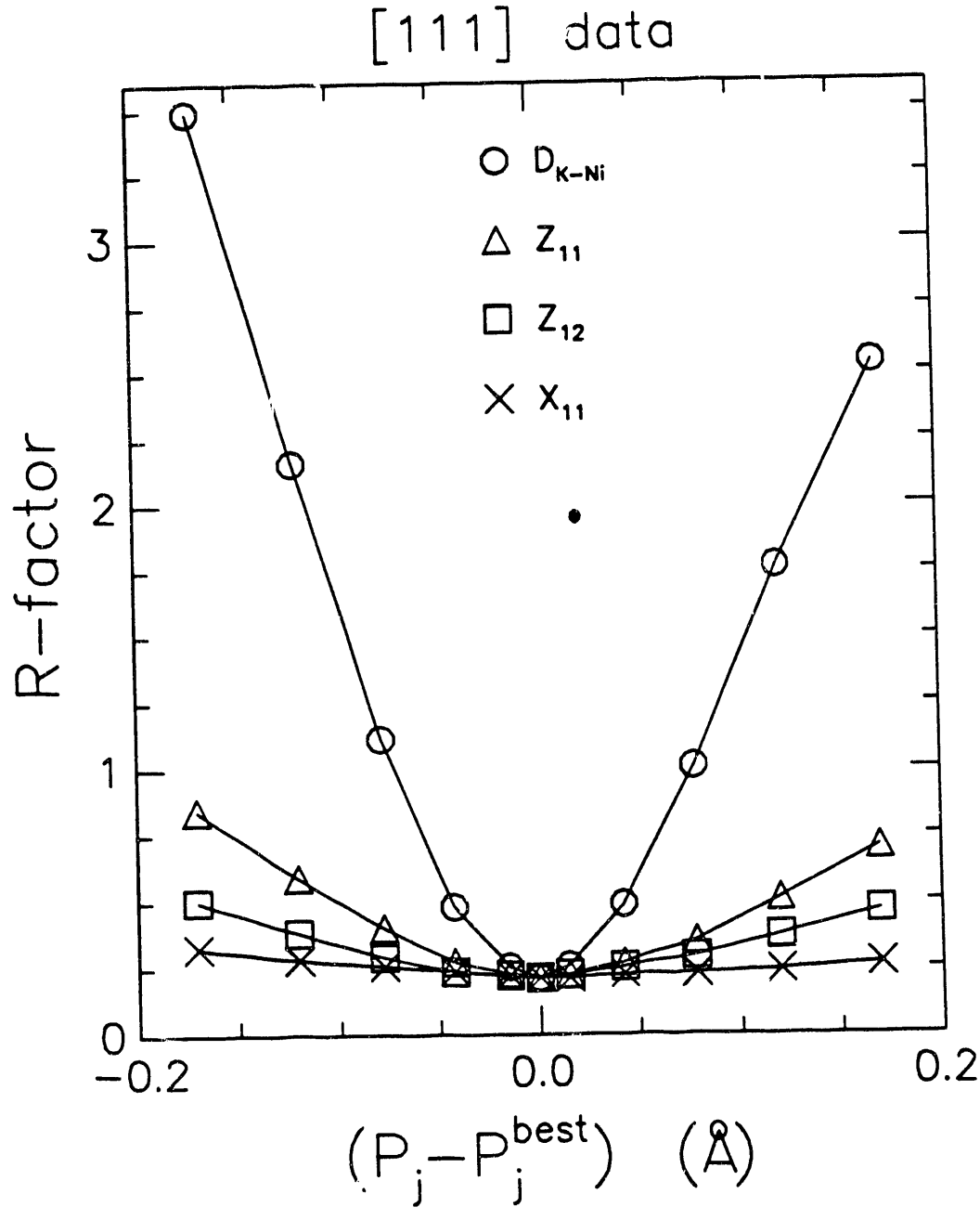


Figure 3.8

DATE
FILMED
2/25/93